



HAL
open science

Medical Bubbles

Michiel Postema

► **To cite this version:**

Michiel Postema. Medical Bubbles. Fluid Dynamics [physics.flu-dyn]. University of Twente, 2004. English. NNT: . tel-03195194

HAL Id: tel-03195194

<https://hal.science/tel-03195194>

Submitted on 10 Apr 2021

HAL is a multi-disciplinary open access archive for the deposit and dissemination of scientific research documents, whether they are published or not. The documents may come from teaching and research institutions in France or abroad, or from public or private research centers.

L'archive ouverte pluridisciplinaire **HAL**, est destinée au dépôt et à la diffusion de documents scientifiques de niveau recherche, publiés ou non, émanant des établissements d'enseignement et de recherche français ou étrangers, des laboratoires publics ou privés.

MEDICAL BUBBLES

MEDISCHE BELLEN

PROEFSCHRIFT

ter verkrijging van
de graad van doctor aan de Universiteit Twente,
op gezag van de rector magnificus
prof. dr. F.A. van Vught,
volgens besluit van het College voor Promoties
in het openbaar te verdedigen
op vrijdag 17 september 2004 om 13.15 uur

door

Michiel Arjen Benjamin POSTEMA

geboren op 19 augustus 1973
te Brederwiede

Dit proefschrift is goedgekeurd door de promotores:
Prof. dr. ir. N. de Jong
Prof. dr. ir. A.F.W. van der Steen

Samenstelling Promotiecommissie

Voorzitter

Prof. dr. ir. L. van Wijngaarden Universiteit Twente

Secretaris

Prof. dr. ir. A. Bliet Universiteit Twente

Promotores

Prof. dr. ir. N. de Jong Universiteit Twente

Prof. dr. ir. A.F.W. van der Steen Erasmus MC

Overige leden

Prof. dr. J. Feijen Universiteit Twente

Prof. dr. W.H. van Gilst Rijksuniversiteit Groningen

Prof. dr. H.H.M. Korsten Technische Universiteit Eindhoven

Prof. dr. A.G.J.M. van Leeuwen Universiteit Twente

Prof. dr. rer. nat. D. Lohse Universiteit Twente

Prof. dr. A. Prosperetti Universiteit Twente, Johns Hopkins University

Dr. F.J. ten Cate Erasmus MC

Support

This work has been supported by the Technology Foundation STW (RKG.5104).

Financial support by the Netherlands Heart Foundation and the Interuniversity Cardiology Institute of the Netherlands for the publication of this thesis is gratefully acknowledged.

Contributions from ALTANA Pharma bv, Oldelft Ultrasonics BV, Philips Nederland B.V. Medical Systems, and Bracco Research SA are kindly acknowledged.

Stellingen

Behorende bij het proefschrift “Medical Bubbles” door Michiel Postema
te verdedigen op 17 september 2004

1. Optisch identieke contrastbellen vertonen onderling verschillend slingergedrag.

Dit proefschrift

2. Behalve voor afbeeldingstechnieken, kunnen contrastbellen ook gebruikt worden om werkzame stof naar een bestemming te vervoeren en ter plaatse te laten ontsnappen door sonisch kraken.

Dit proefschrift

3. Het aantal fragmenten waarin een microbel opbreekt, is een indicatie voor de dominante sferisch harmonische trillingsmode.

Dit proefschrift

4. Jets kunnen benut worden als microinjectienaalden.

Dit proefschrift

5. Het woord *cowboy* heeft meer met paarden dan met koeien te maken.

STELLINGEN

6.

$$F = m a$$

is niet de tweede wet van Newton maar de zestiende stelling van Hermann.

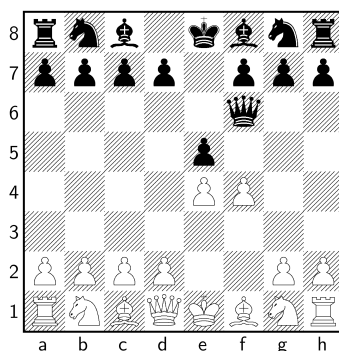
Hermann J. *Phoronomia, sive de Viribus et Motibus Corporum Solidorum et Fluidorum*. Amsterdam: R & G Wetstein 1716.

7. De relatieve hanghoogte van de testikels heeft voorspellende waarde voor links- of rechtshandigheid.

Chang KSF, Hsu FK, Chan ST, Chan YB. Scrotal asymmetry and handedness. *J Anat, Lond* 1960 94:543-548.

McManus IC. Scrotal asymmetry in man and in ancient sculpture. *Nature* 1976 259:426.

8. De Nordwalder variant 1 e4 e5 2 f4 ♖f6 is voordelig voor wit.



9. Het Russische spreekwoord “Een lekkere vent moet vet zijn” duidt op groot potentieel voor superharmonic cardiac imaging.

10. Omsk is een mooie stad maar net iets te ver weg.

Drs. P — Dodenrit

Contents

Woord vooraf	5
Symbols and Abbreviations	11
1 Medical Bubbles and Photography	15
§1 Sound and bubbles, 15 • §2 Historical note, 21 • §3 High-speed photography of medical bubbles, 23 • §4 Outline of this thesis, 26	
2 Images of Microbubbles	27
§1 Introduction, 28 • §2 Imaging theory and simulations, 30 • §3 Experimental setup, 34 • §4 Results, 39 • §5 Discussion and conclusions, 49	
3 Ultrasound-induced Coalescence	53
§1 Introduction, 54 • §2 Theory, 55 • §3 Experimental setup, 61 • §4 Results, 61 • §5 Discussion, 64 • §6 Conclusions, 65	
4 Free Microbubble Coalescence	67
§1 Introduction, 68 • §2 Theory, 69 • §3 Experimental methods, 70 • §4 Results and discussion, 72 • §5 Conclusions, 73	

CONTENTS

5	Pressure Measurements: Simulations	75
	§1 Introduction, 76 • §2 Methods, 77 • §3 Results and discussion, 79 • §4 Conclusions, 80	
6	Ultrasound-induced Gas Release	83
	§1 Introduction, 84 • §2 Experimental setup, 85 • §3 Results, 88 • §4 Discussion and conclusions, 94	
7	Microbubble Phenomena: Overview	97
	§1 Introduction, 98 • §2 Experimental setup, 108 • §3 Results and discussion, 114 • §4 Conclusions, 120	
8	General Considerations	123
	§1 General considerations and summary, 123 • §2 Future prospects, 125	
	Samenvatting	127
	Bibliography	131
	List of Figures	149
	List of Publications	153
	Over de auteur	157

Symbols and Abbreviations

		MLT Θ dimensions
a	acceleration	$L T^{-2}$
α	coefficient defined by $\alpha = \frac{2\pi NA}{\lambda}$	L^{-1}
A	cross-section area	L^2
c	speed of sound	$L T^{-1}$
CCD	charge coupled device	
C_d	drag coefficient	
$\frac{C_i}{C_0}$	saturation ratio	
C_m	added mass coefficient	
d_0	center-to-center bubble distance	L
Δd_m	bubble distance difference, measured	L
Δd_{th}	bubble distance difference, theoretical	L
D	diffusion constant	$L^2 T^{-1}$
\mathcal{D}	bubble diameter	L
E	elastic modulus	$M L^{-1} T^{-2}$
E^*	intrinsic energy ratio	
f	center driving frequency	T^{-1}
f_r	bubble resonant frequency	T^{-1}
F	force	$M L T^{-2}$
F_a	added mass force	$M L T^{-2}$
F_d	drag force	$M L T^{-2}$
F_{rad}	primary radiation force	$M L T^{-2}$
\mathcal{F}	object function	
\mathcal{G}	projection function	
h	film thickness	L
h_c	critical film thickness	L
h_i	initial film thickness	L
h_m	minimum film thickness	L

SYMBOLS AND ABBREVIATIONS

\mathcal{H}	Heaviside function	
i	object index	
J_1	first-order Bessel function of the first kind	
k	Boltzmann's constant $k = 1.3807 \times 10^{-23} \text{ J K}^{-1}$	$\text{M L}^2 \text{ T}^{-2} \Theta^{-1}$
l_j	jet length	L
L	Ostwald coefficient	
m	mass	M
MI	mechanical index	
n	spherical harmonic mode	
n_*	refraction index	
n_{oil}	refraction index of oil	
n_{w}	refraction index of water	
N	number of bubble fragments	
NA	numerical aperture	
NA_{w}	reduced numerical aperture	
p	pressure (difference)	$\text{M L}^{-1} \text{ T}^{-2}$
p_0	ambient pressure	$\text{M L}^{-1} \text{ T}^{-2}$
p_1, p_2	pressure inside bubble 1, 2	$\text{M L}^{-1} \text{ T}^{-2}$
p_{ac}^-	peak rarefactional acoustic pressure	$\text{M L}^{-1} \text{ T}^{-2}$
$p_{\text{ac}}(t)$	acoustic pressure	$\text{M L}^{-1} \text{ T}^{-2}$
p_{f}	film pressure	$\text{M L}^{-1} \text{ T}^{-2}$
p_{LY}	Laplace-Young pressure	$\text{M L}^{-1} \text{ T}^{-2}$
p_{ov}	hydrostatic overpressure	$\text{M L}^{-1} \text{ T}^{-2}$
p_{wh}	water-hammer pressure	$\text{M L}^{-1} \text{ T}^{-2}$
$P(R)$	size distribution of a bubble population	
PSF	point-spread function	
r	radial distance	L
r_2	bubble center distance 2	L
R	bubble radius	L
\ddot{R}	second time derivative of R	L T^{-2}
R_0	equilibrium bubble radius	L
R_0^{tr}	transition radius	L
R_1, R_2	radius of bubble 1, 2	L
\dot{R}_1, \dot{R}_2	first time derivative of R_1, R_2	L T^{-1}
R_{c}	bubble radius just before collapse	L
R_{f}	liquid film radius	L
R_{j}	jet radius	L
R_{m}	mean bubble radius	L
ΔR_{m}	step in mean bubble radius	L

SYMBOLS AND ABBREVIATIONS

\mathcal{R}	resolution of the optical system	L
Re	Reynolds number	
RPNNP	Rayleigh, Plesset, Noltingk, Neppiras, and Poritsky	
t	time	T
Δt	time step	T
$t_{1/2}$	half-size time	T
$\Delta t_{1/2}$	difference in half-size times	T
Δt_d	diffusion time difference	T
T	temperature	Θ
T_p	pulse duration	T
u	relative approach velocity of bubble walls	$L T^{-1}$
UCA	ultrasound contrast agent	
v	velocity	$L T^{-1}$
\dot{v}	first time derivative of v	$L T^{-2}$
v_a	mean approach velocity	$L T^{-1}$
v_j	jet velocity	$L T^{-1}$
V_2	bubble volume 2	L^3
\ddot{V}_2	second time derivative of V_2	$L^3 T^{-2}$
V_b	bubble volume	L^3
V_j	jet volume	L^3
We	Weber number	
z	distance from the film center plane	L
α	maximum angle of incidence	
γ	coordinate in the object plane	L
Γ	coefficient defined by $\Gamma = \frac{\rho R^2 \ddot{R}}{\sigma}$	
δ_t	total damping coefficient	
ε	additive noise function	
ε_r	deformation	
ζ	segmented object diameter	L
ζ_i	segmented diameter of disk i	L
η	viscosity	$M L^{-1} T^{-1}$
θ	segmentation threshold value	
κ	compressibility	$M^{-1} L T^2$
λ	wavelength	L
ξ	segmented image	
Π	disjoining pressure	$M L^{-1} T^{-2}$
ρ	fluid density	$M L^{-3}$

SYMBOLS AND ABBREVIATIONS

ρ_g	gas density	$M L^{-3}$
σ	surface tension	$M T^{-2}$
τ	object diameter	L
τ_d	drainage time	T
τ_i	diameter of disk i	L
τ_{\max}	maximum stress	$M L^{-1} T^{-2}$
ϕ	object intensity	
ψ	background intensity	
Ψ	maximal excursion difference	
\varnothing	diameter	L

1

On Cavitation, High-speed Photography, and Medical Bubbles

1 Sound and bubbles

According to Oxford Advanced Learner’s Dictionary of Current English [68], popular science can be defined as organized knowledge suited to the taste or the education level of the general public. Since boiling water, opening soda bottles, and producing froth when pouring beer is probably “to the taste of the general public”, observing and investigating bubble behavior can be considered as popular science.

One of the first to organize his knowledge on this science was Leonardo da Vinci. Not only did he have a theory on oversaturation of water [154]:

“Moreover the elements repel or attract each other, for one sees water expelling air from itself, and fire entering as heat under the bottom of a boiler and afterwards escaping in the bubbles on the surface of the boiling water.”

He was also the first to describe the concept of surface tension [154]:

[1, 1]

MEDICAL BUBBLES AND PHOTOGRAPHY

“The centre of a particular sphere of water is that which is formed in the tiniest particles of dew, which is often seen in perfect roundness upon the leaves of plants where it falls; it is of such lightness that it does not flatten out on the spot where it rests, and it is almost supported by the surrounding air, so that it does not itself exert any pressure, or form any foundation; and because of this its surface is drawn towards its centre with equal force and they become magnets one of another, with the result that each drop necessarily becomes perfectly spherical, forming its centre in the middle, equidistant from each point of its gravity, it always places itself in the middle between opposite parts of equal weight.”

Leonardo da Vinci had theories on acoustics, too:

“I say that the sound of the echo is reflected to the ear after it has struck, just as the images of objects striking the mirrors are reflected into the eyes. And as the image falls from the object into the mirror to the eye at equal angles, so sound will also strike and rebound at equal angles as it passes from the first percussion in the hollow and travels out to meet the ear.”

As such, we may state that Leonardo da Vinci had already depicted the ingredients needed for contrast echography five hundred years ago.

Roughly two centuries after his death, Sir Isaac Newton did some gravity-related experiments with encapsulated bubbles [131, 132]:

“From the top of St. Paul’s Cathedral in London in June 1710, glass balls were dropped simultaneously in pairs, one full of quicksilver, the other full of air; and in falling they described a space of 220 London feet.”

Not until the work of Daniel Bernoulli [7] it was understood that negative pressure can be produced within a liquid. According to De Jong’s summary of historical technical aspects of cavitation [73], Euler & d’Alembert debated the consequences of negative pressures in the early eighteenth century. According to Euler, they would ultimately cause a rupture of the liquid, d’Alembert refused to accept this view.

Because of the Industrial Revolution, Euler’s view was supported by evidence. As steam turbines became more powerful, the rotation speed of ship-screw propellers increased dramatically. With the increased rotation

speed, an “extraordinarily rapid” kind of erosion of the propellers was observed [167]. Silberrad showed pictures of ship-screws and described the seriousness of this problem:

“These have been photographed from specimens cut from the first set of propellers of the Mauretania, and exhibited at the recent Anglo-Japanese Exhibition. These original propellers had three loose blades, and an over-all diameter of about 17 ft. The metal, it will be seen, is eaten away to the depth of in some cases more than 2 in. The financial aspect of the question was thus very serious. Propellers of the alloys in question cost anywhere between 130l. to 180l. a ton and have a scrap value of less than half that amount, while the rapidity of the wear was such that in the case of the Mauretania and Lusitania they would, had no remedy been found, have required replacing every few months, at a cost of some thousands of pounds, since each propeller weighed about 20 tons.”

As for the cause of the erosion, Silberrad stated:

“Further, it will be noted that the area attacked is, as has already been stated, near the hub. This was of large size, and it seems probable that there was a certain centrifugal action causing a reduction of pressure, and this region of reduced pressure was marked by the erosion. Here Dr. Silberrad considers that cavitation might occur, and, in consequence, water broken by intervening evacuated spaces with no air present.”

The word *cavitation* for the formation of cavities due to negative pressures has been attributed to Froude according to an article by Thornycroft & Barnaby on torpedo-boat destroyers, written in 1895 [180].

In 1917, Lord Rayleigh published a masterpiece on cavitation [150], starting with:

“When reading O. Reynolds’s description of the sound emitted by water in a kettle as it comes to the boil, and their explanation as due to the partial or complete collapse of bubbles as they rise through cooler water, I proposed to myself a further consideration of the problem thus presented; but I had not gone far when I learned from Sir C. Parsons that he also was interested in the same question in connexion with cavitation behind

[1, 1]

MEDICAL BUBBLES AND PHOTOGRAPHY

screw-propellers, and that at his instigation Mr. S. Cook, on the basis of an investigation by Besant, had calculated the pressure developed when the collapse is suddenly arrested by the impact against a rigid concentric obstacle. During the collapse the fluid is regarded as incompressible.

In the present note I have given a simpler derivation of Besant's results, and have extended the calculation to find the pressure in the interior of the fluid during the collapse. It appears that before the cavity is closed these pressures may rise very high in the fluid near the inner boundary.”

The equations presented are still applicable today.

Cavitation with a mechanical origin is called *hydraulic cavitation*. de Haller experimented in a laboratory environment with hydraulic cavitation on turbines [62]. A more recent study on hydraulic cavitation involves snapping shrimp: predator shrimp that kill their prey by producing cavitation bubbles that collapse near their victims [186]. Light is emitted from the collapsing cavities, a phenomenon dubbed *shrimpluminescence* [108].

Sound waves can create negative pressures, too, resulting into *acoustic cavitation*. To learn more about this subject, we have to look into the science of inaudible sound: *ultrasonics*.

In “Some Background History of Ultrasonics”, written in 1948, Klein called ultrasonography, or: *superaudible acoustics*, “a by-product of the two world wars” [91]:

“To trace the progress of ultrasonics from its beginning, it is necessary to recall the years 1914–1918 and Professor Paul Langevin who founded this subject. In 1915, the U-boat menace threatened the Allies. A Russian engineer named Chilowski submitted an idea for submarine detection to the French Government. The latter invited Langevin, then Director of the School of Physics and Chemistry in Paris, to evaluate it. Chilowski's proposal was to excite a cylindrical, mica condenser by a high frequency singing arc (Poulson Arc) operated at about 100 kc. This device was intended to be a generator of an ultrasonic beam for detecting submerged objects. The idea of locating underwater obstacles by means of sound echoes had been previously suggested by L.F. Richardson, in England. In 1912, following the Titanic disaster, he proposed to set a high frequency hydraulic whistle at the focus of a mirror and use the beam for locating submerged

navigational hazards. Sir Charles Parsons, the inventor of the vapor turbine, became interested in this device and built one in accordance to Richardson's ideas. This apparatus was found unsuitable for the job of searching underwater obstacles, but the idea was not lost.

(...)

“By making use of the piezoelectric effects of quartz, Langevin introduced the modern piston transducer. He became acquainted with piezoelectric phenomena while a student at the laboratory of the Curie brothers. Perhaps the most outstanding advance made by Langevin in this field was his theoretical calculation and experimental verification of the fact that a thin sheet of quartz sandwiched between two steel plates constituted an electromechanical resonant system.”

(...)

“Various aspects of the piezoelectric piston transducer were investigated by Langevin and his co-workers, among whom were a number of British and American scientists. They observed many biological and physical effects of the ultrasonic beam. For example, they noted in their laboratory tank that small fish were killed as they swam into the intense portion of the ultrasonic beam. Also, they saw incipient cavitation in the water when the sound source was active and felt painful effects upon the hand when struck in front of the beam.”

This is the first mentioning of acoustic cavitation.

But the cavities themselves produced sound waves as well. Bragg related the sound of drops falling into water to cavities [13]:

“When photographs are taken from below the surface, it becomes clear that an air cavity is often formed.”

(...)

“Now it appears that the note which we hear is the resonant note of this cavity, probably given out when the cavity has closed over

[1, 1]

MEDICAL BUBBLES AND PHOTOGRAPHY

at the top and burst again. My friend Richard Paget has actually measured these cavities in various cases and then made models of them in plasticine. Blowing across the top of the model cavity, he finds that its note is practically the same as that the drop makes when it falls. The note is very high, and has a frequency of two to three thousand vibrations a second.”

In 1933, Minnaert presented his theory for the sounds created by bubbles in water [127]:

“We will suppose that the bubbles give a sound because they pulsate in closing. Periodically the bubble expands and contracts, the surrounding water being the inert mass which is set in vibration, while the elasticity is due to the air of the bubble. A formula for the frequency of such pulsations may be derived in a quite elementary way.”

Thus, he formulated a theory on the resonance frequency of bubbles.

Noltingk & Neppiras were the first to formulate an equation to describe the behavior of gas filled and empty cavities in a sound field [133]. Many more would follow. An excellent overview on the historic development of physical models of the interaction of bubbles with acoustics was written by De Jong [73].

In 1954, not long after the introduction of clinical ultrasound [192, 193], Fox & Herzfeld hypothesized that cavitation bubbles grow from gas nuclei encapsulated by organic skins. Because of the skins, these nuclei would not be subjected to diffusive processes [50]. This hypothesis could also be read as follows: If gas bubbles encapsulated by an elastic shell are insonified, they may still act as cavitation nuclei.

Fourteen years later, Gramiak *et al.* experimented with saline to create *in vivo* air bubbles [59, 60]. These rapidly diffusing air bubbles generated a characteristic response to ultrasound, such that perfused vessels would appear “brighter” on echographic images. This new diagnostic technique was called ultrasound contrast imaging.

Since then, a range of agents consisting of “medical bubbles” have been developed [73, 78, 83, 51]. Most of the ultrasound contrast agents (UCAs) that are currently used in clinical diagnostics contain slowly diffusing gas microbubbles encapsulated by highly elastic shells, to prevent them from dissolving too quickly during application. After intravascular injection of an agent into the circulation, microbubbles will pass the site of interest

which is insonified by the clinician. Upon insonification, the microbubbles will generate a characteristic response, which is detected by the ultrasound scanner used. The resulting echographic image can then be interpreted by the clinician.

The encapsulated gas bubbles generally used in diagnostic ultrasound contrast studies vary in diameter from 1 to 10 μm . They have resonance periods in the microsecond range. If released, the gas dissolves in several to several hundreds of milliseconds.

Most studies on microbubble behavior have been based on the acoustic response from an ensemble of bubbles. With high-speed photography fast enough to surpass the bubble resonance periods, the observation of individual microbubble behavior has become possible.

2 A historical note on high-speed photography

We may define high-speed photography as the capturing of events that are more rapid than the human brain can process, approximately $1/15^{\text{th}}$ of a second.

According to Endelman [44], the beginning of high-speed photography “might be considered to be William Henry Fox Talbot’s experiment in 1851. He attached a page of the London Times newspaper to a wheel, which was rotated in front of his wet plate camera in a darkened room. As the wheel rotated, Talbot exposed a few square inches of the newspaper page for about $1/2,000^{\text{th}}$ of a second, using spark illumination from Leyden jars. This experiment resulted in a readable image.” In 1858, Thomas Skaife claimed to have captured a photograph of a mortar shell in flight [168]. The excerpt of the newspaper is shown in Figure 1.1.

The first multi-frame recording was done by Muybridge in 1878. He captured a sequence of 12 photographs of a trotting horse, shown in Figure 1.2. Exposure times were 2 ms and interframe times 40 ms. Over the next years photographic technology rapidly improved, stimulated by the development of cinematography. Roughly thirty years after Muybridge’s experiments, the first motion picture to embody a plot (The Great Train Robbery) was shown to the public [30].

Early applications of high-speed photography were mainly in ballistics, but also in fluid dynamics. The Mach brothers and Sir Boys published sharp photographs of flying bullets at the end of the nineteenth century [12, 111, 112, 110]. In 1887 and 1904, photographs of rough and

[1, 2]

MEDICAL BUBBLES AND PHOTOGRAPHY

before the death of Sir Henry Barnard, and that all important operations were decided upon with my concurrence, particularly with reference to the assault of Delhi, which was determined to be deferred till a sufficient force had been collected to insure success at a council of war presided over by me.

I remain, Sir, your most obedient servant,
THOMAS REED, Major-General.
United Service Club, May 12.

A FEAT IN PHOTOGRAPHY.

TO THE EDITOR OF THE TIMES.

Sir,—Permit me, through your world-wide journal, to inform your numerous photographic readers, that on the third and last firing of the 13-inch shell from the mortar battery at Woolwich Common, a few minutes before 12 o'clock this day, I succeeded (with permission of the authorities) in photographing stereoscopically, from behind the battery, the descending shell at the instant of its explosion, when in the air, within a few yards of the flagstaff target together with the target and the Artillery Engineers who fired the shell, which (I believe) unprecedented fact in photography was witnessed by Colonel Burrows, Acting-Commandant of the battery, and several other military gentlemen who were present at the time.

I am, Sir, yours obediently,
THOMAS SKAIFE.
Vanbrugh-house, Blackheath, May 27.

WANT PLACES.—All letters to be post paid.

WET NURSE. Married. First child. Good reference.—O. B., 49, Wellington-street, Woolwich.

WET NURSE. Age 26. Good breast of milk. First child, two months' old. Medical reference.—O. F., 1, Northampton-road, Wilmington-square, Clerkenwell.

NURSE (HEAD) in a nobleman's or gentleman's family. Age 33. 20 years' experience. Thoroughly understands all her duties. Highly recommended.—A. B., 1, Hereford-st., Mayfair.

NURSE (UPPER) in a nobleman's or gentleman's family, where a lady's-maid is kept. Accustomed to infants from the month. Character. Would travel.—X. Y. Z., 4, Crawford-st., Portman-sq.

Figure 1.1: Thomas Skaife's claim in *The Times*, London, of May 29, 1858. Reprinted with permission.

smooth spheres falling into water were published [195, 196]. An elaborate overview of the development of high-speed photography in the nineteenth and twentieth century is given by Fuller & Rendell [55].

Nowadays, high-speed cameras capable of taking multiple frames are equipped with either beam splitters that divide an image over several recording devices, or a rotating mirror sweeping the image over numerous recording devices. Although recording speeds of 200 million frames per second can be reached with the former camera type, the total number of frames available is currently 16. With the latter technology, recording

HIGH-SPEED PHOTOGRAPHY OF MEDICAL BUBBLES

[1, 3]

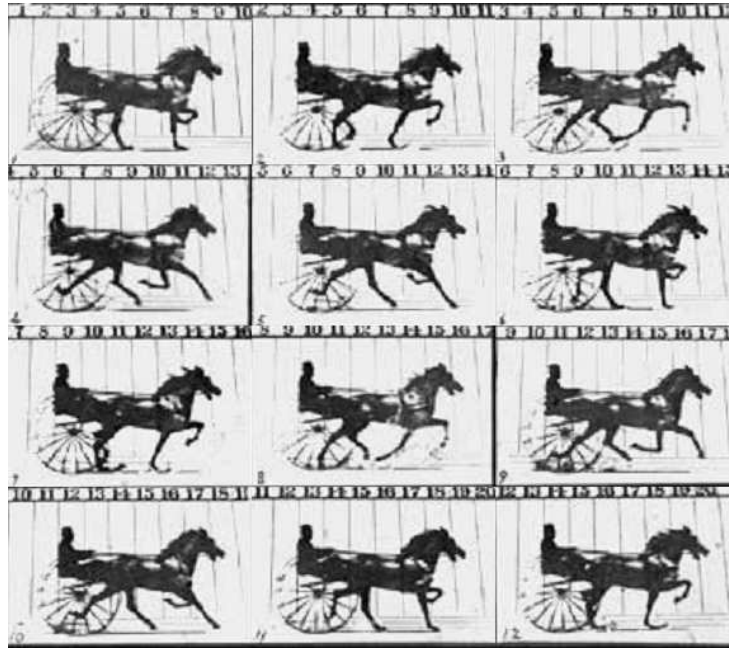


Figure 1.2: “Abe Edgington, owned by Leland Stanford; driven by C. Marvin, trotting at a 2:24 gait over the Palo Alto track, 15th June 1878.” Reprinted with permission from Muybridge HE. *The Horse in Motion 1878*. In: *Adolf Nichtenhauser history of motion picture collection ca. 1950*. Collection number MS C 380 located in: Modern Manuscripts Collection, History of Medicine Division, National Library of Medicine, National Institutes of Health, Department of Health and Human Services, Bethesda, MD.

speeds of 25 million frames per second can be reached, whereas the total number of frames is virtually unlimited.

3 High-speed photography of medical bubbles

Over the past years various studies were performed involving visualization of medical bubbles during ultrasound irradiation. Klibanov *et al.* [93] observed oscillations of UCA bubbles attached to a Petri dish with a 30 frames per second camera. Dayton *et al.* [34, 38] combined acoustical observations of UCA and optical observations with a 600 frames per sec-

[1, 3]

MEDICAL BUBBLES AND PHOTOGRAPHY

ond camera. They observed gas release and bubble destruction. Takeuchi [177, 178] used TV-frame synchronous illumination and insonification to observe microballoon breakage. Because of the low frame rates of the cameras mentioned, the instance of shell breakage and the behavior of a bubble within an ultrasound cycle could not be observed. Kuribayashi *et al.* [97] observed changes in UCA bubble diameters within one cycle of ultrasound, at frame rates up to 10 MHz and 50 \times magnification. They concluded that the imaging frame rate and magnification were not sufficient for studying the details of UCA bubble behavior. De Jong *et al.* [79] carried out a preliminary study on this subject. They proposed a method to visualize the oscillations of bubbles using a microscope and a fast framing camera operating at a 4 MHz frame rate. Furthermore, they compared radius-time curves, derived from two-dimensional bubble pictures, to a theoretical model. Morgan *et al.* [128] used a 100 megaframes per second camera in streak mode to predict bubble-oscillating behavior. More recently, May *et al.* [120] performed high-speed optical experiments on microbubbles with an outer lipid layer, an oil layer, and a gas core. Such microbubbles may have a future application in local drug delivery.

In our laboratory at Erasmus MC, we captured images of insonified encapsulated microbubbles at higher frame rates than the ultrasonic frequencies transmitted. We made use of a fast framing camera with a beam splitter, capturing 8 frames at a 3 MHz frame rate, and of the Brandaris-128 rotating mirror camera system, capturing 128 frames at frame rates around 13 MHz. The microbubbles observed have been applied for diagnostic purposes, and have potential therapeutic applications. The potential clinical applications of insonifying medical bubbles have been explored, based on high-speed optical observations, combined with bubble-sound theory.

An example of our results is shown in Figure 1.3, which shows a sequence of microscopic image frames of a freely flowing contrast agent microbubble. The frames were taken during one cycle of ultrasound insonification, with a center frequency of 500 kHz. The peak negative acoustic pressure at the region of interest was 0.85 MPa. Each frame corresponds to a $45 \times 27 \mu\text{m}^2$ area. The exposure time of each frame was 10 ns. Inter frame times were $0.33 \mu\text{s}$, except for the time between frames e and f, which was $0.66 \mu\text{s}$. The sequence shows an expanding medical bubble of $5.3 \mu\text{m}$ (a) and $17.6 \mu\text{m}$ (b), and its maximal expansion of $22.9 \mu\text{m}$ (c). After contracting to $20.2 \mu\text{m}$ (d), a violent effect is visible (e). The microbubble had been pushed to the lower left side of the frame, apparently by a water

HIGH-SPEED PHOTOGRAPHY OF MEDICAL BUBBLES

[1, 4]

jet that was projected through the microbubble at high speed, causing it to act as a microsyringe. A subframe shows the negative of the region of interest. Finally the deformed microbubble reoccurred as an asymmetric shape (f). Jetting behavior may find an application in drug delivery.

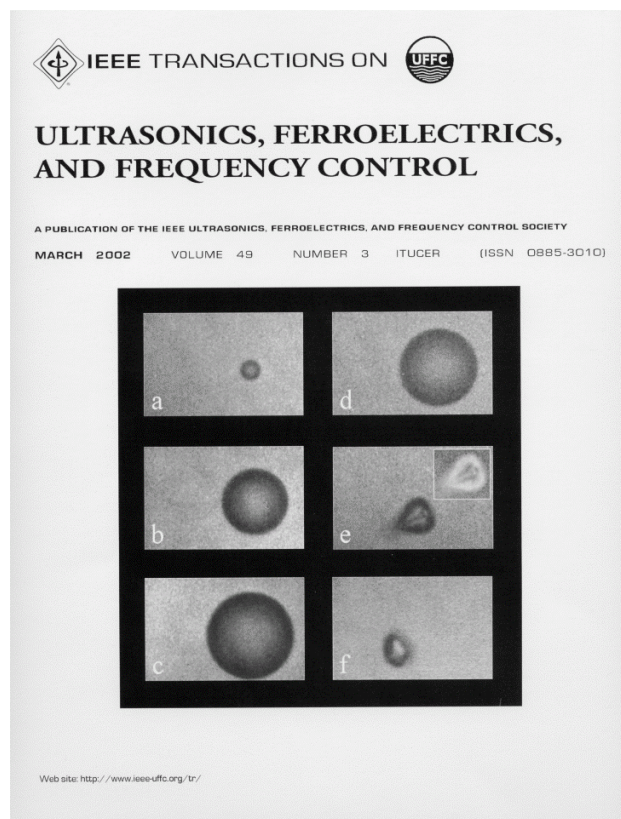


Figure 1.3: Medical bubble acting as a microsyringe. © 2002 IEEE. Reprinted with permission from Postema M, Bouakaz A, de Jong N. *IEEE Trans Ultrason, Ferroelect, Freq Contr* 2002 49(3):cover.

[1, 4]

MEDICAL BUBBLES AND PHOTOGRAPHY

4 Outline of this thesis

Chapter 2 describes a high-speed optical imaging system for capturing microbubbles. Pictures of contrast agent microbubbles under ultrasound insonification are analyzed. The ultrasound amplitudes used are in the clinical diagnostic range.

Chapter 3 reviews the mechanism of the coalescence (merging) of microbubbles. The mechanism is based on computations and on observations from high-speed camera images. Some potential medical applications are addressed.

Chapter 4 presents optical evidence of coalescing behavior of released gas bubbles. With these observations, the theory on expanding bubble coalescence can be validated.

Chapter 5 shows simulations of the diffusive behavior of gas microbubbles. Their applicability for diagnostic pressure measurements is discussed.

Chapter 6 reveals optical evidence for the dissolving behavior of gas bubbles simulated in Chapter 5. The release of gas from an encapsulated bubble is studied.

Chapter 7 gives an overview of types of behavior of microbubbles when insonified at high acoustic pressures. The potential clinical applications of these types of behavior are discussed.

Chapter 8 discusses general considerations and future prospects of medical bubbles.

2

Optical Simulations and Measurements of Microbubbles

Abstract

Ultrasound contrast agents (UCAs) are used in a clinical setting to enhance the backscattered signal from the blood pool to estimate perfusion and blood flow. The UCAs consist of encapsulated microbubbles, measuring 1-10 μm in diameter. Acoustic characterization of UCAs is generally carried out from an ensemble of bubbles. The measured signal is a complicated summation of all signals from the individual microbubbles. Hence, characterization of a single bubble from acoustic measurements is complex.

In this study, 583 optical observations of freely flowing, oscillating, individual microbubbles from an experimental UCA were analyzed. The excursions during ultrasound exposure were observed through a micro-

© 2003 IEEE. Reprinted with permission from Postema M, Bouakaz A, Chin CT, de Jong N. Simulations and measurements of optical images of insonified ultrasound contrast microbubbles. *IEEE Trans Ultrason Ferroelec Freq Contr* 2003 50(5):523-536.

This work has been supported by the Technology Foundation STW (RKG.5104) and by the Interuniversity Cardiology Institute of the Netherlands.

[2, 1]

IMAGES OF MICROBUBBLES

scope. Images were recorded with a high frame rate camera operating at 3 MHz. Microbubbles on these images were measured off-line and maximal excursions were determined. A technique is described to determine the diameters of the bubbles observed. We compared the maximal excursions of microbubbles of the same initial size in an ultrasound field with a 500 kHz center frequency at acoustic amplitudes ranging from 0.06 MPa to 0.85 MPa.

It was concluded that maximal excursions of identical bubbles can differ by 150% at low acoustic pressures (mechanical index or $MI < 0.2$). At a high acoustic pressure ($MI = 1.2$) an image sequence was recorded on which a bubble collapsed, while an apparently identical bubble survived.

1 Introduction

The detection of perfusion and blood flow is of great clinical interest, but technically challenging, because blood reflects ultrasound poorly. Reflections from blood can be increased by administering gaseous bubbles, due to their high echogenicity. Microbubble-based ultrasound contrast agents (UCAs) make blood better detectable in B-mode and Doppler mode imaging [4, 16, 74]. A wide variety of contrast agents is commercially available or under clinical trial and development [4]. De Jong & Ten Cate [83] gave an overview of clinical applications and technological innovations of ultrasound contrast agents. A review of current and near future detection procedures of UCAs was written in [80].

Most of the commercially available UCAs consist of encapsulated microbubbles of low solubility gas, measuring 1–10 μm in diameter. They are sufficiently stable to pass into the systemic circulation following injection into a peripheral vein. Nowadays, new generations of UCA are under investigation to further improve the scattering from blood and to ameliorate its detection in the presence of surrounding tissue. In addition to UCA design and development, increased interest is directed to the development of more sensitive ultrasound equipment to visualize UCA. Consequently, contrast echocardiography has become a rapidly evolving field encompassing a family of technologies and practices for the noninvasive assessment of cardiac structure and function. Recent developments in engineering of microbubbles and in adapted imaging systems such as triggered modality in combination with imaging techniques such as power Doppler, pulse inversion and power modulation imaging are facilitating simultaneous as-

INTRODUCTION

[2, 1]

assessment of myocardial function and perfusion [4, 75]. Despite these new imaging techniques, myocardial contrast echocardiography has to overcome several problems if it is to be able to quantify myocardial blood flow. These limitations can be surmounted with a better understanding of the behavior of a single microbubble in an ultrasound field. As a matter of fact, the interactions of microbubbles with an ultrasound beam are complex. When a microbubble is exposed to an oscillating acoustic signal, it undergoes alternate expansions and contractions, equal and symmetrical at low acoustic powers, *i.e.*, mechanical index (MI) < 0.1. The mechanical index is defined as

$$MI = \frac{p_{ac}^-}{\sqrt{f}}, \quad (2.1)$$

where p_{ac}^- is the peak rarefactional acoustic pressure normalized by 1 MPa and f is the center frequency of the ultrasound normalized by 1 MHz. As the acoustic power increases, more complex nonlinear interactions occur. This oscillating behavior is associated with the production of harmonic signals. At still higher powers, highly nonlinear behavior is associated with complex bubble behavior, which can be revealed by phenomena like bubble rupture, fragmentation, and merging.

An improved understanding of contrast bubble properties and behavior under the influence of ultrasound may lead to more sophisticated detection techniques. Until now, mostly ultrasonic measurements supported by theoretical models were adopted to elucidate and quantify the interaction between ultrasound beam and contrast gas bubbles [82, 81, 29, 67, 54]. The experiments were mostly performed on an ensemble of gas bubbles with certainly a range of different sizes and possibly different shell parameters. Therefore, these studies express a bulk response of a majority of bubbles. Hence, the behavior and contribution of individual bubbles becomes difficult to predict. To make more thorough investigations on individual bubble response to ultrasound excitation, and by that develop new detection techniques, optical visualization of oscillating bubbles represents an attractive alternative. Over the past years various studies were performed involving visualization of gas bubbles during ultrasound irradiation. Klibanov *et al.* [93] observed oscillations of UCA bubbles attached to a Petri dish with a 30 frames per second camera. Dayton *et al.* [34, 38] combined acoustical observations of UCA and optical observations with a 600 frames per second camera. They observed gas release and bubble destruction. Takeuchi [177, 178] used TV-frame synchronous illumination

[2, 2]

IMAGES OF MICROBUBBLES

and insonification to observe microballoon breakage. Because of the low frame rates of the cameras mentioned, the instance of shell breakage and the behavior of a bubble within an ultrasound cycle could not be observed. Kuribayashi *et al.* [97] observed changes in UCA bubble diameters within one cycle of ultrasound, at frame rates up to 10 MHz and 50 \times magnification. They concluded that the imaging frame rate and magnification were not sufficient for studying the details of UCA bubble behavior. De Jong *et al.* [79] carried out a preliminary study on this subject. They proposed a method to visualize the oscillations of bubbles using a microscope and a fast framing camera operating at a 4 MHz frame rate. Furthermore, they compared radius-time curves, derived from two-dimensional bubble pictures, to a theoretical model. Morgan *et al.* [128] used a 100 megaframes per second camera in streak mode to predict bubble-oscillating behavior.

In this study, 583 optical observations of freely flowing, oscillating, individual microbubbles from an experimental UCA were analyzed. The excursions during ultrasound exposure were observed through a microscope. Images were recorded with a high frame rate camera operating at 3 MHz. Microbubbles on these images were measured off-line and maximal excursions were determined. A technique is described to precisely determine the diameters of the bubbles observed. We compared the maximal excursions of microbubbles of the same initial size in an ultrasound field with a 500 kHz frequency at acoustic amplitudes ranging from 0.06 MPa to 0.85 MPa. Furthermore, examples are shown of two-dimensional observations, revealing bubble-collapse and bubbles merging. In addition, the results are compared to theory.

2 Optical imaging theory and simulations

The optical system was studied to determine the relation between observed bubble sizes and true bubble sizes. To measure a bubble from an optical image, it has to be segmented from the background of the image. The measurement depends on the characteristics of the optical system and on the segmentation technique applied. In this section a segmentation technique is applied to simulated images to estimate the precision of our optical system.

An optical image of a radially symmetric flat object in focus, observed through a microscope, can be expressed as the following illumination in-

tensity function:

$$\mathcal{G}(r) = \int_{-\infty}^{\infty} \text{PSF}(r - \gamma) \mathcal{F}(\gamma) d\gamma + \varepsilon(r), \quad (2.2)$$

where r is the coordinate in the image plane, γ is the coordinate in the object plane, \mathcal{G} is the intensity of the image observed, PSF is the point-spread function of the optical imaging system, \mathcal{F} represents the illumination intensity of the object, and ε is a one-dimensional additive noise function [1, 72]. The PSF, derived from geometrical optics, is given by [198, 101]:

$$\text{PSF}(r) = \left(2 \frac{J_1(\alpha r)}{\alpha r} \right)^2, \quad \alpha = \frac{2\pi \text{NA}}{\lambda}, \quad (2.3)$$

where J_1 is the first-order Bessel function of the first kind, NA is the numerical aperture of the objective lens,* and λ is the wavelength of the light. The PSF of our optical system was computed for NA = 1.25 and $\lambda = 500 \text{ nm}$. The resolution \mathcal{R} of an optical system is defined by the Rayleigh criterion [149]

$$\text{PSF}\left(\frac{1}{2}\mathcal{R}\right) = 0, \quad (2.4)$$

which holds for

$$\mathcal{R} = 1.22 \frac{\lambda}{\text{NA}}. \quad (2.5)$$

To simulate the imaging in focus, we defined five differently sized circularly symmetric objects \mathcal{F} : the Heaviside function

$$\mathcal{H}(r) = \begin{cases} 1, & r \geq 0 \\ 0, & r < 0 \end{cases}, \quad (2.6)$$

and four disks with diameters τ of $1 \mu\text{m}$, $0.5 \mu\text{m}$, $0.2 \mu\text{m}$, and $0.1 \mu\text{m}$, respectively. τ_i corresponds to the true diameter of disk i . By applying (2.2) to \mathcal{F} and assuming $\varepsilon = 0$, simulated images \mathcal{G} were obtained [Figure 2.1]. To obtain the true object diameters from the obtained images, the objects

*The numerical aperture is given by

$$\text{NA} = n_* \sin \alpha$$

where n_* is the refraction index of the material between the object plane and the objective lens, and α is the maximum angle of incidence relative to the optical axis.

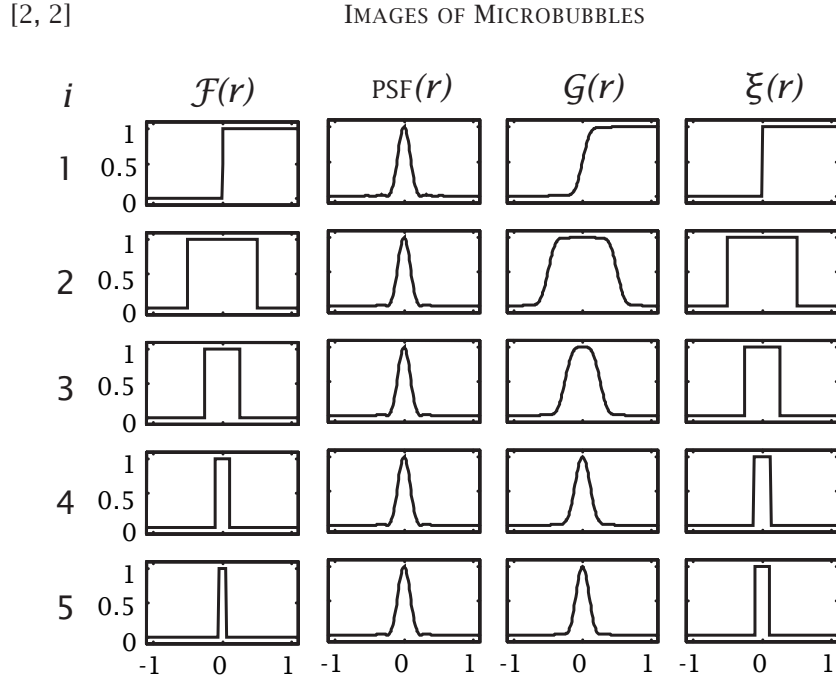


Figure 2.1: One-dimensional, differently sized objects \mathcal{F} , convolved with the PSF, resulting in optical images \mathcal{G} . Segmented objects ξ were obtained after applying the threshold $\theta = 0.5$.

had to be segmented. A common method to discriminate objects from the background in optical images is to segment the image into:

$$\xi(r) = \begin{cases} 1, & \mathcal{G}(r) \leq \theta \\ 0, & \mathcal{G}(r) > \theta \end{cases}, \quad (2.7)$$

where ξ represents the segmented image and θ is the gray-level used as a threshold value; (2.7) segments objects that are lighter than the background. This segmentation technique is called gray-level window-slicing [72]. Window-slicing was applied to the images \mathcal{G} in Figure 2.1. A threshold value $\theta = 0.5$ was used for segmentation, corresponding to a threshold level halfway between imaged object intensity $\mathcal{G} = 1$ and background $\mathcal{G} = 0$. The segmented values ξ are plotted as a function of lateral distance r . We define ζ_i as the diameter of a segmented object in image i . We show in Table 2.1 that ζ_i corresponds to the true object diameter τ_i , except for objects $i = 4$ and $i = 5$. The disk sized τ_5 is too narrow to be detected with

Object i	Object diameter $\tau (\mu\text{m})$	Segmented object diameter $\zeta (\mu\text{m})$
1	∞	∞
2	1.0	1.0
3	0.50	0.50
4	0.20	0.24
5	0.10	0.22

Table 2.1: True and segmented object diameter.

a threshold of 50% between object intensity and background under conditions similar to those of our optical system. For disks in the size range $50 \text{ nm} \leq \tau \leq 2 \mu\text{m}$, simulated images $\mathcal{G}(r)$ were calculated. The previously described 50% threshold $\theta = 0.5$ was applied for segmentation. The resulting measured diameters ζ were plotted as a function of τ [Figure 2.2]. For $\tau > 0.35 \mu\text{m}$, the measured object diameter was equal to the true object diameter ($\zeta = \tau$). Thus, true object diameters larger than $0.35 \mu\text{m}$ can be determined from one-dimensional, gray-scaled, monochromic optical images with a 50% threshold between object intensity and image background. For objects smaller than $\approx 0.35 \mu\text{m}$, the measured diameters deviate from the true diameters and approach half of the resolution \mathcal{R} of the optical system.

We investigated the influence of the threshold value on the measured diameters. Figure 2.3 shows the measured diameter ζ as a function of applied threshold θ for three differently sized disks. The slopes of the curves are determined by the PSF. For thresholds $0.3 \leq \theta \leq 0.7$, measured diameter ζ equals true diameter $\tau \pm 0.1 \mu\text{m}$, which means that flat object diameters can be determined with $0.1 \mu\text{m}$ precision. The effects of defocusing have been mathematically described by [172, 56, 155, 39]. When an object is large compared to the PSF, only the slope of the edge is changed by defocusing. Hence, the threshold $\theta = 0.5$ is still applicable [61]. A three-dimensional object can be considered as a stack of infinitely thin two-dimensional layers [1, 147, 66]. When three-dimensional objects are imaged through a microscope, the image projected onto the charge coupled device (CCD) element consists of contributions from all layers. A sphere is considered in focus when the middle layer of the sphere is in the focal plane [39, 66]. Bubbles which are large compared to the resolution

[2, 3]

IMAGES OF MICROBUBBLES

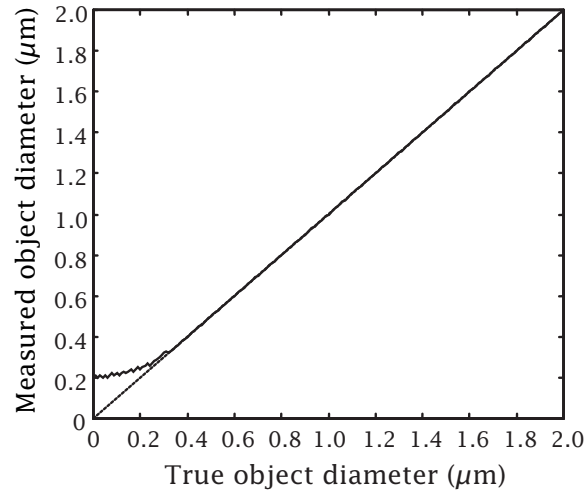


Figure 2.2: Measured object diameter (ζ) versus true object diameter (τ) after segmentation using the threshold $\theta = 0.5$.

have to be considered as part of the optical system [87]. Hence, images from an axial shift above the focal plane are not necessarily identical to the images from the same shift below the focal plane.

3 Experimental setup

An overview of the experimental setup for taking pictures of oscillating contrast agent microbubbles is shown in Figure 2.4. A computer controlled the triggering of a waveform generator, a Xenon flash source, and a fast framing camera. The electrical signal generated by the LW 420A waveform generator (LeCroy Corp., Chestnut Ridge, NY), typically consisting of 10 cycles at 500 kHz, was adjusted by two variable 355C/D attenuators (Hewlett Packard Company, Palo Alto, CA) in series, and an A-500 60 dB linear power amplifier (ENI technology, Inc., Rochester, NY). It was converted to ultrasound by a v389-SU 500 kHz single-element transducer (Panametrics Inc., Waltham, MA), spherically focused at 7.5 cm. The transducer was mounted in a Perspex container at an angle of 45° relative to the lid of the container, as shown in Figure 2.5. This container was filled with saturated water. A $\varnothing 200 \mu\text{m}$ cellulose Cuprophan[®] capillary tube

EXPERIMENTAL SETUP

[2, 3]

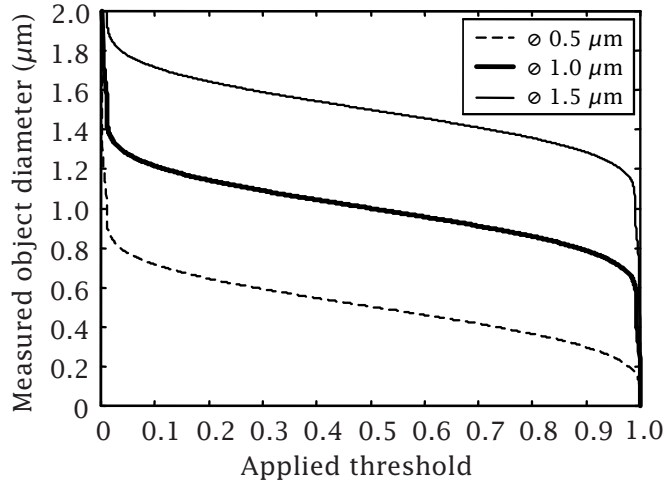


Figure 2.3: Measured object diameter (ζ) as a function of applied threshold (θ) for three different object diameters.

(Membrana GmbH, Wuppertal, Germany) was fixed in the focal area of the transducer, through which contrast agent was flowing. Because the wall of the capillary tube had been impregnated with water and because the tube was much smaller in diameter than the acoustic wavelength, it was not expected to interfere with the ultrasound transmitted. Without contrast agent inserted, we did not observe reflections from the tube. Underneath the capillary tube either a \varnothing 5 mm or a \varnothing 7 mm optic fiber was fixed, that was mounted to a modified Xenon flash source. This light source was triggered by a PM 5716 pulse/delay generator (Koninklijke Philips Electronics N.V., Eindhoven, The Netherlands).

The container was positioned beneath a BH-2 microscope (Olympus Optical Co., Ltd., Tokyo, Japan) with an SPlan 100 oil immersion objective lens (Olympus Optical Co., Ltd.) with numerical aperture $NA = 1.25$. Because we did not use oil but water between the objective lens and the capillary tube, the numerical aperture was reduced to

$$NA_w = \left(\frac{n_w}{n_{oil}} \right)^{1.3} NA^{1.25} = 1.1, \quad (2.8)$$

where NA_w is the reduced numerical aperture, n_w is the refraction index

[2, 3]

IMAGES OF MICROBUBBLES

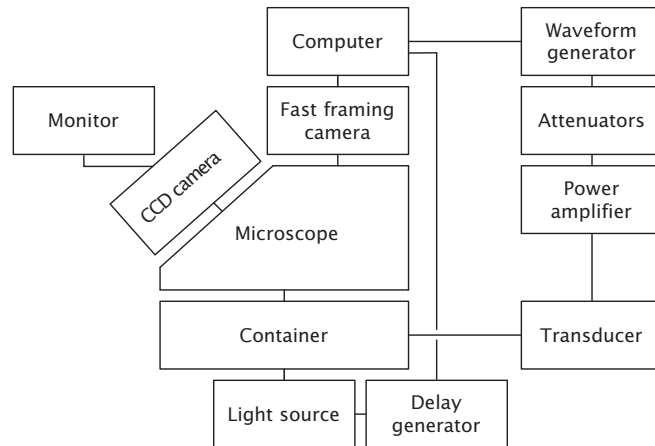


Figure 2.4: Basic setup for taking UCA microbubble pictures.

of water, and n_{oil} is the refraction index of oil. Because the reduced numerical aperture is much higher than 0.6, our optical system still could be considered a high-NA imaging system [47]. For focusing and calibration purposes, a WAT-902HS CCD camera (Watec Co., Ltd., Yamagata, Japan) was fitted to the eye-piece of the microscope. Focusing was done manually at the middle of the cellulose tube. Because the tube was wide compared to the contrast microbubbles measured, its upper half was considered a flat surface between contrast microbubbles and object lens, not causing aberrations but theoretically lowering the dynamic range of the images. The optical observations were recorded with an Imacon 468 fast framing camera (DRS Hadland, Ltd., Tring, UK), capable of recording eight two-dimensional frames at 100 MHz. In all observations, the first frame was taken a few microseconds before ultrasound waves reached the contrast agent. The other seven frames were taken during ultrasound insonification, with 330 ns interframe time for 500 kHz ultrasound, spanning a full ultrasound cycle. Frame exposure times ranged from 10 ns to 70 ns. A photograph of the optical observation part of the setup is shown in Figure 2.6.

We investigated an experimental UCA (supplied by Bracco Research SA, Geneva, Switzerland). It consists of phospholipid-encapsulated gas bubbles ranging in diameter from 1 to 6 μm with a median of 2 μm . The acous-

EXPERIMENTAL SETUP

[2, 3]

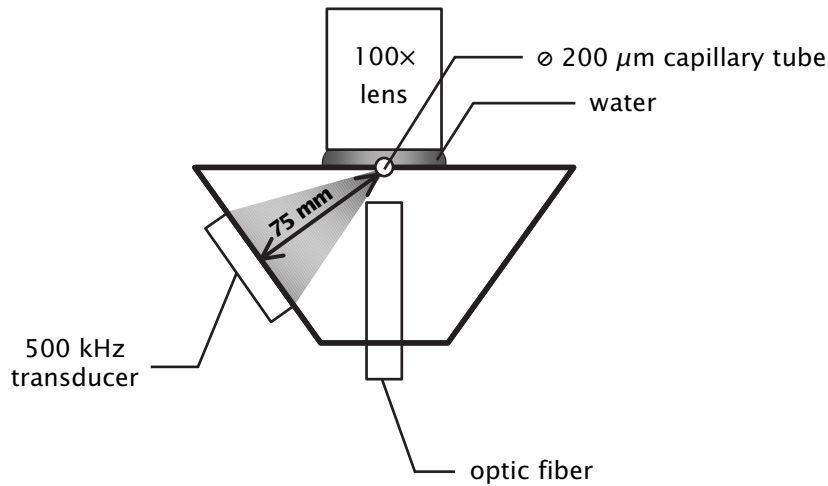


Figure 2.5: Front-side view of container.

tic behavior of a very similar contrast agent was modeled and described in [58]. In this article we make use of the parameters from this model. The UCA bubbles were insonified by 500 kHz ultrasound at peak rarefactional acoustic pressures between 0.06 and 0.85 MPa. Acoustic pressures applied were measured with a calibrated MH28-10 hydrophone (FORCE Technology, Brøndby, Denmark) in a separate water tank. Figure 2.7 displays the acoustic signal measured at the transducer focus, after transmitting 10 cycles of ultrasound at 210 kPa peak rarefactional pressure. It is assumed the *in-situ* acoustic signal is comparable to the signal measured.[†]

Undiluted UCA (5ml of a 0.9% sodium chloride dilution, added to a 25 mg UCA vial) was inserted through the capillary tube using either a syringe pressed by hand or a hose operated by a gravity fed or pumped infusion.

Furthermore, we did observations of diluted Quantison™ (Upperton Limited, Nottingham, UK) UCA, freely flowing underneath a glass coverslip.

The measuring of the numerous experimental UCA microbubbles was done with a partly automated method, using a MATLAB® (The MathWorks,

[†]In a separate experiment the *in-situ* reverberant component due to the presence of the microscopic lens was observed to be less than -14 dB, with a delay of 4 μs.

[2, 3]

IMAGES OF MICROBUBBLES

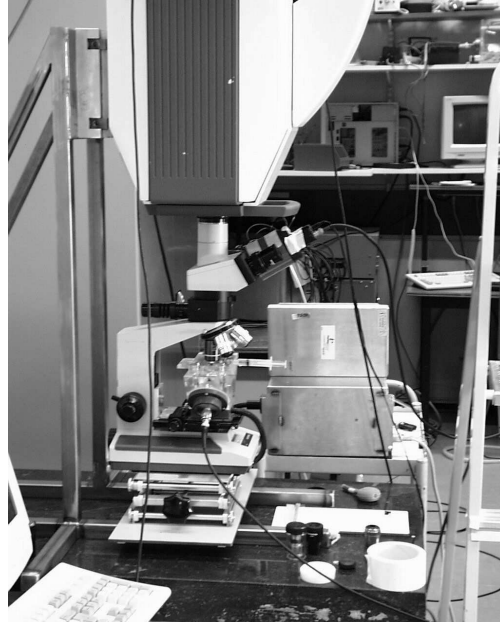


Figure 2.6: Optical observation part of the experimental setup.

Inc., Natick, MA) program. From previously recorded images, bubbles were selected for off-line measurement. These bubbles were selected only if they were visibly sharp, both before ultrasound arrival and in maximal expansion phase. Around each bubble to be measured, a rectangular region of interest was selected manually, which was much larger than the bubble [Figure 2.8(a) and (b)]. The background level ψ of the region of interest was determined automatically by calculating the median gray-value of the region of interest. The darkest value ϕ inside the region of interest was taken automatically as representative for the bubble wall. Segmentation was done by automatically applying the 50% threshold

$$\theta = \frac{1}{2} (\phi + \psi) \quad (2.9)$$

to the selected region of interest of the image [Figure 2.8(c)]. Due to nonuniform illumination and dark spots outside the bubble wall, the segmented bubble would sometimes not be represented by a circular shape. In those cases the threshold was set manually to a value typical for the

RESULTS

[2, 4]

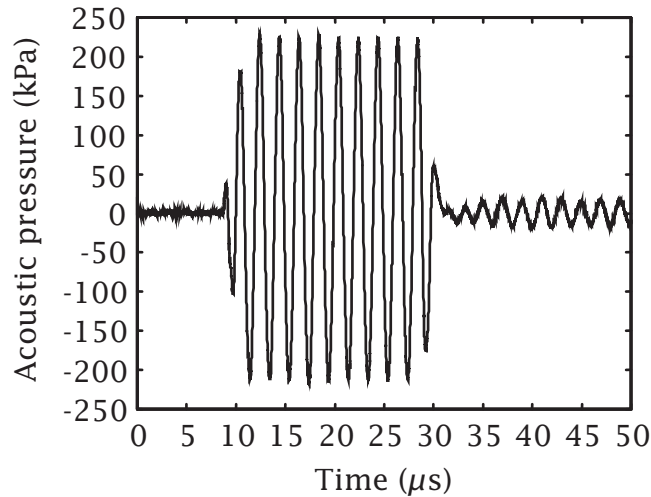


Figure 2.7: Acoustic signal measured at the transducer focus.

particular region of interest. If the resulting image did not appear to have a continuous circular shape, the measurement would not be taken into account. Individual circular areas were selected manually to be measured. Segmented points outside a selected circular area were removed automatically and the area inside the circular area was filled automatically [Figure 2.8(d)]. The bubble cross-section area A was measured by summation of all points of the circular area [198, 117]. Bubble diameters \mathcal{D} were calculated with the equation

$$\mathcal{D} = 2\sqrt{\frac{A}{\pi}}. \quad (2.10)$$

4 Results

Object size measurements

To perform measurements on flat, circular objects, a test grid was built (DIMES/TU Delft, Delft, The Netherlands). It consists of differently sized transparent triacontakaidigons (32-sided polygons) on a dark background,

[2, 4]

IMAGES OF MICROBUBBLES

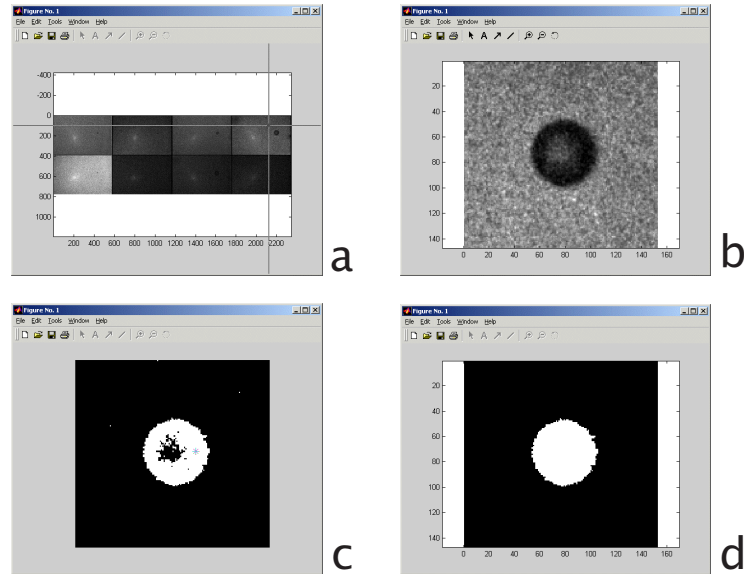


Figure 2.8: Semi-automated segmentation. Selection of region of interest (a) and (b), binary segmented image (c), segmented object (d).

each specified by the diameter of the biggest circle fitting inside the triacontakaidigon. From measurements of a 228.0 cycles/mm grid on a negative 1951 USAF glass slide resolution target (Edmund Industrial Optics, Barrington, NJ) [140] it was appreciated that identical transparent and dark objects were measured the same width. Hence, the results of measurements of transparent triacontakaidigons on a dark background are expected to be the same as those of measurements of dark triacontakaidigons on a transparent background. Figure 2.9(i) shows two 8-bit optical images of the test grid, recorded with the WAT-902HS CCD camera (Watec Co., Ltd.). The image size corresponds to a $43 \times 32 \mu\text{m}^2$ area. The median intensity ϕ inside triacontakaidigon 1 was $\phi = 187$ and the median background value ψ was $\psi = 28$, giving a 50% threshold level of $\theta = 1/2(\phi + \psi) = 107.5$. This threshold was applied to both images [Figure 2.9(ii)]. From the measured areas, the respective diameters were calculated and corrected for the polygon shape. These values are summarized in Table 2.2. Triacontakaidigon 11 was too small to be measured. For circles $\phi > 1 \mu\text{m}$, measured values differ from specified values on the order of 1%.

RESULTS

[2, 4]

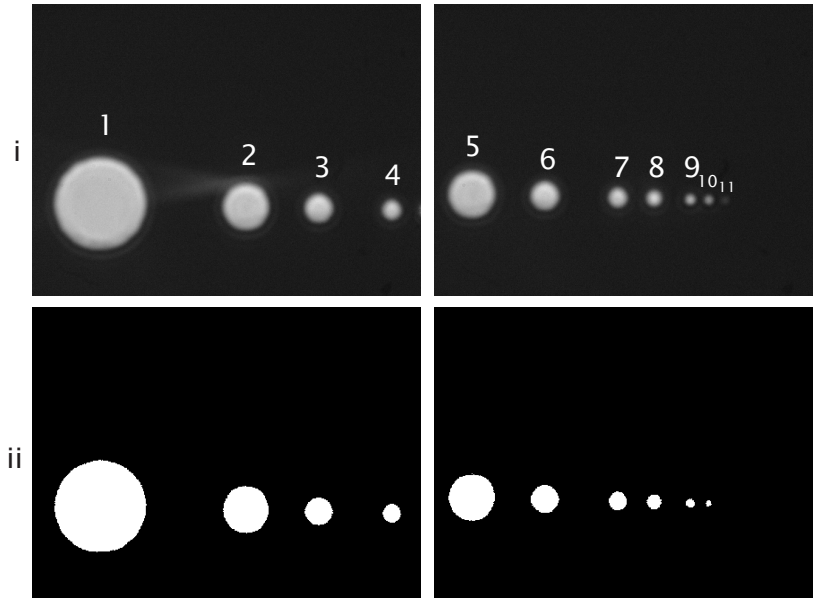


Figure 2.9: CCD images of 11 triacontakaidigons (i) on a calibration grid, (ii) segmented with a $\theta = 1/2(\phi + \psi)$ threshold.

We studied if the threshold $\theta = 0.5$ is still applicable if a sphere is slightly out of visual focus. Figure 2.10 shows four images of a $5 \mu\text{m}$ glass microsphere (Structure Probe, Inc., West Chester, PA), recorded with a CCD camera through our optical system. Figure 2.10(c) is in visual focus. Figure 2.10(b) and (d) were taken $2 \mu\text{m}$ proximal and $2 \mu\text{m}$ distal to the focus, respectively. Figure 2.10(a) was taken $4 \mu\text{m}$ proximal to focus. The same threshold, determined from the median background value and the darkest bubble wall values, was applied to all four of the images. From each binary-segmented image, the size of an enclosed area representing a sphere was measured. From this area the microsphere diameter was calculated. The diameters calculated from Figure 2.10(b) and (c) were $5.01 \mu\text{m}$; the diameter calculated from Figure 2.10(d) was $4.95 \mu\text{m}$. The diameter could not be calculated from Figure 2.10(a), which was too far out of focus. Based on these measurements with calibration spheres, we assume that diameters from bubbles that were slightly out of focus could be correctly measured with the threshold used.

Characteristic aberration was observed when a large part of the bubble

[2, 4]

IMAGES OF MICROBUBBLES

32-gon	Specified diameter (μm)	Measured diameter (μm)
1	10.0 ± 0.1	10.03
2	5.0 ± 0.1	5.06
3	3.0 ± 0.1	3.02
4	2.0 ± 0.1	1.99
5	5.0 ± 0.1	5.06
6	3.0 ± 0.1	3.03
7	2.0 ± 0.1	1.99
8	1.6 ± 0.1	1.60
9	1.0 ± 0.1	0.96
10	0.8 ± 0.1	0.66
11	0.4 ± 0.1	—

Table 2.2: Specified and measured diameters of triacontakaidigons.

was between focal plane and objective lens, as demonstrated in the next two figures. Figure 2.11 shows optical images of highly stable Quantison™ (Upperton Limited) UCA microbubbles placed underneath a glass coverslip and shifted through the visual focus of our optical system. Each frame corresponds to a $43 \times 32 \mu\text{m}^2$ area. Figure 2.11(e) is in visual focus. The bubbles that were below the focal plane got fuzzy rims [Figure 2.11(g), (h), (i)], whereas bubbles largely above the focal plane got bright centers with optical interference patterns around them [Figure 2.11(a) and (b)]. Figure 2.12 displays a collection of randomly taken pictures of freely flowing, ultrasound insonified, experimental UCA microbubbles. Figure 2.12(a) and (f) contain bubbles with a bright center, which are considered to be out of focus, and some sharp bubbles in the lower part of the frames. Figure 2.12(b), (c), (d), and (e) contain both sharp and fuzzy, unsharp bubbles that are comparable in size. Bubbles that were clearly out of focus were not taken into account in this study.

We quantified the errors caused by our optical recording system and our segmentation procedure [171]. The precision of the bubble diameter measurement is dependant of axial focus deviation of the bubble, light intensity, uniformity of illumination, CCD channel, multichannel plate amplification, and choice of region of interest. Because the choice of the region of interest is directly related to the threshold to be used, we do not have to consider this error separately. As we demonstrated with the two-

RESULTS

[2, 4]

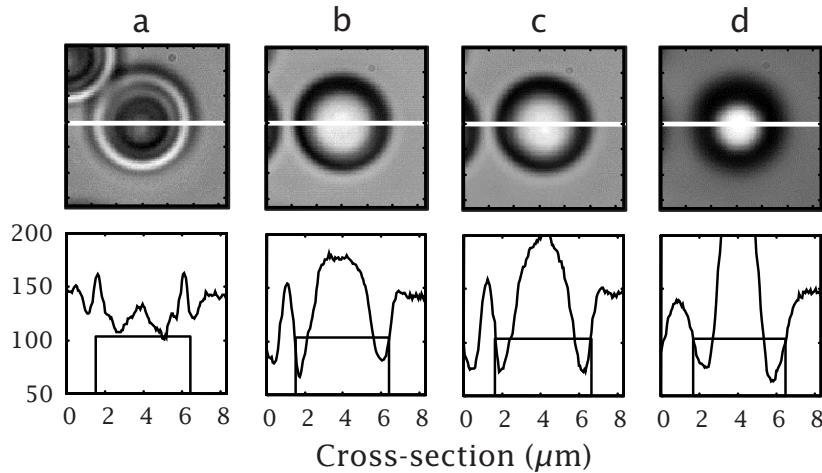


Figure 2.10: Intensity cross-sections of a $5 \mu\text{m}$ glass calibration particle, $4 \mu\text{m}$ proximal to focus (a), $2 \mu\text{m}$ proximal to focus (b), in focus (c), and $2 \mu\text{m}$ distal to focus (d).

dimensional simulations, a slightly changed threshold value from the 50% level between object and background intensity will not cause a systematic error. Because we only measured bubbles that were in visual focus, and we found no error from spheres that were slightly out of focus, the error caused by defocusing is considered negligible for our measurements. The random error, caused by light intensity, uniformity of illumination, CCD channel, and multichannel plate amplification, was calculated from 184 separate measurements of bubble diameters from 21 different bubbles on image sequences of freely flowing experimental UCA and freely flowing gas bubbles. The bubbles were in visual focus. They were not insonified with ultrasound. Their diameters ranged from $1.4 \mu\text{m}$ to $28 \mu\text{m}$. The gain of each CCD was varied, as was the exposure time, resulting in different illumination per frame. In each frame, the same region of interest was selected. For each bubble, the mean diameter was calculated. The largest and the smallest diameter measured were used to calculate the maximal deviation from the mean diameter due to random error. The maximal deviations are plotted in [Figure 2.13] as a function of the mean bubble diameter measurements. The figure shows that the values of the random error do not exceed 9% of the mean diameter.

[2, 4]

IMAGES OF MICROBUBBLES

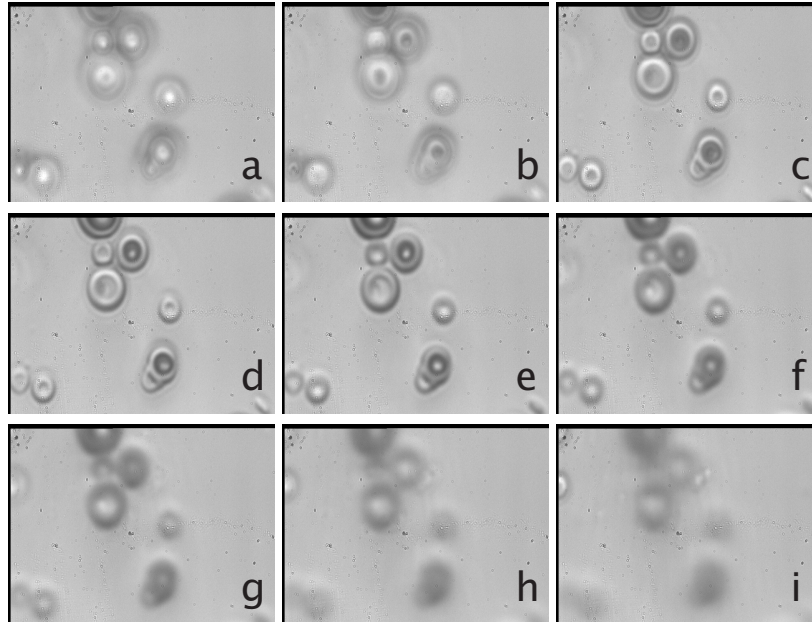


Figure 2.11: Quantison™ contrast microbubbles above the focal plane of the optical system (a)–(d), shifted through visual focus (e), below the focal plane (f)–(i). Each frame corresponds to a $43 \times 32 \mu\text{m}^2$ area.

Insonified UCA measurements

In this study, 583 results of initial diameter and maximal diameter measurements of insonified bubbles, selected from 1320 events, were subjected to an exhaustive analysis. Peak rarefactional acoustic pressures applied to these bubbles ranged from 0.06 MPa to 0.85 MPa. Bubble diameters were measured, using the 50% threshold between darkest foreground and median background, as described in the previous section. Figure 2.14 summarizes the data from events at four different acoustic pressures, corresponding to mechanical indices of $MI = 0.089$, $MI = 0.15$, $MI = 0.25$, and $MI = 0.39$. Maximal diameters were plotted as a function of initial bubble diameters. As Figure 2.14 shows, the bubbles investigated had initial diameters ranging from $1 \mu\text{m}$ to $4 \mu\text{m}$. We found no observations for initial diameters larger than $3 \mu\text{m}$ at $MI = 0.25$ [Figure 2.14(c)] and at $MI = 0.39$ [Figure 2.14(d)], in contrast to the observations at $MI = 0.089$ [Figure 2.14(a)]

RESULTS

[2, 4]

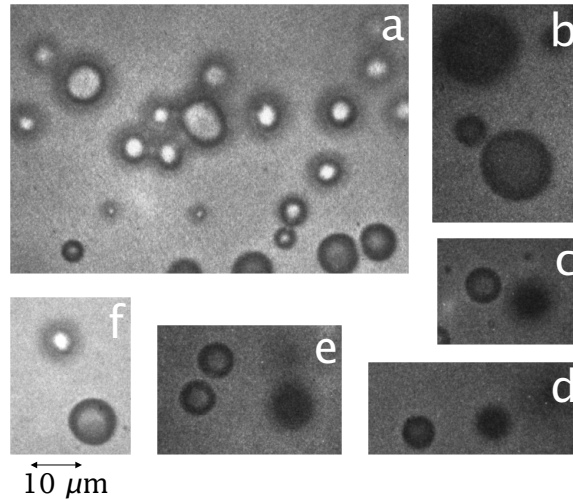


Figure 2.12: Randomly taken pictures of freely flowing, ultrasound insonified, experimental UCA. Bubbles with a bright center are considered to be out of focus (a), (f). Sharp and unsharp, fuzzy bubbles are comparable in size (b)–(e)

and at $MI = 0.15$ [Figure 2.14(b)]. The resonance size corresponding to the scanning frequency used, is estimated from theory [129] at $13.4 \mu\text{m}$. Therefore, the range of sizes studied is mainly located in the acoustic Rayleigh scattering zone. This is clearly shown in Figure 2.14, in which the maximal bubble expansion increases for larger bubbles, especially at the lowest acoustic pressure applied. At higher pressures, the slope of increase in bubble expansion as a function of initial diameter is steeper. This demonstrates that bubbles at these pressures undergo strong nonlinear oscillations. In addition, we can appreciate for all acoustic pressures applied that bubbles with the same initial diameter can oscillate differently, leading to different maximal expansions. This phenomenon is more pronounced at higher acoustic pressures. At $MI = 0.15$, 15 microbubbles in the range $2.8 \mu\text{m}$ to $3.2 \mu\text{m}$ reached maximal diameters between $3.2 \mu\text{m}$ and $7.6 \mu\text{m}$. This corresponds to a maximal difference in excursion of $\Psi = 151\%$. At $MI = 0.25$ we observed 25 microbubbles in the range $1.8 \mu\text{m}$ to $2.2 \mu\text{m}$ expand to maximal diameters between $2.5 \mu\text{m}$ and $8.8 \mu\text{m}$, corresponding to $\Psi = 340\%$.

To further explore these large differences in maximal expansion, we investigated the bubble response at high MI . An example of this investiga-

[2, 4]

IMAGES OF MICROBUBBLES

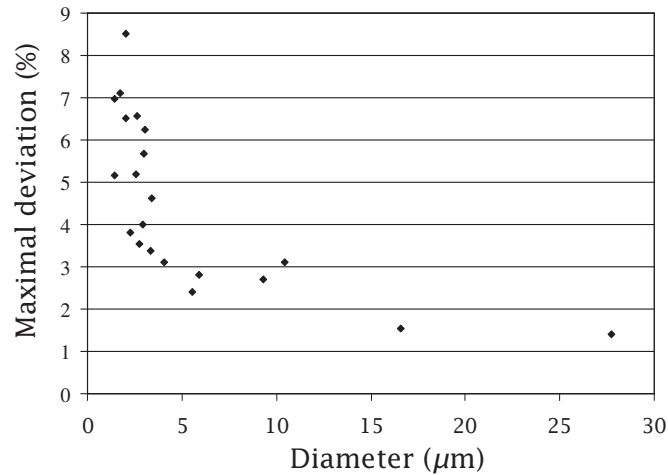


Figure 2.13: Maximal deviation in bubble measurement due to random error caused by the optical system and the segmentation process, as a function of mean bubble diameter measurement.

tion is demonstrated in Figure 2.15, in which three identical UCA bubbles expanded to different maximal diameters. Each frame corresponds to a $55 \times 45 \mu\text{m}^2$ area. Figure 2.15(a) was taken before ultrasound arrival. The maximal difference in excursion is $\Psi = 28\%$.

Figure 2.16 summarizes the results of 39 bubbles selected from ten events, recorded at an MI of 0.93. Figure 2.16 displays the relative bubble excursion as a function of the initial diameter. Identical markers indicate bubbles from the same sequence. In each first frame of the image sequences, bubbles of apparently the same size could be observed. Hence, for these bubbles, all conditions such as illumination, gain, and ultrasound field were kept unchanged, and the previously calculated random errors do not apply. We clearly notice that bubbles recorded from the same events (*e.g.*, those indicated by ‘*’) oscillate differently. All these bubbles had initial diameters approaching $2.6 \mu\text{m}$, whereas their maximal diameters range from $5.0 \mu\text{m}$ to $7.6 \mu\text{m}$, corresponding to relative expansions of 91% to 185% ($\Psi = 94\%$). Differences in oscillation or behavior of bubbles with similar initial sizes are also demonstrated in the optical images shown in Figure 2.17, which demonstrates bubble expansion and collapse at MI = 1.2. Each frame corresponds to a $88 \times 58 \mu\text{m}^2$ area. In the

RESULTS

[2, 4]

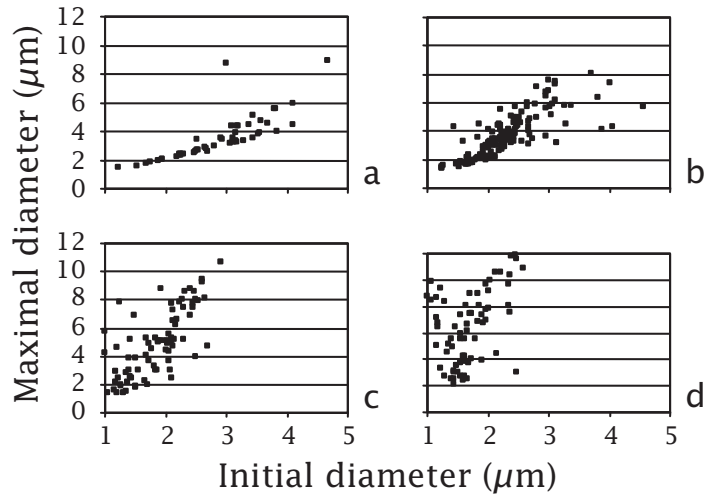


Figure 2.14: Bubble expansion at four different acoustic pressures. $MI = 0.089$ (a), $MI = 0.15$ (b), $MI = 0.25$ (c), $MI = 0.39$ (d).

first frame, taken before ultrasound arrival, no bubbles were visible. We presume that the bubbles were too small (*i.e.* below the optical resolution \mathcal{R}) to be detected. From Figure 2.17(b), (c), (d), and (e), the bubbles oscillate and appear to have similar sizes. Both bubbles expanded to $\varnothing 17.0 \mu\text{m}$ in Figure 2.17(d). In Figure 2.17(f), where the contraction phase of the ultrasonic wave starts, one bubble clearly collapsed while the other bubble continues contracting. In the last two frames, contraction is maximal, so both bubbles were no longer visible.

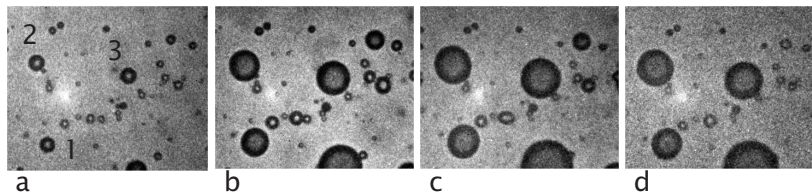


Figure 2.15: Optical image sequence of three microbubbles with apparently the same initial diameters, insonified at $MI = 0.93$. Each frame corresponds to a $55 \times 45 \mu\text{m}^2$ area. Frame (a) was taken before ultrasound arrival. The microbubbles expanded to different maximal diameters (b)-(d).

[2, 4]

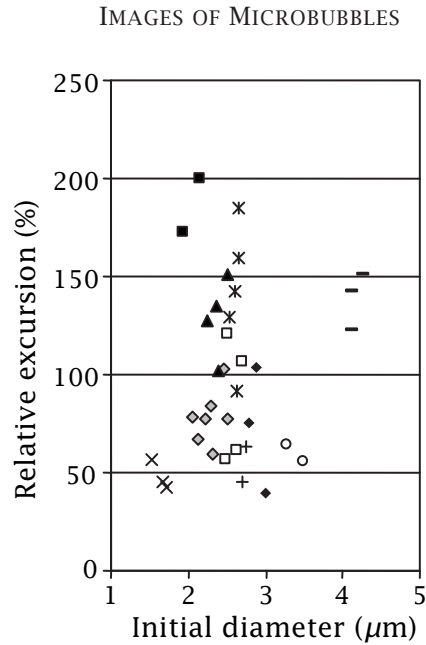


Figure 2.16: Relative excursion at $MI = 0.93$. 39 bubbles were selected from 10 image sequences. Identical markers indicate bubbles from the same image sequence.

At acoustic pressures corresponding to $MI > 0.5$, not only the phenomenon of bubbles violently collapsing [143], but also the phenomenon of bubbles coalescing was observed [141]. Figure 2.18 was recorded during insonification at $MI = 0.93$. In each $88 \times 58 \mu\text{m}^2$ frame, a $21 \times 22 \mu\text{m}^2$ region of interest is highlighted. In Figure 2.18(a) three sharp microbubbles can be discriminated, of which two seem to stick together. In Figure 2.18(b) there are only two separate expanding bubbles left. Figure 2.18(c) shows

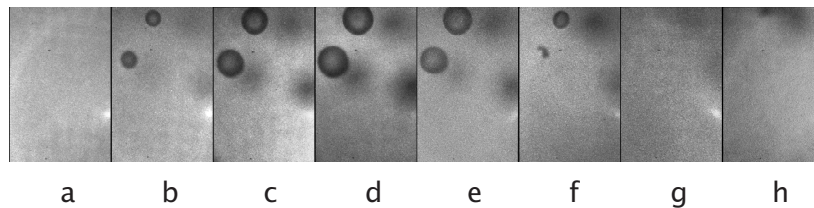


Figure 2.17: Bubble expansion (b)-(e) and collapse (f) within one acoustic cycle at $MI = 1.2$.

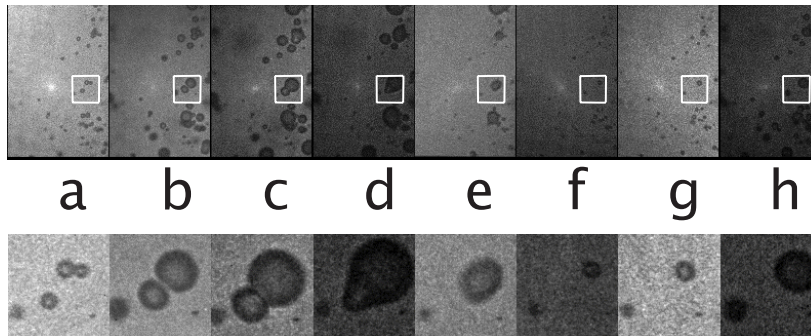


Figure 2.18: Bubbles coalescing during insonification at $MI = 0.93$.

these two bubbles attaching. In Figure 2.18(d) the lower left bubble appears to merge into the upper right bubble. The remaining bubble appears to have an oval shape in Figure 2.18(e), but a round shape in the remaining frames. Such asymmetric oscillations were regularly observed at high acoustic pressures.

Mean relative bubble excursion is plotted as a function of acoustic pressure in Figure 2.19, from 134 bubbles with diameters between $1.8 \mu\text{m}$ and $2.2 \mu\text{m}$. Standard deviations of the data were calculated for each acoustic pressure. The plotted theoretical curves were calculated numerically for a $\varnothing 2 \mu\text{m}$ bubble and based on the parameters of the constant thickness model [58]. The models used are based on a modified RPNNP equation, named after its developers Rayleigh, Plesset, Noltingk, Neppiras, and Poritsky [77], and a modified Herring equation [129]. We refer to these models as model A and model B, respectively. At acoustic pressures below 0.4 MPa, model B comes closest in describing the mean expansion, although there is clearly no fit. For higher acoustic pressures, model B predicts values much higher than the measured ones.

5 Discussion and conclusions

This was the first optical investigation of a large UCA data set using a 500 kHz transducer. The errors caused by our optical system and segmentation process are within 9% of the mean bubble sizes measured for median UCA bubble diameters larger than $1.4 \mu\text{m}$.

The initial diameters of the bubbles shown in Figure 2.14 are clearly not

[2, 5]

IMAGES OF MICROBUBBLES

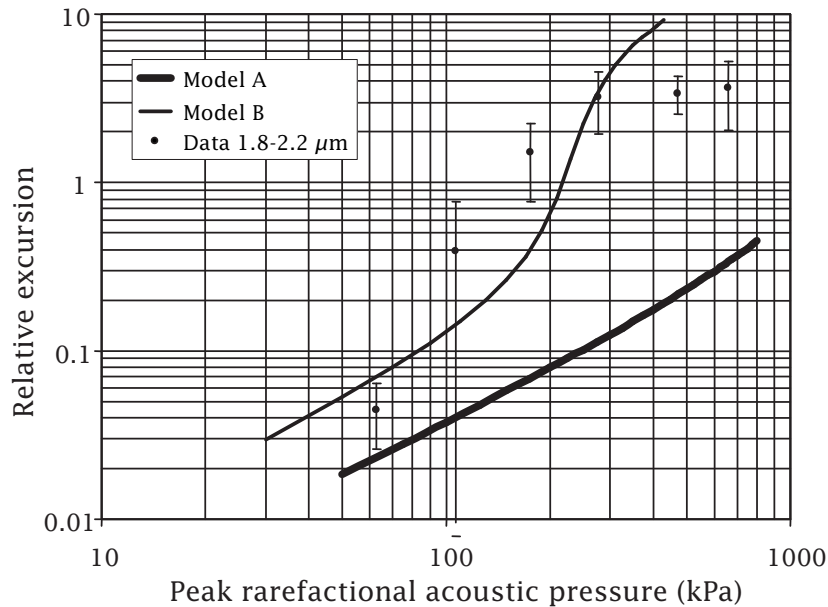


Figure 2.19: Mean relative excursion as a function of acoustic pressure applied, for bubble diameters ranging from $1.8\ \mu\text{m}$ to $2.2\ \mu\text{m}$, compared to model A and model B.

normally distributed. This is attributed to the lack of expansion of bubbles smaller than $2\ \mu\text{m}$ at lower pressures and to the rupturing and coalescing behavior of larger bubbles at higher pressures. Because only bubbles with measurable maxima were plotted, these two groups were excluded.

We checked the representativity of the bubbles analyzed for the whole agent by comparing the optically determined size distribution of our bubbles with published data of a SonoVue™ (Bracco Research SA, Geneva, Switzerland) distribution measured with a Coulter instrument [158]. The median diameter of $2\ \mu\text{m}$ is confirmed by these measurements, but bubbles over $4\ \mu\text{m}$ are hardly observed in the optical data. Only bubbles showing expansion were measured. We conclude that our optical observations are representative in the diameter range $1\ \mu\text{m}$ to $4\ \mu\text{m}$.

Because the image exposure times are low relative to the interframe times, the measured maxima do not have to correspond to the true maximal bubble expansions. In worst case, if the bubble expands according to

a sine, the maximal growth measured can be off the true value by half an interframing interval, which equals a twelfth of an expansion cycle, giving a measured excursion of $100\% \times \cos(2\pi/12) = 87\%$ of the true excursion.

Because the bubbles in the experiments shown in Figure 2.15 are closer to each other than 1% of the acoustic wavelength, acoustic differences due to location are negligible in this situation.

Although big bubbles that are out of optical focus might cause differences in bubble oscillating behavior, we did not take such effects into account.[‡]

From the above results, it is concluded that identical bubbles can have different oscillating behavior. The differences in the oscillation maxima observed might be explained by differences in elastic properties of individual bubbles.

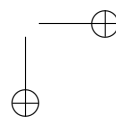
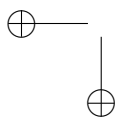
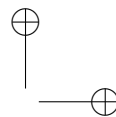
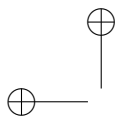
Acknowledgments

We thank Martijn Frijlink for designing the calibration grid and Leo Bekker for building part of the experimental setup.

[‡]A hidden bubble “2” generates a spatially varying far field pressure of [98]:

$$p(r_2) = \frac{\rho}{4\pi} \ddot{V}_2(t) \frac{1}{r_2},$$

where ρ is the fluid density, r_2 is the distance to the center of bubble 2, and \ddot{V}_2 is the second time derivative of the volume of bubble 2. For bubbles in our size range, just outside the depth of field ($\pm 5 \mu\text{m}$) the pressure may be of the order 50 kPa, which is less than 10% of the ultrasonic amplitude in our examples, and which cannot account for the large expansion differences in our optical observations.



3

Ultrasound-induced Microbubble Coalescence

Abstract

When gas bubbles collide, the following stages of bubble coalescence have been reported: flattening of the opposing bubble surfaces prior to contact, drainage of the interposed liquid film toward a critical minimal thickness, rupture of the liquid film, and formation of a single bubble. For ultrasound contrast agents this phenomenon has not yet been studied. During insonification, expanding contrast agent microbubbles may come into contact with each other, resulting in coalescence or bounce. In this study, we give a description of the coalescence mechanism of insonified microbubbles, based on high-speed photography and theoretical modeling. The optical images were recorded through a microscope at a frame rate of 3 million frames per second. Contrast agent microbubbles with monolayer

Based on the manuscript Postema M, Marmottant P, Lancée CT, Hilgenfeldt S, de Jong N. Ultrasound-induced microbubble coalescence. *Ultrasound Med Biol* 2004 submitted.

This work has been supported by the Technology Foundation STW (RKG.5104) and by the Interuniversity Cardiology Institute of the Netherlands.

[3, 1]

ULTRASOUND-INDUCED COALESCENCE

lipid shells were insonified at 0.5 MHz with acoustic amplitudes of 0.66–0.85 MPa.

The same stages of coalescence described for colliding bubbles could be distinctly observed with expanding contrast agent microbubbles. Flattening of the opposing bubble surfaces occurs if and only if the bubble system has a Weber number greater than 0.5. In our results, Weber numbers are relatively high because of the rapid bubble expansions, with a maximal radius increase at a rate of several m/s.

The film drainage was computed for immobile (rigid) bubble surfaces resulting in a laminar flow, and for mobile (free) bubbles surfaces resulting in a plug flow. The observed coalescence times appeared to be at least three times shorter than the times produced by laminar flow. In conclusion, we suspect that during expansion the lipid shell is so dilute that the contrast agent microbubble coalescence times are comparable to those of free gas bubbles.

1 Introduction

Ultrasound contrast agent (UCA) is a suspension of encapsulated gas bubbles. The bubbles have diameters ranging from 1 to 10 μm . They oscillate upon insonification, generating a characteristic acoustic response. UCAs are widely used in medical diagnostics [16, 57].

Observing ultrasound insonified UCA with a high-speed camera is a promising method for analyzing microbubble oscillation and destruction behavior [178, 79, 28, 96, 142]. Expanding UCA microbubble coalescence, observed with a high-speed camera during one cycle of ultrasound, has been previously reported by us [142].

To understand microbubble coalescence, one needs to comprehend the drainage of the liquid separating the bubble surfaces. Reynolds [153] noted that the viscosity of a liquid can be determined by pressing two flat plates together, squeezing the liquid out, and measuring the drainage velocity. Thus, he formulated an equation for the drainage velocity of a fluid between rigid surfaces. General theories on the coalescence of colliding bubbles and droplets that are based on liquid film drainage, were put forward by Marrucci [115], Dimitrov & Ivanov [42], Ivanov *et al.* [71], Lin & Slattery [105], Chesters & Hofman [21], Duineveld [43], and Klaseboer *et al.* [90]. Literature overviews on film drainage and bubble coalescence were given by Kralchevsky *et al.* [95], Narsimhan & Ruckenstein [130], and

Dhainaut [40].

Theories on droplet coalescence find applications in fuel ignition research and aerosol studies, whereas the research on bubble coalescence focuses on thin film physics and foam stability [95, 130]. This paper explores ultrasound-induced coalescence of microbubbles. Controlled coalescence will have potential applications in the clinical field.

Theories on bubble coalescence are generally based on the collision of unencapsulated bubbles or droplets, approaching each other at constant velocity. The following stages are discriminated in the process [40]. When two bubbles approach collision, the adjacent bubble surfaces will flatten, trapping liquid in between. The liquid drains, until the separation reaches a critical thickness that lies between 10 nm and 200 nm. An instability mechanism will cause the rupture of the separation and the formation of a coalesced bubble. We define bubble coalescence as the process of the fusing of two or more bubbles into a single bubble. The process begins with the flattening of the bubble surfaces and is considered finished when the resulting bubble has a spherical shape.

In this Chapter, we give a description of the coalescence of expanding microbubbles, based on optical observations and theoretical modeling. First, we present theories for expanding bubble coalescence, based on film drainage theory. Then, we present experimental results, obtained by recording optical images of insonified UCA. Finally, theories and results are compared and discussed.

2 Theory

During expansion, microbubbles may come into contact with bubbles nearby, resulting in coalescence or bounce. We discriminate the following stages in the coalescence mechanism, optically observed in Figure 3.1 and schematically represented in Figure 3.2. First, two bubbles approach collision while expanding (Figure 3.2a). Prior to contact, there may be a flattening of the adjacent bubble surfaces, trapping liquid in between (Figure 3.1a, Figure 3.2b). This trapped liquid drains (Figure 3.1b, Figure 3.2c) until the separation reaches a critical thickness (Figure 3.2d). An instability mechanism (Figure 3.2d, magnified) results in rupture of the separation (Figure 3.2e) and the formation of a merged bubble (Figure 3.1c). After coalescence the resulting bubble will have an ellipsoidal shape (Figure 3.1d, Figure 3.2f). Owing to surface tension, it will relax into a spherical shape.

[3, 2]

ULTRASOUND-INDUCED COALESCENCE

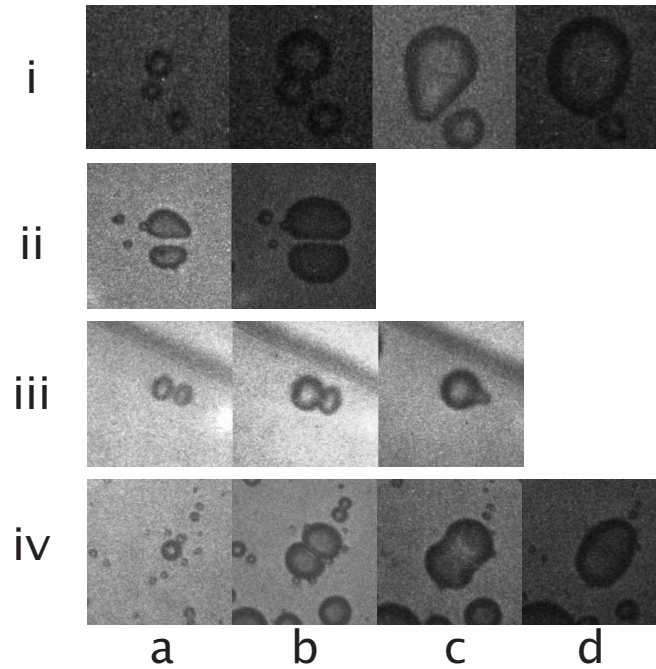


Figure 3.1: Optical images of stages of ultrasound-induced microbubble coalescence: flattening of contact surfaces (a), liquid film drainage (b), forming of a merged bubble (c), turning into an ellipsoidal bubble (d). Each frame in event (i) corresponds to a $21 \times 21 \mu\text{m}^2$ area. Each frame in events (ii)-(iv) corresponds to a $30 \times 30 \mu\text{m}^2$ area. Interframe times are $0.33 \mu\text{s}$.

When the contact time is less than the time needed for film drainage, the bubbles bounce off each other [18].

Flattening of the interface

Flattening of the opposing bubble surfaces occurs if and only if the bubble system has a Weber number $We > 0.5$ [21]. The Weber number for a fluid containing two bubbles with radii R_1 and R_2 , respectively, is given by the inertial force relative to the surface tension force:

$$We = \frac{\rho u^2}{\frac{\sigma}{R_m}}, \quad (3.1)$$

THEORY

[3, 2]

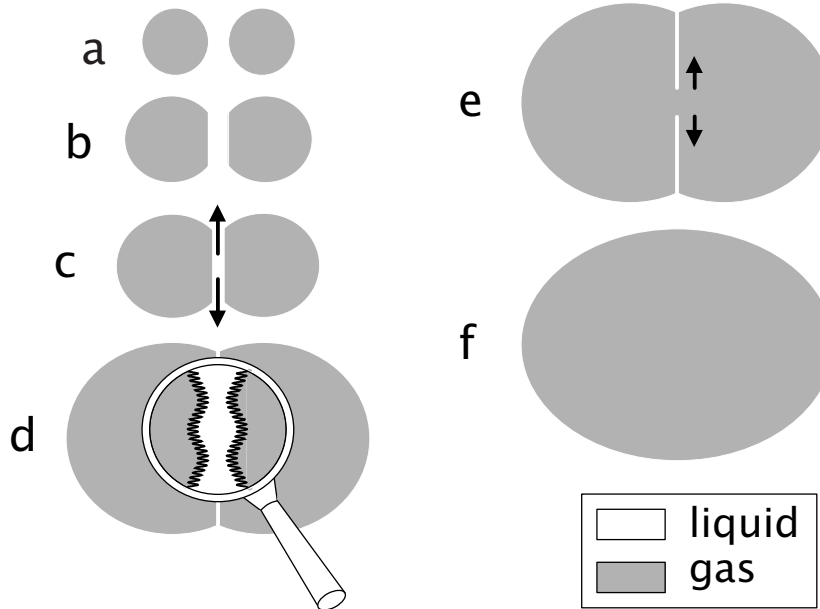


Figure 3.2: Schematic representation of stages of expanding bubble coalescence: bubble collision (a), flattening of contact surfaces (b), liquid film drainage (c) until a critical thickness (d), film rupture (e), and formation of an ellipsoidal bubble (f).

where u is the relative approach velocity of the bubble walls,* ρ is the fluid density, σ is the surface tension, and R_m is the mean bubble radius for which holds:

$$\frac{2}{R_m} = \frac{1}{R_1} + \frac{1}{R_2}. \quad (3.2)$$

In our results, Weber numbers are relatively high because of the rapid bubble expansions, with maximal radius increases of several m s^{-1} . If the Weber number is lower than 0.5, bubble coalescence will always occur, without flattening of the adjacent surfaces prior to contact [21]. In our observations, Weber numbers are up to 10. In the high-Weber number

*For bubbles with a constant center-to-center distance,

$$u = \dot{R}_1 + \dot{R}_2.$$

[3, 2]

ULTRASOUND-INDUCED COALESCENCE

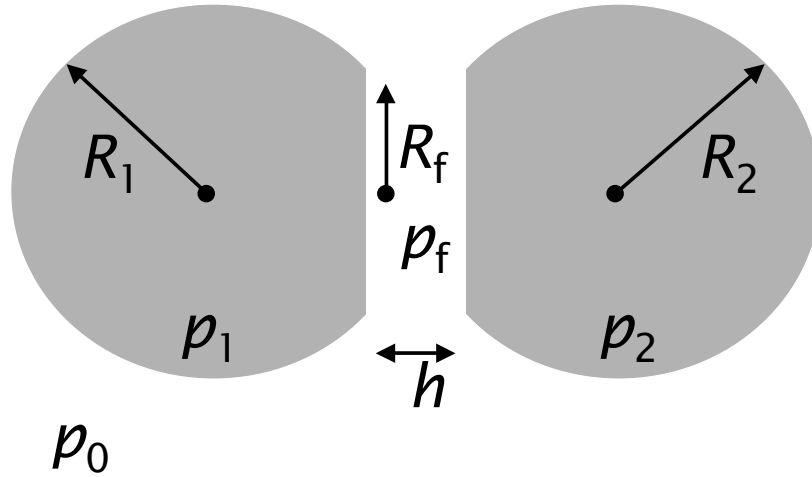


Figure 3.3: Schematic overview of variables used.

regimens, coalescence is determined by a second step, after flattening: film drainage.

Film drainage

We investigate microbubble coalescence by computing the film drainage for immobile (rigid) bubble surfaces resulting in a laminar flow, and for mobile (free) bubbles surfaces resulting in a plug flow.

Let us consider two bubbles with radii R_1 and R_2 , and internal pressures p_1 and p_2 , respectively, assumed spherical everywhere with the exception of a flattened interface that separates them through a liquid film of thickness h (*cf.* Figure 3.3). The drainage rate of the liquid film depends on the difference $(p + \Pi)$ between the film pressure p_f and the liquid ambient pressure p_0 . We estimate the pressure in the film by the mean of pressures p_1 and p_2 , since the parallel film surfaces lead to equal pressure differences towards both bubbles:

$$\begin{aligned}
 p + \Pi = p_f - p_0 &= \frac{1}{2} (p_1 + p_2) - p_0 = \\
 &= \sigma \left(\frac{1}{R_1} + \frac{1}{R_2} \right) \equiv p_{LY} \quad , \quad (3.3)
 \end{aligned}$$

where p_{LY} is the Laplace-Young film pressure [69], σ is the surface tension, and Π is the disjoining pressure that slows down film thinning in the range $0.1 \mu\text{m} > h > 0.01 \mu\text{m}$ until the film ruptures [115, 18, 5]. For the estimates we are going to make, we neglect Π , knowing that we will underestimate drainage times only for $h < 0.1 \mu\text{m}$. Therefore, we take p equal to the Laplace-Young pressure for the films observed. As such, the pressure gradient determining the drainage velocity is independent of the ambient pressure.

We choose a coordinate system such that the film is symmetric around the plane $z = 0$ and that its boundaries are located at $z = \pm \frac{h}{2}$. Then the radial velocity of the liquid in the film is a combination of a plug flow driven by the motion of the interfaces, and a laminar velocity profile (analogous to Poiseuille flow) driven by the radial pressure gradient [90, 197].

We will study two cases: the first for bubbles with immobile interfaces, and the second for bubbles with mobile interfaces.

Immobile interfaces

If the bubble surfaces consist of a high concentration of surfactant, on our working scales the interfaces are to be considered immobile [106, 105, 19]. In the case of immobile interfaces, the interfacial tangential velocity is zero, so the plug flow contribution is zero [90].

The film drainage velocity for rigid radial surfaces (disks) is given by the Reynolds equation [153]:

$$-\frac{dh}{dt} = \frac{2p h^3}{3\eta R_f^2}, \quad (3.4)$$

where η is the viscosity of the liquid, and R_f is the radius of the film surface.

The drainage time, τ_d , between the initial film thickness h_i and the critical film thickness h_c can be determined by integration of eq. (3.4):

$$\int_{h_i}^{h_c} -\frac{dh}{h^3} = \int_0^{\tau_d} \frac{2p}{3\eta R_f^2} dt. \quad (3.5)$$

By taking p and R_f constant over time, we obtain

$$\tau_d = \frac{3\eta R_f^2}{4p h_c^2} \left(1 - \frac{h_c^2}{h_i^2} \right). \quad (3.6)$$

[3, 3]

ULTRASOUND-INDUCED COALESCENCE

If $h_c^2 \ll h_i^2$ the drainage time can be approximated by

$$\tau_d \approx \frac{3 \eta R_f^2}{4 p h_c^2}. \quad (3.7)$$

Mobile interfaces

If the bubble surfaces consist of a low concentration of surfactant, which is less than (on the order of) 10^{-4} M, the interfaces are to be considered mobile [2]. In the case of mobile interfaces, the Poiseuille contribution to the drainage flow becomes negligible [90]. The film drainage velocity for free radial surfaces is given by the equation [42]:

$$-\frac{dh}{dt} = \frac{2 p h^3}{\eta R_f^2}. \quad (3.8)$$

Similarly to the immobile case, making the same assumptions with regards to p , R_f , and h_c , the drainage time can be approximated by

$$\tau_d \approx \frac{\eta R_f^2}{4 p h_c^2}. \quad (3.9)$$

Film rupture

Sharma & Ruckenstein described film instability as a combination of surface waves and thermal perturbations [161]. For thermal perturbations of a gas bubble in the micrometer range, the initial perturbation will be on the order of $\sqrt{\frac{kT}{\sigma}}$, where k is Boltzmann’s constant, and T is the absolute temperature, in our situation approximately 300 K. Hence, the initial thermal perturbation is lower than 1 nm.

Films gradually thin to a critical thickness at which it either ruptures due to a local instability or at which it converts to an equilibrium thickness. Aksoy measured these thicknesses for water, dependant of surfactant concentration [2]. For water films with a surfactant concentration below 10^{-4} M, critical film thicknesses are between 150 and 170 nm, whereas for surfactant concentrations above 10^{-3} M, critical thicknesses are between 20 and 70 nm.

3 Experimental setup

Our experimental setup for imaging insonified contrast bubbles is as previously described in [142] and Chapter 2. In short: a v389-SU 500 kHz single-element transducer (Panametrics Inc., Waltham, MA) was mounted into a water-filled container, spherically focused at the focal plane of the optical system. The optical images were recorded through a microscope with an Imacon 468 fast framing camera (DRS Hadland, Ltd., Tring, UK), capable of taking 8 frames per experiment. It operated at a frame rate of 3 million frames per second, corresponding to interframe times of $0.33 \mu\text{s}$. Exposure times ranged from 10 ns to 70 ns. The frames presented in this paper correspond to $30 \times 30 \mu\text{m}^2$ areas, except for Figure 3.1(i). The first frame was typically captured prior to arrival of the ultrasound wave at the focal area. Seven frames were taken during ultrasound insonification, spanning a full ultrasound cycle of $2 \mu\text{s}$. Contrast agent was insonified by 10 cycles of 0.5 MHz ultrasound with high acoustic amplitudes, in the range 0.66–0.85 MPa.

We investigated coalescence events of an experimental UCA (Bracco Research SA, Geneva, Switzerland). These bubbles are covered with a monolayer phospholipid shell and range in diameter from 1 to $6 \mu\text{m}$ with a median of $2 \mu\text{m}$. Undiluted UCA (5 ml of a 0.9% NaCl dilution, added to a 25 mg vial) was inserted through a cellulose capillary tube using either a syringe pressed by hand or a gravity fed or pumped infusion. This tube was positioned in the acoustic focus area. Since the capillary tube slightly moved within the acoustic focus area between experiments, the exact phase of the ultrasound wave in an image frame is not known. We performed 482 experiments at high acoustic amplitudes with the experimental UCA. We recorded 133 optical image sequences where microbubble coalescence was observed. Bubble sizes and distances were measured manually or by using a segmentation method described by Postema *et al.* [142].

4 Results

The observed phenomena are classified as follows: coalescence, bounce, multiple coalescence, and combined coalescence and fragmentation.

[3, 4] ULTRASOUND-INDUCED COALESCENCE

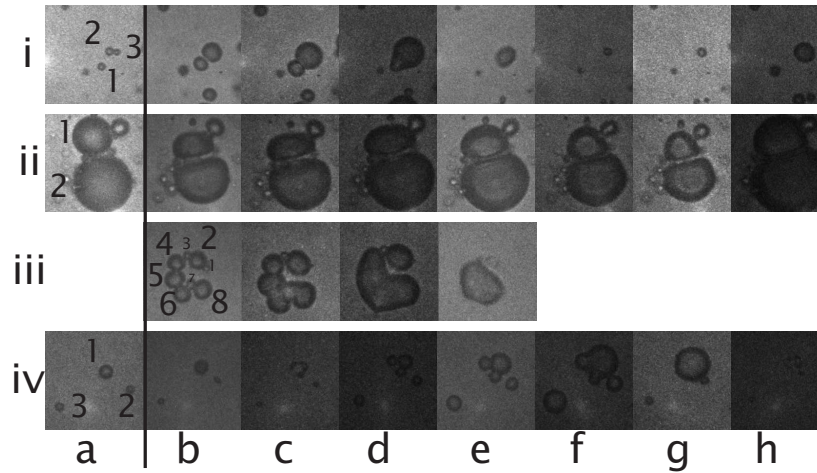


Figure 3.4: Optical images of microbubble coalescence and spherical rebound (i), bounce (ii), multiple coalescence (iii), and repeated coalescence (iv). Each frame corresponds to a $30 \times 30 \mu\text{m}^2$ area. The frames in column a have been captured prior to ultrasound arrival. Interframe times are $0.33 \mu\text{s}$.

Coalescence

Figure 3.4(i) shows an example of coalescence. Figure 3.4(i)a shows three microbubbles with diameters (1) $2.5 \mu\text{m}$, (2) $2.5 \mu\text{m}$, and (3) $2.0 \mu\text{m}$. After ultrasound arrival, microbubbles 2 and 3 have apparently coalesced (Figure 3.4(i)b). The remaining bubble, with a diameter of $5.0 \mu\text{m}$, is separated from microbubble 1, which is seen to have expanded to $3.8 \mu\text{m}$, with a center-to-center distance $d_0 = 4.8 \mu\text{m}$. The center of bubble 1 has shifted slightly to the upper right. The thickness of the liquid film, separating the bubble shells is approximately $h = 1.1 \mu\text{m}$, and the film radius is larger than $1.7 \mu\text{m}$. In Figure 3.4(i)c the liquid film appears to have drained while the bubbles expanded, but, a separation is still visible. This boundary appears to have disappeared in Figure 3.4(i)d,[†] leaving a pear-shaped bubble that turns ellipsoidal (Figure 3.4(i)e) when contracting. Figure 3.4(i)f,g,h shows that the coalesced bubble expands uniformly. It takes between $0.33 \mu\text{s}$ and $0.66 \mu\text{s}$ for the film in Figure 3.4(i)b to drain and rupture.

[†]If the line of sight is not perpendicular to the film, but at a tilt, the projection of the film boundaries might be obfuscated.

Bounce

Figure 3.4(ii) shows an example of bounce, *i.e.* bubbles approaching and flattening, but not coalescing. Figure 3.4(ii)a shows two microbubbles with diameters (1) $12.4\ \mu\text{m}$, and (2) $18.0\ \mu\text{m}$. After ultrasound arrival, the bubble surfaces have flattened (Figure 3.4(ii)b). The bubble centers have shifted towards each other. The film radius is on average $R_f = 4.8\ \mu\text{m}$. The film thickness is approximately $h = 1.8\ \mu\text{m}$. In the remaining frames the bubbles expand and contract, but coalescence does not occur.

Multiple coalescence

Figure 3.4(iii) shows an example of multiple coalescence. In Figure 3.4(iii)b an agglomerate of 8 touching microbubbles can be seen. Microbubbles 1 and 3 appear to be slightly above the focal plane [142]. As the bubbles expand, they coalesce into one heart-shaped bubble and one ellipsoidal bubble (Figure 3.4(iii)c,d). In the contraction phase, the heart-shaped bubble takes on an ellipsoidal shape (Figure 3.4(iii)e).

Combined coalescence and fragmentation

We observed repeated coalescence and fragmentation behavior in twelve events. Figure 3.4(iv) demonstrates the fragmentation, coalescence, and re-fragmentation of a microbubble. Figure 3.4(iv)a shows three microbubbles with diameters (1) $4.3\ \mu\text{m}$, (2) $2.6\ \mu\text{m}$, and (3) $2.8\ \mu\text{m}$. After ultrasound arrival, microbubbles 2 and 3 have translated towards microbubble 1 (Figure 3.4(iv)b). From Figure 3.4(iv)c, captured in contraction phase, it is appreciated that microbubble 1 has broken up into fragments. Three remaining fragments have started coalescing in Figure 3.4(iv)d, and have obtained an irregular shape in Figure 3.4(iv)e. The films separating the individual microbubbles have drained in Figure 3.4(iv)f, while microbubble 2 appears to touch the coalescing structure. In Figure 3.4(iv)g, the fragments of microbubble 1 have coalesced into one spherical bubble. Notice the translation of microbubble 2. Figure 3.4(iv)h shows that the coalesced bubble has re-fragmented in compression phase.

[3, 5]

ULTRASOUND-INDUCED COALESCENCE

5 Discussion

If we take $\eta = 0.001$ Pa s, $\sigma = 0.072$ N m⁻¹, $p = \sigma \left(\frac{1}{R_1} + \frac{1}{R_2} \right)$, $h_c = 0.15$ μ m [2], and substitute the parameters $R_1 = 6.2$ μ m, $R_2 = 9.0$ μ m, and $R_f = 4.8$ μ m obtained from Figure 3.4(ii), we find a film drainage time $\tau_d = 39$ μ s for immobile interfaces and $\tau_d = 13$ μ s for mobile interfaces. Within 1 μ s, the film can only drain to a minimum thickness $h_m = 0.94$ μ m. This is consistent with the absence of coalescence in Figure 3.4(ii).

If we substitute the parameters $R_1 = 1.9$ μ m, $R_2 = 2.5$ μ m, and $R_f = 1.7$ μ m obtained from Figure 3.4(i), we find a film drainage time $\tau_d = 1.4$ μ s for immobile interfaces and $\tau_d = 0.48$ μ s for mobile interfaces. Drainage theory of a thin film mobile interfaces is sufficient to account for the rapid coalescence in Figure 3.4(i), whereas drainage theory of a thin film with immobile interfaces is insufficient to account the observed coalescence.

The results presented in Figure 3.1 and Figure 3.4 show that the bubbles have expanded to more than ten-fold their initial surface areas before coalescing. As the UCA shell consists of a lipid monolayer, this layer is very dilute by the time of coalescence. Therefore, we may assume that the shell hardly influences the film instability mechanism, which confirms that the interfaces may be assumed mobile. We demonstrated previously with high-speed optical images that the UCA microbubbles used may expand to several times their original sizes, particularly at high acoustic pressures [142].

One of the effects of secondary radiation forces is that they lead to mutual attraction of similar-sized bubbles over multiple cycles. This may account for the translations observed in Figure 3.4.

The most unstable situations occur when a bubble is contracting and decelerating [139, 15]. Moreover, the forming of a re-entrant jet from a collapsing bubble has been related to the bubble shattering into fragments when the jet impacts the other side of the bubble surface. An optical image sequence of jet occurrence in a contrast microbubble was demonstrated by Postema *et al.* [143]. Apparently water was projected through the freely flowing microbubble. Although we clearly observed jets in two events, we did not observe fragmentation in the same events [141].

Irregular shapes of oscillating bubbles, like those shown in Figure 3.4(iii) and (iv), were interpreted as modes of shape instability of a single bubble before [25, 26, 121, 120], but may also be accounted for by coalescence of bubbles or bubble fragments.

After coalescence, the resulting bubble will have different acoustic prop-

CONCLUSIONS

[3, 6]

erties than the original bubbles, especially if it is comparable to the size resonant with the ultrasonic driving. If small UCA microbubbles, having passed through the narrowest vessels, coalesce, they may be controlled to obtain resonant sizes. Especially for subharmonic imaging [160], where twice the resonant bubble size is needed, and for tracking the diffusion of free gas bubbles with subharmonics, a promising technique in noninvasive blood pressure measurements [144], controlled microbubble coalescence may be applicable.

Owing to secondary radiation forces, clusters of bubbles may be formed. By inducing coalescence of such groups of bubbles, and thus creating emboli, the perfusion of tumor vascularization may be reduced.

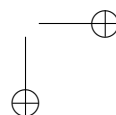
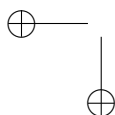
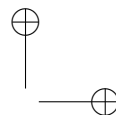
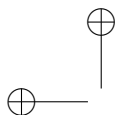
If coalescence of a lipid-shelled microbubble and a cell membrane can be induced, this will imply a promising technique in targeted drug delivery [189, 114].

6 Conclusions

Ultrasound-induced microbubble coalescence is the fusion of two or more microbubbles when subjected to an ultrasound field. Contrast agent microbubble coalescence has been observed frequently in an experimental setup. We showed that a coalescence mechanism for colliding bubbles also applies for expanding bubbles.

As adjacent bubbles expand, the following stages can be distinctly observed: flattening of the adjacent bubble surfaces prior to contact, drainage of the interposed liquid film toward a critical thickness, rupture of the liquid film, and formation of a single bubble. The time between flattening until coalescence was observed to take less than $1 \mu\text{s}$ for ultrasound contrast agent microbubbles in the micron diameter range.

Ultrasound-induced coalescence has potential clinical applications in harmonic imaging, noninvasive blood pressure measurements, and targeted drug delivery.



4

Ultrasound-induced Coalescence of Free Gas Microbubbles

Abstract

When gas bubbles collide, the following stages of bubble coalescence have been reported: flattening of the opposing bubble surfaces prior to contact, drainage of the interposed liquid film toward a critical minimal thickness, rupture of the liquid film, and formation of a single bubble. During insonification, expanding contrast agent microbubbles may collide with adjacent bubbles, resulting in coalescence or bounce. We previously investigated the coalescence times of insonified soft-shelled microbubbles, by comparing observed coalescence times to calculated film drainage times, based on the Reynolds equation.

In this study, we investigate the validity of the Reynolds-like equations for expanding free bubbles, by subjecting rigid-shelled contrast agent mi-

Based on the manuscript Postema M, Marmottant P, Lancée CT, Versluis M, Hilgenfeldt S, de Jong N. Ultrasound-induced coalescence of free gas microbubbles. *Proc IEEE Ultrason Symp 2004* to be submitted.

This work has been supported by the Technology Foundation STW (RKG.5104) and by the Interuniversity Cardiology Institute of the Netherlands.

[4, 1]

FREE MICROBUBBLE COALESCENCE

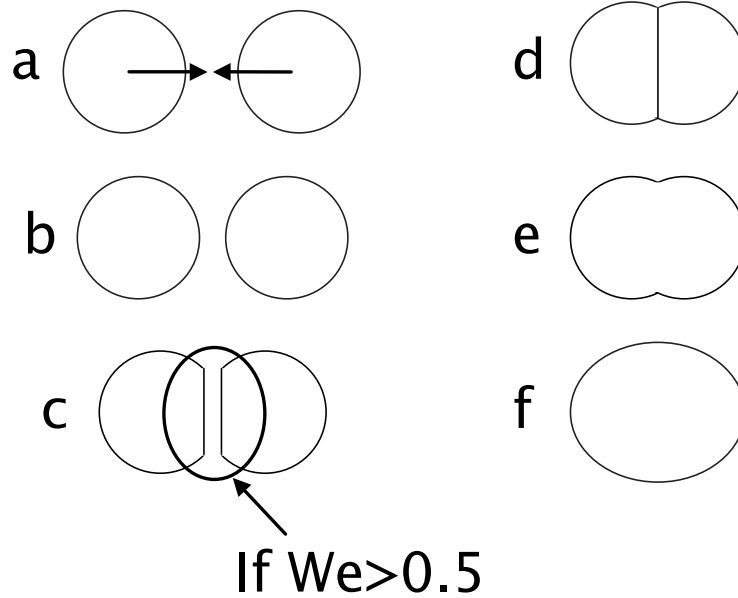


Figure 4.1: Schematic representation of colliding bubbles or droplets: approach (a-b), flattening of the interposed film (c), drainage to a critical thickness (d), film rupture (e), and formation of a single bubble (f).

crobbles to ultrasound, in order to release gas, and photograph the coalescence of these free gas bubbles. As with colliding bubbles, bubble surface flattening is related to the Weber number. Calculated drainage times are comparable with observed coalescence times of released gas bubbles.

1 Introduction

When two gas bubbles collide or are driven into each other, coalescence into a single bubble may result. The following stages of bubble coalescence have been identified (*cf.* Figure 4.1): flattening of the opposing bubble surfaces prior to contact, drainage of the interposed liquid film toward a critical minimal thickness, rupture of the liquid film, and formation of a single bubble. If the critical thickness is not reached during collision, the bubbles bounce off each other instead.

Free gas bubble coalescence after collision has been studied extensively [115, 42, 71, 105, 21, 43]. With ultrasound contrast agents, microbubble coalescence has been observed during ultrasound insonification, when expanding microbubbles come into contact with adjacent bubbles [141, 146]. With the aid of high-speed photography, we previously investigated the coalescence times of insonified soft-shelled microbubbles. We compared observed coalescence times to calculated film drainage times, based on the Reynolds equation [153]. We concluded that the bubbles behaved as if they had mobile interfaces like free gas bubbles [146]. However, to support this conclusion, we should investigate the validity of the Reynolds-like equations for expanding bubbles. In this study we do so, by subjecting rigid-shelled contrast agent microbubbles to ultrasound, in order to release gas, and investigate the coalescence of these free gas bubbles. We compare these times to the Reynolds-like computations.

2 Theory

Flattening of the opposing bubble surfaces occurs if and only if the bubble system has a Weber number $We > 0.5$ [21]. If $We < 0.5$, the bubbles will coalesce without the prior formation of an interposed film. The Weber number for a fluid containing two bubbles with radii R_1 and R_2 , respectively, is given by the inertial force relative to the surface tension force: $We = \rho u^2 / \frac{\sigma}{R_m}$, where u is the relative approach velocity, ρ is the fluid density, σ is the surface tension, and R_m is the mean bubble radius for which holds: $\frac{2}{R_m} = \frac{1}{R_1} + \frac{1}{R_2}$. Because the radius and with it the approach velocity of oscillating bubbles change during a cycle, so does the Weber number. If the bubble surfaces are considered to be mobile, the liquid film drainage time τ_d is approximated by [42]:

$$\tau_d \approx \frac{\eta R_f^2}{4 p h_c^2}, \quad (4.1)$$

where η is the viscosity of the fluid, R_f is the film radius, h_c is the critical film thickness, at which the film ruptures, p and is the pressure difference between film and surrounding fluid which is taken $p = \sigma \left(\frac{1}{R_1} + \frac{1}{R_2} \right)$. In our computations, we take $\eta = 0.001 \text{ Pa s}$, $\rho = 998 \text{ kg m}^{-3}$, $\sigma = 0.072 \text{ N m}^{-1}$, and $h_c = 0.15 \text{ }\mu\text{m}$ [2].

[4, 3]

FREE MICROBUBBLE COALESCENCE

3 Experimental methods

Our experimental setups for taking pictures of insonified contrast bubbles were as described in [22]. A $\varnothing 200 \mu\text{m}$ capillary tube, through which contrast agent was flowing, was fixed in the focal area of a v389-SU 500 kHz or a v397-SU 2.25 MHz single-element transducer (Panametrics Inc., Waltham, MA). The optical observations of the insonified ultrasound contrast agent were recorded with the Brandaris-128 system, operating at speeds up to 15 MHz.

The free gas bubbles were released from PB127 (POINT Biomedical Corporation, San Carlos, CA). PB127 consists of bilayered microspheres encapsulating nitrogen bubbles with a mean diameter of $4 \mu\text{m}$. The outermost layer is albumin and the inner layer is composed of a biodegradable polymer. The content of a PB127 vial was resuspended in 5 ml of deionized water, and shaken gently for 20 seconds before further dilution. Diluted PB127 was inserted through the capillary tube using a syringe pressed by hand. It was insonified by 6 or 8 cycles of 500 kHz, or by 8 cycles of 1.7 MHz ultrasound at acoustic pressures corresponding to mechanical indices between 0.3 and 1.9.

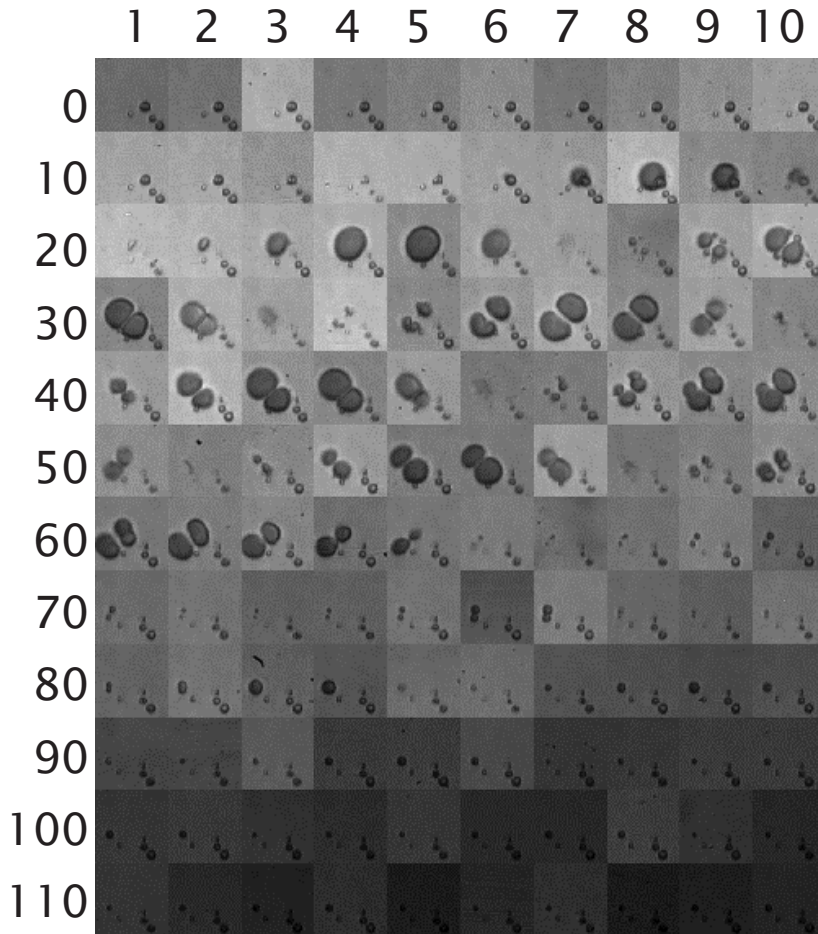


Figure 4.2: Gas release from PB127 microbubbles, captured at 10 MHz. Each frame corresponds to a $23 \times 23 \mu\text{m}^2$ area. Spontaneous coalescence of free gas microbubbles takes place in frames 81–83.

4 Results and discussion

The same stages of coalescence described for colliding bubbles could be distinctly observed with expanding free gas microbubbles and soft-shelled microbubbles. Examples of soft-shelled microbubble coalescence were shown in [141, 146, 142] and Chapter 3.

As with encapsulated bubbles, coalescence and bounce were regularly observed. For the interacting free gas microbubbles measured from the optical images, $We < 30$. We obtained 9 image sequences where free bubble coalescence times and the bubble dimensions could be measured. The times between flattening of the free bubble surfaces and coalescence are less than $0.3 \mu s$, for expanded gas bubbles with diameters between 3 and $5 \mu m$.

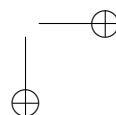
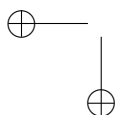
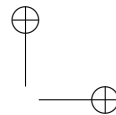
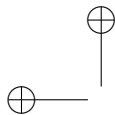
Figure 4.2 shows an example of gas release from a PB127 bubble. Each frame corresponds to a $23 \times 23 \mu m^2$ area. Four PB127 bubbles are in the field of view. After ultrasound arrival (frame 13) the bubbles contract. During expansion, gas escapes from the $\varnothing 3 \mu m$ upper bubble (16-19). The free gas is seen detached in frame 21. It expands (22-25) and starts to contract (26). Close to its minimum, the free gas bubble splits up into multiple fragments (27). During expansion, the fragments appear to have coalesced into two separate bubbles (28-29). These bubbles collide during expansion (30). The Weber number, calculated with the bubble wall displacement (29-30): $(u > \frac{2 \mu m}{0.1 \mu s})$, is greater than $We > 20 \gg 0.5$, which agrees with the flattening of the bubble surfaces. Computing equation (4.1) with $R_1 = 3.9 \mu m$, $R_2 = 3.4 \mu m$, and $R_f = 2.1 \mu m$ yields $\tau_d = 1.1 \mu s$. This long drainage time accounts for the observed bounce (30-32). Close to maximal contraction (33), the two bubbles fragment (34). During expansion, the fragments are seen to coalesce (35-37) into two bubbles of perpendicular orientation. Again, these bubbles bounce (38-39), fragment (40), and coalesce into two bubbles perpendicular to their mother bubbles (41). This process repeats itself, until insonification ends (66). The two remaining free gas bubbles still pulsate, and collide while doing so. These collisions may possibly be attributed to secondary radiation forces. In frame 82, the bubbles coalesce. This coalescence is induced by the pressure field exerted by the bubbles themselves. The remaining bubble has a maximum of $3.8 \mu m$. It pulsates at 1.7 MHz. Hence, the pulsations may be attributed to reflections.

5 Conclusions

Expanding gas bubble coalescence has been observed with released gas. As with colliding bubbles, bubble surface flattening is related to the Weber number. Calculated drainage times are comparable with the observed coalescence times of released gas bubbles.

Acknowledgments

We thank POINT Biomedical Corporation for supplying PB127.



5

Microbubble-based Pressure Measurements: Simulations

Abstract

This paper describes a noninvasive method to measure local hydrostatic pressures in fluid filled cavities. The method is based on the disappearance time of a gas bubble, as the disappearance time is related to the hydrostatic pressure. When a bubble shrinks, its response to ultrasound changes. From this response, the disappearance time, and with it the hydrostatic pressure, can be determined.

We investigated the applicability of the gases Ar, C₃F₈, Kr, N₂, Ne, and SF₆, based on their diffusive properties. For pressure measurements with a limited duration, *e.g.* 150 ms, Kr and Ar bubbles are most suitable, since they are most sensitive to pressure change. If there is also a limitation to bubble size, *e.g.* a maximum diameter of 6 μm, SF₆ is most suitable.

© 2004 Elsevier B.V. Reprinted with permission from Postema M, Bouakaz A, de Jong N. Noninvasive microbubble-based pressure measurements: a simulation study. *Ultrasonics* 2004 42(1-9):759-762.

This work has been supported by the Technology Foundation STW (RKG.5104) and by the Interuniversity Cardiology Institute of the Netherlands.

[5, 1]

PRESSURE MEASUREMENTS: SIMULATIONS

We present improvements of a method that correlates the duration of the decay of the fundamental ultrasound response to the hydrostatic overpressure. We propose to correlate the duration until subharmonic occurrence in combination with its decay, to hydrostatic overpressure, since the subharmonic decays more rapidly than the fundamental response. For a dissolving Ar gas bubble with an initial diameter of $14\ \mu\text{m}$, the overpressure can be determined 4 times as precise from the decay of the subharmonic response as from the decay of the fundamental response. Overpressures as small as 11 mmHg may be discriminated with this method.

1 Introduction

Local pressure measurements in cavities are widely used in medical diagnostics. Local pressure measurements in the heart are generally done by catheterization, causing pain and risk of infection [170]. We propose a renewed noninvasive method to measure pressure in cavities, based on the diffusion of free gas microbubbles and their interaction with ultrasound waves.

Epstein & Plesset [45] and De Jong *et al.* [84] demonstrated the relation between the disappearance time of gas bubbles and the hydrostatic pressure applied. Because the sizes of gas bubbles change as a function of the hydrostatic pressure, the acoustic properties of the bubbles are affected. Based on this finding, a relation between bubble disappearance time, its acoustic response, and ambient pressure can be established. Bouakaz *et al.* gave an overview of pressure measurement methods using this relation, and studied one *in vitro* [11]. Instead of free gas bubbles, they inserted ultrasound contrast agent in their setup. Hard-shelled ultrasound contrast agent can act as a vehicle to carry gas to a region of interest. Upon insonification at sufficient acoustic pressure, the gas is released. This process is called sonic cracking [141]. Bouakaz *et al.* determined overpressures from the decay of the fundamental acoustic response from diffusing released air bubbles. Pressure differences of 50 mmHg could be distinguished theoretically and experimentally. In medical diagnostics a resolution lower than 50 mmHg is desirable. To improve the sensitivity of the measurement approach mentioned above, we investigated the use of different gases. Furthermore, we investigated subharmonics as a marker for half resonant bubble size, since the subharmonic response is more sensitive to bubble size change than the fundamental [137].

Shi *et al.* had suggested the use of subharmonics for noninvasive pressure measurements [163]. They measured the scattering of encapsulated microbubbles over the pressure range 0–186 mmHg, and found a decrease of approximately 10 dB. It had previously been demonstrated theoretically that subharmonic generation from free gas bubbles and from ultrasound contrast agents requires a threshold insonifying pressure, which is minimal when microspheres are insonified at twice their resonance frequency [148, 160]. Palanchon *et al.* determined such thresholds with simulations and experiments for free microemboli [137].

Since subharmonics can be generated with the resonant bubble size corresponding to half the transmitted frequency, we propose to correlate the time until subharmonic occurrence, to the hydrostatic overpressure.

In this Chapter we present improvements of a previously published method that correlates the duration of the decay of the fundamental response to the hydrostatic overpressure [11]. To improve the method, we simulate the diffusive behavior of six gases, and suggest a qualitative measure for the applicability of a specific gas. We discuss the results with respect to boundary conditions and limitations, which hold for the ultimate *in vivo* situation. Furthermore, we simulate the scattering behavior of ultrasound-insonified diffusing gas bubbles. We investigate the sensitivity of the subharmonic response in comparison to the fundamental response.

2 Methods

Theoretical model

The change of gas bubble radius as a function of time, is given by [84, 11]:

$$\frac{dR}{dt} = DL \left(\frac{\frac{C_i}{C_0} - 1 - \frac{2\sigma}{R p_0} - \frac{p_{ov}}{p_0}}{1 + \frac{4\sigma}{3R p_0}} \right) \left(\frac{1}{R} + \frac{1}{\sqrt{\pi D t}} \right), \quad (5.1)$$

where $\frac{C_i}{C_0}$ is the ratio of the dissolved gas concentration to the saturation concentration (saturation ratio), D is the diffusion constant, L is the Ostwald coefficient, p_0 is the ambient pressure, p_{ov} is the applied overpressure, R is the instantaneous bubble radius, t is the time starting ($t = 0$) when the bubble surface is exposed to the liquid surface, and σ is the

[5, 3]

PRESSURE MEASUREMENTS: SIMULATIONS

surface tension. Eq. (5.1) shows that the disappearance of gas bubbles in a liquid medium is highly influenced by gas diffusion parameters and applied overpressure, and that the disappearance time of gas bubbles is shorter when the liquid medium is under pressure.

When a gas bubble dissolves into a liquid medium, its acoustic response changes with its radius. The oscillating behavior of a gas bubble in a liquid, subjected to a sound field with a low acoustic pressure, was derived by [129]. The changes in oscillating behavior of the dissolving gas bubble lead to changes in scattering cross sections [65], and thus, the scattering behavior of an insonified, diffusing gas bubble can be calculated, dependent of the applied overpressure.

Simulations

First, we investigate the diffusive behavior of six gases by simulations, and define a qualitative measure for the applicability of a specific gas. Then we explore the sensitivity of the subharmonic acoustic response from diffusing gas bubbles, in comparison to the fundamental response.

The disappearance of free gas bubbles was simulated at hydrostatic overpressures between 0 and 200 mmHg, with gases Ar, C₃F₈, Kr, N₂, Ne, and SF₆. For our computations we used MATLAB[®] (The MathWorks, Inc., Natick, MA) programs. The parameters used were published in [77]. The diffusion constants and the Ostwald coefficients were used for gas diffusing in water at room temperature [194, 89, 27, 104, 122]. Saturation ratios $\frac{C_i}{C_0} = 0$ were used, indicating that the gases are not present in water. From the diffusion curves, we computed the times it takes for bubbles to diffuse until they reach half their initial diameters. Half-size times were computed for gas bubbles varying in diameters from 5 to 20 μm , at ambient pressure, and at 20 mmHg overpressure. When applying an overpressure, the half-size time of a bubble is shorter than the half-size time at ambient pressure, $t_{1/2}$. This difference in half-size times, $\Delta t_{1/2}$, is a qualitative measure for the applicability of a specific gas for the measurement of hydrostatic overpressures: The sensitivity of the bubble to pressure change improves when $\Delta t_{1/2}$ increases.

Scattering cross-sections were calculated for the diffusing gas bubbles as a function of time [129, 65, 77], after filtering the fundamental and subharmonic responses from the acoustic bubble responses using a band-pass filter. The acoustic frequencies simulated, ranged from 0.5 MHz to 10 MHz.

Gas	Limitation					
	$t_{1/2} \leq 150 \text{ ms}$		$\mathcal{D} \leq 6 \mu\text{m}$		$t_{1/2} \leq 150 \text{ ms} \wedge \mathcal{D} \leq 6 \mu\text{m}$	
	\mathcal{D} (μm)	$\Delta t_{1/2}$ (ms)	$t_{1/2}$ (ms)	$\Delta t_{1/2}$ (ms)	\mathcal{D} (μm)	$\Delta t_{1/2}$ (ms)
Ar	12	3.1	35	0.6	6.0	0.6
C ₃ F ₈	1.0	0.8	> 1000	> 12	1.0	0.8
Kr	14	3.2	24	0.4	6.0	0.4
N ₂	7.5	2.8	99	1.6	6.0	1.6
Ne	8.5	2.7	72	1.2	6.0	1.2
SF ₆	3.5	1.7	453	7.2	3.5	1.7

Table 5.1: Half-size time differences for different limitations.

3 Results and discussion

From our simulations it follows that diffusion duration, and with it $\Delta t_{1/2}$, increases with the initial bubble diameter \mathcal{D} . However, bubble size is a limiting factor in the *in vivo* situation, as an encapsulated bubble may have to pass through narrow vessels before arriving in the cavity where the gas is released. The measurement duration is another limitation, especially for blood pressure measurements, since pressure changes occur within the cardiac cycle. A measurement of the systolic pressure in the left ventricle is limited to a duration of roughly 150 ms [6].

Table 5.1 gives an overview of values $\Delta t_{1/2}$, for different limitations. If the half-size time is limited to 150 ms, and there is no limit to the bubble size, Kr and Ar gas bubbles result in the highest $\Delta t_{1/2}$. If the bubble diameter is limited to $6 \mu\text{m}$, and there is no limit to the measurement duration, C₃F₈ and SF₆ bubbles result in the highest $\Delta t_{1/2}$. If both limitations are combined, SF₆ and N₂ bubbles result in the highest $\Delta t_{1/2}$. Hence, the applicability of a specific gas is mainly determined by the limitations that apply.

Shi *et al.* noted, that yet another limitation of our approach may lie in the fact that the disappearance times of the gas bubbles depend also on the gas content of the blood [163]. We may overcome this limitation by choosing gases that are not present in the human body, and as such have a saturation ratio $\frac{C_1}{C_0} = 0$.

Figure 5.1 shows the fundamental and subharmonic scattered power of

[5, 4]

PRESSURE MEASUREMENTS: SIMULATIONS

a dissolving $\varnothing 14 \mu\text{m}$ Ar bubble, insonified at 1 and 2 MHz, respectively, as a function of time. The solid lines represent the situation at ambient pressure, the dashed at a 50 mmHg hydrostatic overpressure. The maximum of the fundamental is reached gradually, whereas the subharmonic has a rapid rise near double-resonant size. The subharmonic peaks decay with 40 dB in 8.2 ms, whereas the most rapid fundamental decay is only 20 dB in 15.2 ms. Hence, the subharmonic response is more sensitive to diameter change than the fundamental response, indeed. Since overpressures of 50 mmHg could be distinguished from the decay of the fundamental response [11], we estimate that the scattering may have a ± 5 dB variation. With this variation, we computed diffusion time differences Δt_d for the decays observed in Figure 5.1: $\Delta t_d = 7.6$ ms for the fundamental response, and $\Delta t_d = 2.0$ ms for the subharmonic response. In our simulations, these diffusion time differences correspond to hydrostatic overpressures of 45 and 11 mmHg, respectively. Hence, the overpressure can be determined 4 times as precisely from the decay of the subharmonic response as from the decay of the fundamental response.

As an improvement of noninvasive pressure measurements, we propose to correlate the duration until the subharmonic peak in combination with the subharmonic decay, to hydrostatic overpressure. Evidently, precise knowledge of the initial bubble size is of importance. This might be established by generating subharmonics around the initial bubble size too.

Controlled gas release from a single bubble is currently under investigation *in vitro* with an ultrafast framing camera system [23].

4 Conclusions

For pressure measurements with a limited duration, *e.g.* 150 ms, Kr and Ar bubbles are most suitable, since they are most sensitive to pressure change. If there is also a limitation to bubble size, *e.g.* a maximum diameter of $6 \mu\text{m}$, SF_6 is most suitable.

When a diffusing gas bubble with known initial diameter is insonified, the duration until subharmonic occurrence in combination with its decay, is an indicator of the hydrostatic overpressure. The subharmonic decays more rapidly than the fundamental response. For a diffusing Ar gas bubble with an initial diameter of $14 \mu\text{m}$, the overpressure can be determined 4 times as precisely from the decay of the subharmonic response as from the decay of the fundamental response. Overpressures as small

CONCLUSIONS

[5, 4]

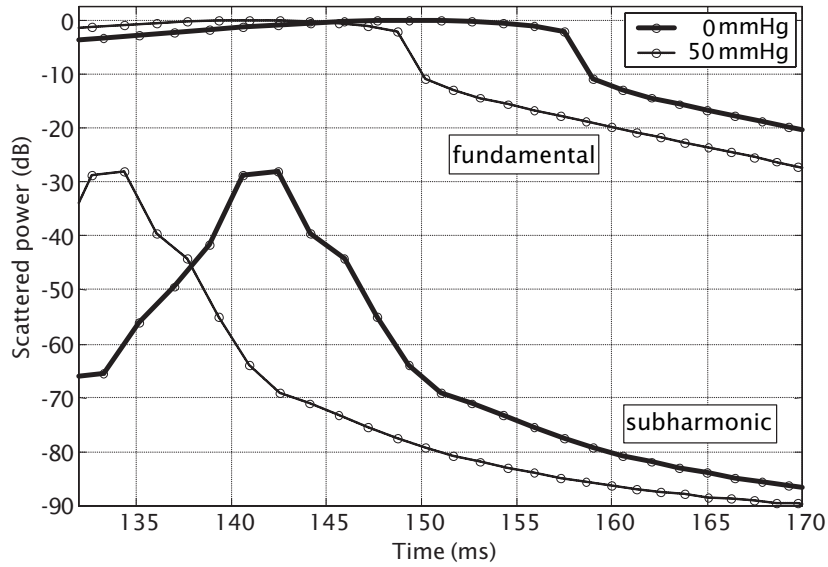
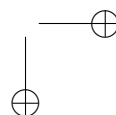
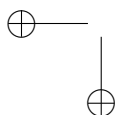
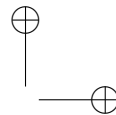
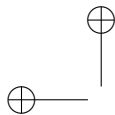


Figure 5.1: Fundamental and subharmonic scattering cross-sections of a diffusing $\varnothing 14 \mu\text{m}$ Ar bubble, insonified at 1 and 2 MHz, respectively, as a function of time, when applying hydrostatic overpressures of 0 and 50 mmHg.

as 11 mmHg may be discriminated with this method. Generating subharmonics may also be useful for verifying the initial bubble size.

Free gas bubbles can be delivered to cavities, and released by means of sonic cracking, which is currently under investigation.



6

Ultrasound-induced Gas Release from Rigid-Shelled Microbubbles

Abstract

We investigated gas release from two rigid-shelled ultrasound contrast agents, by subjecting them to high-MI ultrasound and simultaneously capturing high-speed photographs. At an insonifying frequency of 1.7 MHz, a larger percentage of contrast bubbles is seen to crack than at 0.5 MHz. Most of the released gas bubbles have equilibrium diameters between 1.25 and 1.75 μm . Their disappearance was observed optically. Free gas bubbles have equilibrium diameters smaller than the bubbles from which they have been released.

Based on the manuscript Postema M, Bouakaz A, Versluis M, de Jong N. Ultrasound-induced gas release from contrast agent microbubbles. **2004** submitted.

This work has been supported by the Technology Foundation STW (RKG.5104) and by the Interuniversity Cardiology Institute of the Netherlands.

[6, 1]

ULTRASOUND-INDUCED GAS RELEASE

1 Introduction

Bubbles have been under investigation for medical imaging and drug delivery, but may also be of interest for noninvasive pressure measurements.

Bubbles have been under investigation for medical imaging and drug delivery, but may also be of interest for noninvasive pressure measurements.

The assessment of local blood pressure plays an important role in contemporary cardiology. Local cardiac pressure measurements are generally done by catheterization. This is an expensive procedure with a risk of infection [170].

Since the 1970s, several noninvasive methods have been proposed for local blood pressure assessment, based on the acoustic properties of microbubbles under different hydrostatic pressure conditions.

The resonance frequency f_r of a free gas bubble is related to its diameter \mathcal{D} according to [181]:

$$f_r \approx \frac{6.5 \text{ m s}^{-1}}{\mathcal{D}}. \quad (6.1)$$

When subjected to a hydrostatic overpressure, a bubble will contract, and by that increase its resonance frequency. In [46, 181, 157] it was suggested to measure pressures from changes in resonance frequency of relatively big, and thus slowly dissolving, gas bubbles.

The dissolving time of gas bubbles is related to the hydrostatic pressure as well [11]. Hence, another noninvasive method for blood pressure assessment would be the measurement of the acoustic response from a dissolving bubble population. Simulations of the dissolving behavior of gas bubbles have been presented in [86, 11, 20, 144]. The precision of the pressure measurement might be increased by making use of the (sub)harmonic components of the acoustic signals [164, 144].

For both noninvasive methods, free gas bubbles have to be delivered to a region of interest. Hard-shelled ultrasound contrast bubbles might act as the vehicles to deliver the gas. Upon insonification, the gas would then be released from their encapsulation and immediately be subjected to the local hydrostatic overpressure. The ultrasound-induced release of gas from an encapsulated microbubble is referred to as ‘sonic cracking’ [178]. Previous experiments demonstrated the feasibility of gas release from contrast agent microbubbles and the subsequent fading acoustic response from the dissolving released gas bubbles [176, 85, 11, 20].

EXPERIMENTAL SETUP

[6, 2]

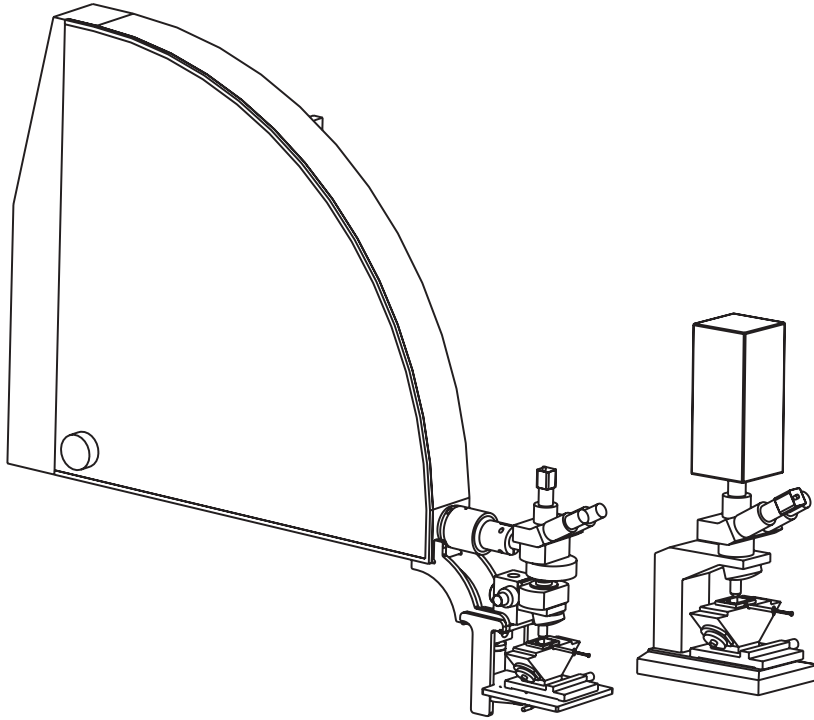


Figure 6.1: Line drawings of the housing of the Brandaris-128 (left) and the CR 2000 camera (right).

In this study, we visualize the release and the dissolution of air bubbles after sonic cracking. Furthermore, we discuss if the sizes of the released gas bubbles are in agreement with previous measurements of acoustic decay times.

2 Experimental setup

Overview

For the observations of gas release, we made use of the Brandaris-128 fast framing camera system [22]. The amplitude of the electrical signal

[6, 2]

ULTRASOUND-INDUCED GAS RELEASE

generated by an AWG 520 arbitrary waveform generator (Tektronix, Inc., Beaverton, OR) was adjusted by two variable 355C/D attenuators (Hewlett Packard Company, Palo Alto, CA) in series, and an A-500 60 dB linear power amplifier (ENI technology, Inc., Rochester, NY). The signal was converted to ultrasound by a v389-SU 500 kHz, or by a v397-SU 2.25 MHz single-element transducer (Panametrics Inc., Waltham, MA), both spherically focused at 7.5 cm. The transducer was mounted in a Perspex container at an angle of 45° relative to the top of the container. This container was filled with saturated water. A \varnothing 200 μm cellulose Cuprophan[®] capillary tube (Membrana GmbH, Wuppertal, Germany) was fixed in the focal area of the transducer, through which contrast agent was flowing.

Optics

Underneath the capillary tube an optic fiber was mounted. This fiber was connected to an MVS-7010 Fiber Optic Strobe (PerkinElmer Optoelectronics, Salem, MA), and to a KLS-201 continuous fiber light source (Olympus KMI (KeyMed Ltd), Southend-on-Sea, UK).

The container was positioned beneath a customized BXF_M microscopic system (Olympus Optical Co., Ltd., Tokyo, Japan) with a U-CA magnification changer (Olympus Optical Co., Ltd.), switched to 2 \times magnification and a LUMPlanFI 60 \times water immersion objective lens (Olympus Optical Co., Ltd.). For image control purposes, an LCL-902K CCD camera (Watec Co., Ltd., Yamagata, Japan) was mounted to the top of the microscope.

Camera

The optical observations were recorded with a Brandaris-128 (*cf.* Figure 6.1) fast framing camera system [22]. The Brandaris-128 captured sequences of 128 image frames at speeds up to 15 million frames per second. Typical frame sizes correspond to 89 \times 68 μm^2 . In all observations, image frames were captured before, during, and after ultrasound insonification.

For the observations of gas dissolution, which is a relatively slow process compared to bubble oscillations, we made use of a data set recorded with a CR 2000 camera (Redlake MASD, LLC, San Diego, CA) that operated at a speed of two thousand frames per second. This camera had been installed on top of the microscope, as shown in Figure 6.1.

Contrast agents

We investigated the ultrasound contrast agent Quantison™ (Upperton Limited). It consists of human serum albumin-encapsulated air bubbles with a mean diameter of $3.2\ \mu\text{m}$. Shell thicknesses are between 0.2 and $0.3\ \mu\text{m}$ [54]. The resonance frequency of the bulk agent is $4\ \text{MHz}$ [54]. The content of a Quantison™ vial was resuspended in $5\ \text{ml}$ of Isoton® II (Beckman Coulter, Inc., Fullerton, CA), and shaken gently for 20 seconds before further dilution.

We also investigated PB127 (POINT Biomedical Corporation, San Carlos, CA), which is specified as follows: PB127 consists of bilayered microspheres encapsulating nitrogen bubbles with a mean diameter of $4\ \mu\text{m}$. The outermost layer is albumin and the inner layer is composed of a biodegradable polymer. The resonance frequency of PB127 lies between 6 and $7\ \text{MHz}$. The content of a PB127 vial was resuspended in $2\ \text{ml}$ of deionized water, and shaken gently for 20 seconds before further dilution.

Ultrasound

The agents were insonified either by 6 or 8 cycles of $500\ \text{kHz}$ ultrasound, or by 8 cycles of $1.7\ \text{MHz}$ ultrasound. For both frequencies transmitted, peak acoustic pressures corresponded to mechanical indices in the range $0.3 < MI < 1.9$. We refer to ultrasound transmission with mechanical indices greater than 0.8 as high-MI insonification. Acoustic pressures in this regimen are high enough to ensure gas release [17].

Acoustic pressures applied were measured with a calibrated MH28-10 hydrophone (FORCE Technology, Brøndby, Denmark) in a separate water tank (*cf.* Chapter 2).

Procedure

We recorded 533 image sequences with the Brandaris-128 system, and 55 sequences with the CR 2000 camera. For each event, the total number of contrast agent microbubbles visible in the frames were counted, and the number of contrast agent microbubbles from which gas was released. From the frames recorded after ultrasound insonification, the diameters of the released gas bubbles (if still present) or fragments thereof were measured, as well as the diameters of the contrast agent microbubbles from which they had escaped. Bubble diameters and distances were measured

[6, 3] ULTRASOUND-INDUCED GAS RELEASE

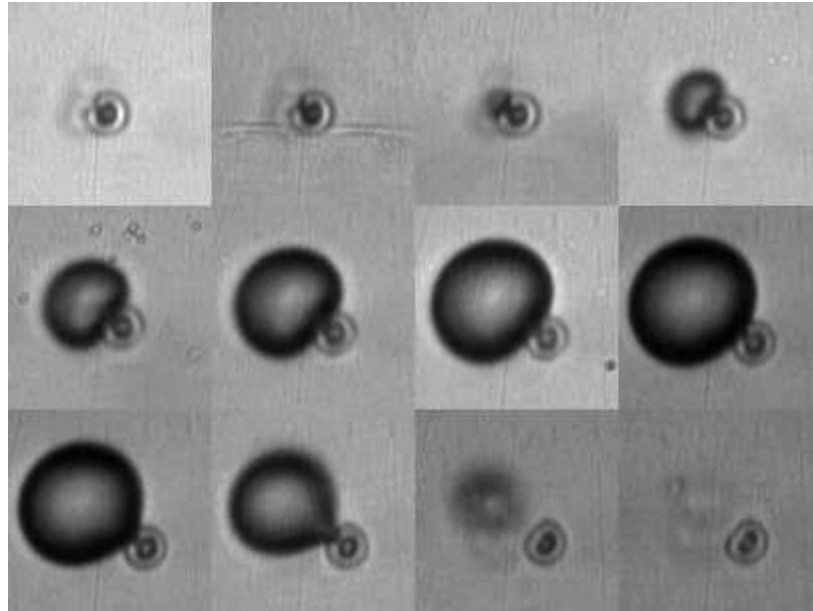


Figure 6.2: Gas release from a Quantison™ contrast microbubble at 0.5 MHz and $MI = 1.1$. Each frame corresponds to a $19 \times 19 \mu\text{m}^2$ area. Interframe times are $0.1 \mu\text{s}$.

manually or by using an image processing method described in [142] and Chapter 2.

3 Results

Quantison™

An example of the sonic cracking of a Quantison™ bubble is shown in Figure 6.2. Frames numbering is from left to right, then from upper to lower. The camera system operated at a speed of 10 million frames per second. Gas is seen to escape from a $\varnothing 4.3 \mu\text{m}$ shelled Quantison™ bubble in the third frame. Apparently, the Quantison™ shell is too rigid to be seen expanded. The free gas expands to $\varnothing 12.3 \mu\text{m}$ in the eighth frame, after which it contracts. In the eleventh frame, the free gas bubble, which

RESULTS

[6, 3]

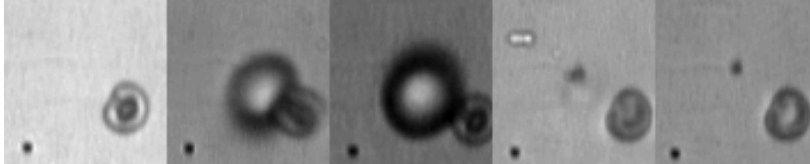


Figure 6.3: Gas release from a Quantison™ contrast microbubble at 0.5 MHz and $MI = 0.9$. Each frame corresponds to a $13 \times 13 \mu\text{m}^2$ area. Interframe times are $0.33 \mu\text{s}$.

has been subjected to motion blur, appears to be detached from the encapsulated bubble. In the twelfth frame, the gas is hardly visible.

Another example of gas release is given in Figure 6.3. The camera system operated at a speed of 3 million frames per second. In the second frame, gas escapes from a $\varnothing 3.7 \mu\text{m}$ bubble. The response of the released gas to ultrasound can be clearly appreciated. After expanding to a $\varnothing 8.0 \mu\text{m}$ maximum in frame three, it is seen detached and contracted in frames four and five. The encapsulated bubble clearly looks different than before cracking, as if there is no gas left inside the shell. A few microseconds after insonification, the left frame of Figure 6.4 was captured. The released gas bubble is visible to the upper left of the bubble from which we

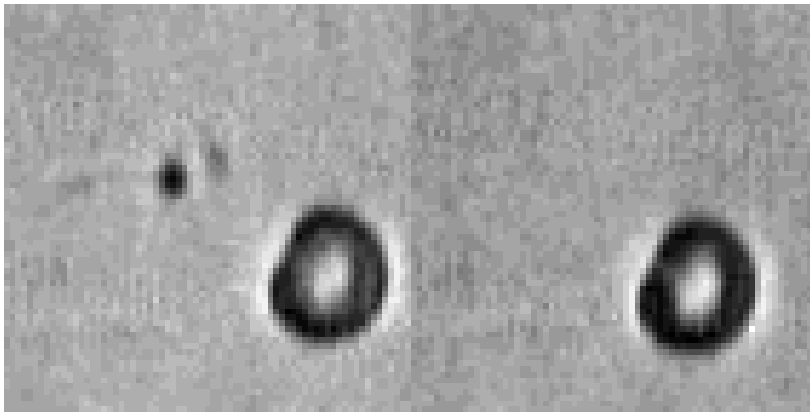


Figure 6.4: Dissolution of released gas. Each frame corresponds to a $13 \times 13 \mu\text{m}^2$ area. Time between recordings is 100 ms. The free gas bubble is visible to the upper left of the PB127 bubble in the left frame.

[6, 3] ULTRASOUND-INDUCED GAS RELEASE

saw it escape. Its diameter is estimated to be less than $1\ \mu\text{m}$. One hundred ms later, the right frame was captured. Here, the released gas bubble has disappeared.

The dissolving process itself of the released gas bubbles was captured at 2000 frames per second. The upper images of Figure 6.5 show 8-bit photographs of three QuantisonTM bubbles before ultrasound arrival. The lower images show the same photographs after gray-level window-slicing. After insonification, the QuantisonTM bubbles have translated, and two fragments are visible in the second frame. The diameters of the fragments are less than $1\ \mu\text{m}$. These fragments slowly disappear, and are hardly visible in the last frame.

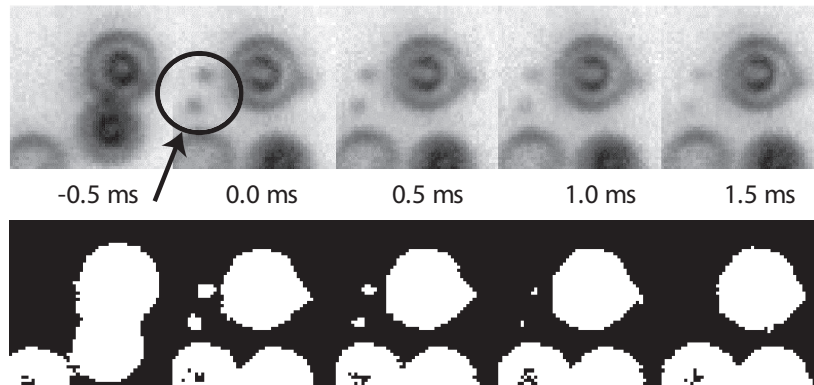


Figure 6.5: Dissolution of released gas, captured at 2 kHz. Upper frames show raw CCD images, lower frames show segmented images. Each frame corresponds to a $10 \times 10\ \mu\text{m}^2$ area. The released gas fragments (arrow) are less than $1\ \mu\text{m}$.

RESULTS

[6, 3]

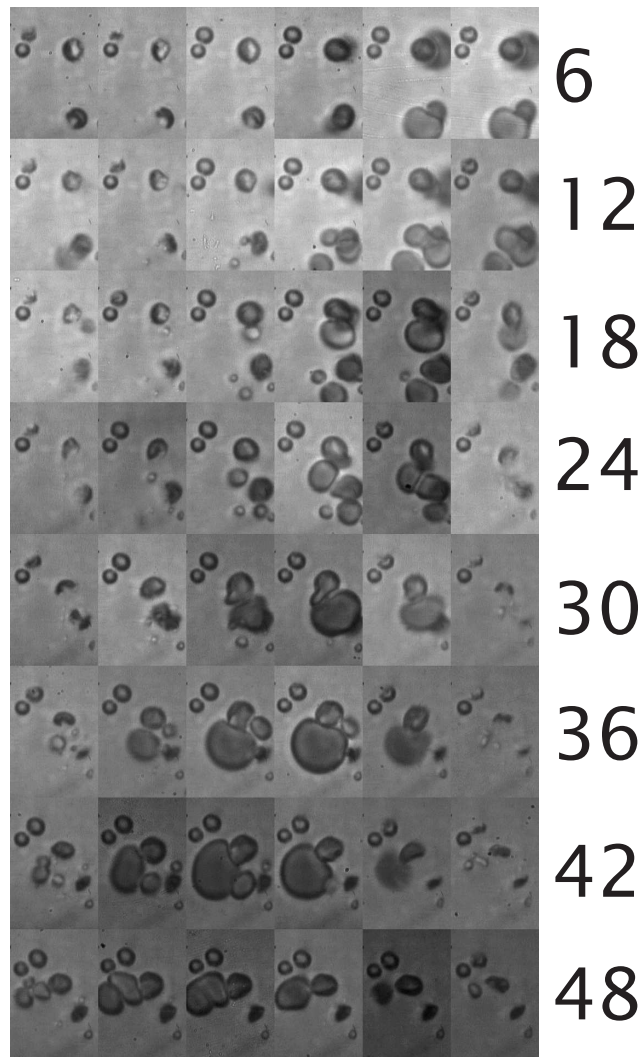


Figure 6.6: Gas release from a PB127 contrast microbubble at 1.7 MHz and $MI = 0.9$. Each frame corresponds to a $46 \times 30 \mu\text{m}^2$ area. Interframe times are $0.1 \mu\text{s}$. After release (first three rows), the free gas bubbles interact, until one free gas bubble remains (last row).

[6, 3] ULTRASOUND-INDUCED GAS RELEASE

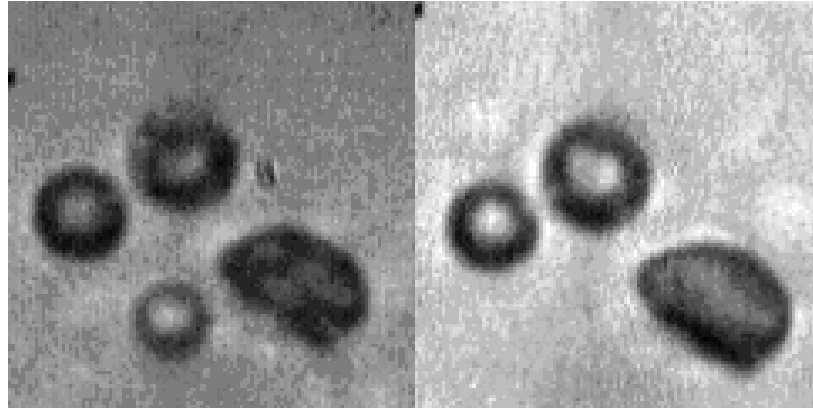


Figure 6.7: Three PB127 bubbles and one released gas bubble (left). After 100 ms the released gas bubble has disappeared (right). Each frame corresponds to a $23 \times 23 \mu\text{m}^2$ area. Time between recordings is 100 ms.

PB127

An example of the sonic cracking of a PB127 bubble is shown in Figure 6.6. Frames numbering is from left to right, then from upper to lower. The camera system operated at a speed of 9.4 million frames per second. Upon ultrasound arrival in the second frame, the bubbles start to contract. From frame four on, gas is released from two $\varnothing 7 \mu\text{m}$ PB127 bubbles. In frame eight, both gas bubbles have been detached from the shell. Starting with frame ten, gas release is again observed from the lower PB127 bubble. The released gas bubbles interact, and both fragmentation and coalescence occur several times between frames 21 and 47. After insonification had finished, one resulting free gas bubble remained, which was still seen to pulsate. The left frame of Figure 6.7 was captured after insonification. The free gas bubble is the lower bubble in the diamond-shaped bubble group. Its resting diameter is $4 \mu\text{m}$. One hundred ms later, the right frame was captured. Here, the free gas bubble has disappeared.

Our results show that the sizes of the PB127 bubbles from which gas was released, are normally distributed. The mean diameter of these bubbles is $3.6 \mu\text{m}$, with a standard deviation of $1.5 \mu\text{m}$.

The size distribution of the released gas bubbles from PB127 is shown in Figure 6.8. For both frequencies, most released gas bubbles have equi-

RESULTS

[6, 3]

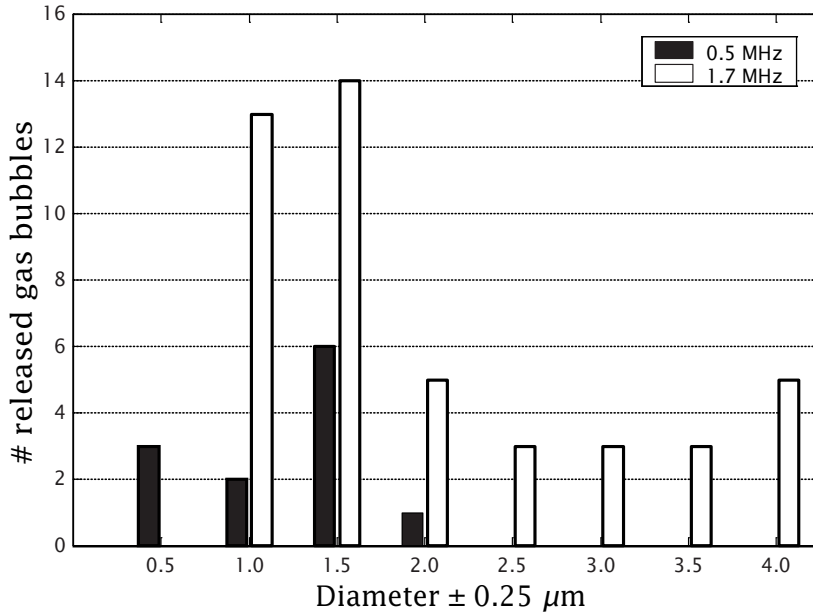


Figure 6.8: Size distribution of released gas from PB127.

librium diameters between 1.25 and 1.75 μm.

The size distribution of the released gas bubbles from PB127 is shown in Figure 6.8. For both frequencies, most released gas bubbles have final resting diameters between 1.25 and 1.75 μm.

Overview

A quantitative overview of gas release is demonstrated in Figure 6.9. Typically, 10–15 contrast agent bubbles were visible in the field of view. For both agents, the percentage of released gas bubbles is greater at 1.7 MHz than at 0.5 MHz insonification.

Released gas bubbles have been observed to translate, to fragment, and to coalesce with other released bubbles. The contrast agent bubbles did not demonstrate these phenomena. Our measurements of resting sizes of released gas bubbles include fragments of released gas bubbles and coalesced bubbles. Bubbles that did not show gas release upon insonification,

[6, 4] ULTRASOUND-INDUCED GAS RELEASE

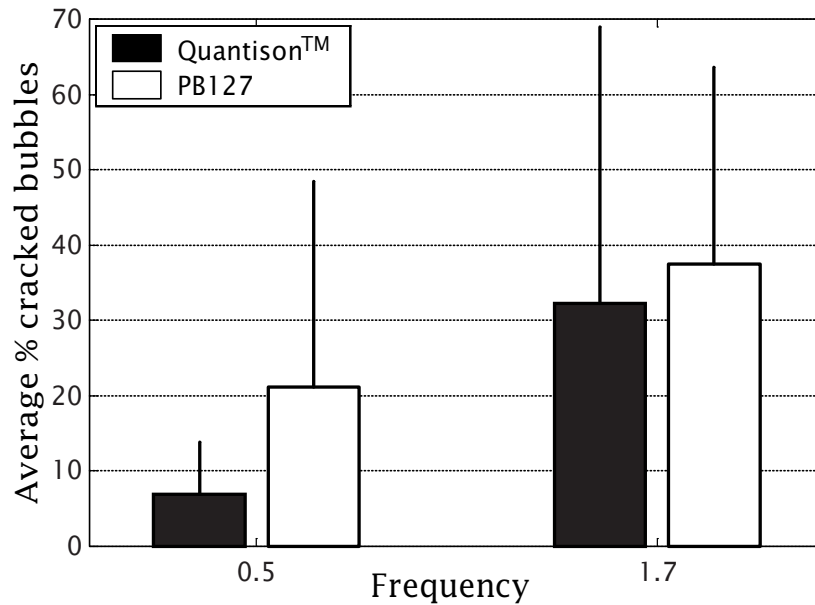


Figure 6.9: Average number of cracked contrast agent bubbles for $MI > 0.8$.

have been observed to crack during a subsequent ultrasonic burst.

After sonic cracking, contrast bubbles of both agents can stay acoustically active. Gas remainder has been observed inside the shells from sonically cracked bubbles, which was released by a subsequent ultrasonic burst.

4 Discussion and conclusions

We can only speculate on why certain bubbles crack while others stay intact. Tiny flaws in the shells may account for this observation. Such flaws are apparently formed or widened during ultrasound insonification, causing the bubble to crack during a subsequent ultrasonic burst.

The difference in average cracking percentage observed at 0.5 MHz and 1.7 MHz, may lie in the proximity of the resonance frequency of the agent to the insonifying frequency. The resonance frequency of Quantison™, *i.e.* 4 MHz, is closest to 1.7 MHz, indeed. So is the resonance frequency of

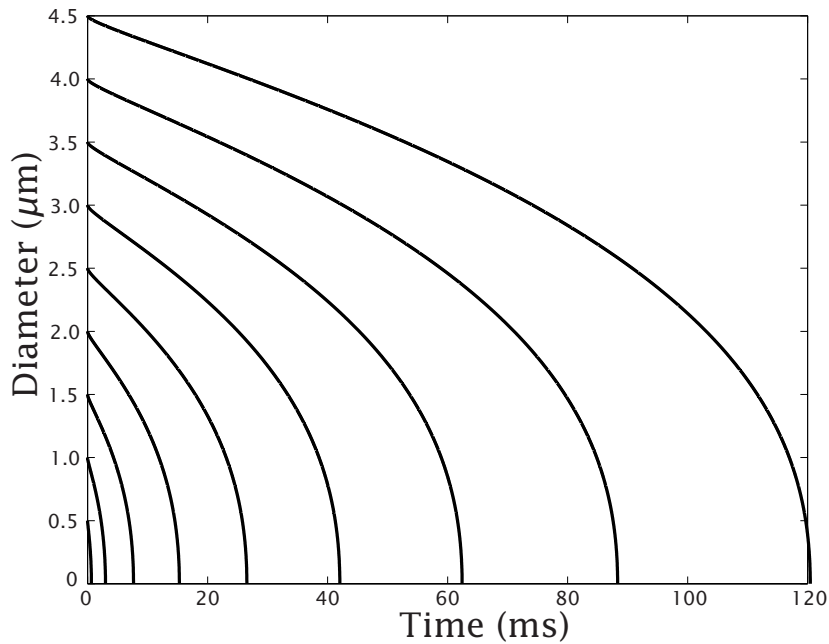


Figure 6.10: Dissolution of nitrogen microbubbles with diameters between 0.5 and 4.5 μm into saturated water at ambient pressure.

PB127, *i.e.* $6 < f_r < 7$ MHz.

The phenomenon of bubbles translating during an ultrasonic cycle has only been observed with free gas bubbles. We attribute this behavior to the small size of the free gas bubbles during contraction, and the lack thereof with the hard-shelled contrast agent bubbles. When in contraction phase, free gas bubbles have a very small translating mass, as it is equivalent to half the mass of the displaced fluid [102]. Because of impulse conservation, such small bubbles can translate further than the relatively big encapsulated bubbles.

The acoustic response from an ensemble of Quantison™ microbubbles disappears between 15 and 30 ms after transmission of a high-MI ultrasonic burst [11], whereas the disappearance time of the fundamental acoustic response of an ensemble of PB127 microbubbles lies between 50 and 100 ms after transmission of a high-amplitude ultrasonic burst [17]. Figure 6.10 demonstrates simulations of the dissolution of nitrogen mi-

[6, 4]

ULTRASOUND-INDUCED GAS RELEASE

microbubbles with diameters between 0.5 and 4.5 μm into saturated water at ambient pressure. Since most released gas bubbles have equilibrium diameters between 1.25 and 1.75 μm , they will disappear within 15 ms. The longer decay times measured in QuantisonTM [11] and PB127 [17] must be attributed to the relatively small number of large released gas bubbles around 4 μm . These large bubbles might be formed by coalescence of released gas bubbles or fragments [146].

For noninvasive pressure measurements, the influence of applying hydrostatic overpressures on the occurrence of sonic cracking will have to be investigated. Furthermore, the influence of pulse length and pulse repetition are of great practical interest.

Acknowledgments

We thank POINT Biomedical Corporation for supplying PB127, Upperton Limited for supplying QuantisonTM, Leo Bekkering and Jan Honkoop for technical assistance, and Cees Pakvis for drawing Figure 6.1.

7

Contrast Microbubble Phenomena: Overview

Abstract

When encapsulated microbubbles are subjected to high-amplitude ultrasound, the following phenomena have been reported: oscillation, translation, coalescence, fragmentation, sonic cracking, and jetting.

In this Chapter, we explain these phenomena, based on theories that were validated for relatively big, free (not encapsulated) gas bubbles. These theories are compared with high-speed optical observations of insonified contrast agent microbubbles. Furthermore, the potential clinical applications of the bubble-ultrasound interaction are explored.

We conclude that most of the results obtained are consistent with free gas bubble theory. Similar to cavitation theory, the number of fragments after bubble fission is in agreement with the dominant spherical harmonic

© 2004 World Federation for Ultrasound in Medicine & Biology. Reprinted with permission from Postema M, van Wamel A, Lancée CT, de Jong N. Ultrasound-induced encapsulated microbubble phenomena. *Ultrasound Med Biol* 2004 30(6):827-840.

This work has been supported by the Technology Foundation STW (RKG.5104) and by the Interuniversity Cardiology Institute of the Netherlands.

[7, 1]

MICROBUBBLE PHENOMENA: OVERVIEW

oscillation mode. Remarkable are our observations of jetting through contrast agent microbubbles. The pressure at the tip of a jet is high enough to penetrate any human cell. Hence, liquid jets may act as remote-controlled microsyringes, delivering a drug to a region of interest.

Encapsulated microbubbles have (potential) clinical applications in both diagnostics and therapeutics.

1 Introduction

Blood does not reflect ultrasound well, but its response may be enhanced by gas microbubbles of a few micrometers in diameter that are introduced into the blood pool [57]. These microbubbles oscillate upon insonification, and generate as such a characteristic acoustic response.

An ultrasound contrast agent (UCA) is a liquid containing gas microbubbles that are encapsulated by a shell. UCAs are widely used in clinical diagnostic imaging [4, 57]. The intravascular use of UCA enhances the quantification of perfusion and blood flow [92, 190], and lowers the detectability threshold of tumor and tissue vascularization, using conventional Doppler instruments [16]. An overview of UCA detection procedures in ultrasound imaging has been presented by De Jong *et al.* [80], and an overview of UCA imaging innovations has been put forward by Chiou *et al.* [24].

To understand encapsulated microbubble behavior better in order to develop or enhance applications in diagnostics and therapeutics, UCA microbubbles have been subjected to high-speed photography. Postema *et al.* [142] gave an overview of publications on high-speed optical observations of insonified UCA.

Observations of dynamic UCA microbubble behavior have resulted in new insights and novel approaches in diagnostics and therapeutics: The nonlinear behavior of oscillating bubbles has led to the development of contrast harmonic imaging [159, 77, 76, 8, 9], whereas observations of bubble destruction have led to the development of high-MI imaging techniques [183, 53].

Targeted UCA delivery is based on microbubbles with ligands attached to them [92, 185]. These bubbles circulate through vessels and accumulate at a target tissue, thereby marking the target in ultrasound images. Klibanov [92] put forward the idea that targeted microbubbles may be applied for selective delivery to the areas where selective enhancement of the action of ultrasound would be required, and if such a bubble would

INTRODUCTION

[7, 1]

contain plasmid DNA, enzyme, or another therapeutic agent, it might be released at the site of interest during insonification. Another means of targeting was suggested by Dayton *et al.* [36]. They provided optical verification that microbubbles oscillate differently when inside neutrophils in response to insonification, and emit acoustic signals that are distinct from free microbubbles. Thus, microbubbles within neutrophils might be detected, providing a potential method to image activated neutrophils as they accumulate at sites of inflammation.

Recently, Unger *et al.* [184] gave an overview of the therapeutic applications of UCA microbubbles. They presented experimental results using UCAs for thrombolysis, drug delivery, and gene delivery. Other recent advances in local drug and gene delivery include the *in vivo* delivery of a virus vector, attached to albumin microbubbles [166], the *in vitro* and *in vivo* transfection of endothelial cells with plasmid DNA mixed with UCA [179], and the accelerated cellular drug uptake *in vitro* when UCA microbubbles are present [189]. Tachibana *et al.* [175] subjected cells in the presence of a photosensitive drug to continuous ultrasound, and noticed surface pores on the cells. Inducing porosities in cells with ultrasound, generally referred to as sonoporation, has potential applications in (tumor) cell lysis and selective delivery of drugs and genes into cells. Independently, it was demonstrated that moderate microbubble oscillations are sufficient to achieve rupture of lipid membranes, in a regimen in which the bubble dynamics can be accurately controlled [114]. This might enable the transport of drugs through the cell membrane.

At high acoustic amplitudes, destructive effects of UCA microbubbles have been observed, such as hemorrhaging [169, 116], and lysis [189]. Kudo *et al.* [96] performed an *in vitro* study on bovine arterial cell damage by ultrasound in combination with microbubbles. They found that the locations of damaged cells were similar to the locations where violent bubble collapse was observed, suggesting that bubble collapse is responsible for cell membrane damage.

In this Chapter, we present an overview of dynamic encapsulated microbubble behavior observed at high acoustic amplitudes. The mechanisms for each type of behavior, found in literature on free (not encapsulated) gas bubbles, acoustics, and cavitation, are correlated to our high-speed optical observations. Furthermore, we address the potential clinical applications of the phenomena.

Previously, some UCA microbubble destruction phenomena were categorized by Chomas *et al.* [27] and Postema *et al.* [141]. From our optical

[7, 1]

MICROBUBBLE PHENOMENA: OVERVIEW

observations, we discriminate the following categories: oscillation, translation, coalescence, fragmentation, sonic cracking, and jetting.

In the following subsections, we give a brief overview of these phenomena, and an explanation of their occurrence. Most theories on bubble behavior were validated for big, free (not encapsulated) microbubbles.

Oscillation

When a microbubble is exposed to an oscillating acoustic signal, it undergoes alternate expansions and contractions with the same amplitude and duration at low driving pressures [173]. This regimen of pulsation amplitudes has been referred to as *moderate* [187]. Bubble activity which may occur at relatively low-amplitude pressures has been denoted as *stable cavitation* [125]. As the driving pressure increases, more complex nonlinear interactions occur: greater bubble expansion amplitude than contraction amplitude, and relatively slow expansion followed by rapid contraction (collapse). This behavior has been referred to as *violent* [187] or *inertial* (or *transient*) *cavitation* [125, 49, 3]. It has been associated with the production of harmonic signals [142].

The transition from the *moderate* to the *violent* regimen is rather abrupt: For any driving pressure, there exists a transitional equilibrium microbubble radius R_0^{tr} , above which microbubbles pulsate like *inertial cavities* [48, 49, 64]. This transition is referred to as the *cavitation threshold*. A bubble is judged to have grown into an *inertial cavity* when its maximum radius is greater than approximately twice its equilibrium radius [48, 49].

A number of models for computing radius-time curves of insonified gas bubbles has been developed. These models differ both in complexity and in the range of acoustic amplitudes for which they can be used [187].

To model the behavior of UCA microbubbles, the presence of an encapsulation around the gas core has to be accounted for. Hence, we have to introduce parameters that describe the dynamic behavior of the shell.

Presently, two models have been used for modeling UCA microbubble oscillations. De Jong *et al.* [77] used a modified RPNNP equation, named after its developers Rayleigh, Plesset, Neppiras, Noltingk, and Poritsky. They accounted for the presence of a shell by introducing a shell stiffness and a shell friction parameter. Morgan *et al.* [129] used a modified Herring equation. They introduced the shell properties thickness, elasticity modulus, and viscosity. Both models are consistent with optical observations at low driving pressures [79, 129, 142]. Currently, models on UCA microbubble

oscillating behavior at high driving pressures have been under investigation [174].

Translation

Translations of UCA microbubbles in the direction of the sound field and towards each other have been frequently observed with high-speed cameras [32, 37, 33, 35, 146]. Microbubble translation in the direction of the sound field has been attributed to a primary radiation force resulting from a pressure gradient across the bubble surface. The translation is maximal in contraction phase [151]. It was demonstrated that the velocity v of a gas bubble in a steady fluid subjected to an ultrasound field can be calculated from the following ordinary differential equation [113, 152, 188, 107]:

$$\sum F = F_{\text{rad}} + F_d + F_a = \frac{d}{dt}(\rho_g V_b v) \approx 0, \quad (7.1)$$

where F_{rad} is the primary radiation force, F_d is the drag force, F_a is the added mass force, ρ_g is the density of the gas, and V_b is the volume of the bubble.

In a steady flow, averaging over one acoustic cycle, the added mass force for small accelerations is given by [152]:

$$F_a = -\rho C_m V_b \dot{v}, \quad (7.2)$$

where ρ is the density of the surrounding fluid, C_m is the added mass coefficient, which is $1/2$ for a sphere, whatever the Reynolds number [113], and $V_b \approx \frac{4\pi}{3} R_0^3$, in which R_0 is the ambient bubble radius.

Averaging over one acoustic cycle, the primary radiation force is given by [37, 182]:

$$F_{\text{rad}} = \frac{(p_{\text{ac}}^-)^2 R_0}{\rho c f} \frac{\delta_t \frac{f_r}{f}}{\left[\left(\frac{f_r}{f} \right)^2 - 1 \right]^2 + \left(\delta_t \frac{f_r}{f} \right)^2}, \quad (7.3)$$

where c is the speed of sound, p_{ac}^- is the peak rarefactional acoustic pressure, δ_t is the dimensionless total damping coefficient [124], and f_r is the bubble resonant frequency [124]. The drag force is given by [113, 182]:

$$F_d = -\frac{\pi \eta}{4} C_d \text{Re} R_0 v(t), \quad (7.4)$$

[7, 1]

MICROBUBBLE PHENOMENA: OVERVIEW

where η is the shear viscosity of the fluid, $\text{Re} = \frac{2\rho R_0}{\eta} |v(t)|$ represents the Reynolds number, and

$$C_d = \frac{24}{\text{Re}} \left(1 + 0.15 \text{Re}^{0.687}\right) \quad (7.5)$$

is the drag coefficient of a contaminated system [41], such as a contrast agent.

The microbubble translations towards each other have been attributed to secondary radiation forces: oscillating bubbles generate spatially varying pressure fields. If two bubbles are either both below or both above the resonant size, this results in attraction. However, if one bubble is below and the other is above the resonant size, they oscillate out of phase [136, 102, 151], causing the bubbles to recede from each other. The mean approach velocity v_a of two identical bubbles is given by [37]:

$$v_a = -\frac{(2\pi f p_{ac}^-)^2}{27\eta} \rho \kappa^2 \frac{R_0^5}{d_0^2}, \quad (7.6)$$

where d_0 is the distance between the centers of the two bubbles, and κ is the compressibility of the bubble

$$\kappa = \frac{1}{\rho} \frac{\partial \rho}{\partial p}, \quad (7.7)$$

in which $\frac{\partial \rho}{\partial p}$ is the partial derivative of the density with respect to the pressure.

Coalescence

Ultrasound-induced microbubble coalescence is the fusion of two or more microbubbles. As adjacent bubbles expand, the pressure in the film between them increases, resulting in a deformation (flattening) of the bubble surfaces. The continuing bubble expansion causes drainage of the interposed film. This thinning continues until a critical thickness around $0.1 \mu\text{m}$ is reached, at which the Van der Waals attractive forces result in film rupture and the coalescence of the bubbles [43]. Thinning and rupture of thin liquid films have been described by Sheludko [162], Kralchevsky *et al.* [95], and Narsimhan & Ruckenstein [130].

Flattening of the adjacent bubble surfaces occurs if and only if the bubble system has a Weber number $\text{We} > 0.5$ [21]. The Weber number for a

fluid containing two bubbles with radii R_1 and R_2 , respectively, is given by the inertial force relative to the surface tension force:

$$\text{We} = \frac{\rho u^2}{\sigma R_m}, \quad (7.8)$$

where u is the relative approach velocity of the bubble walls, ρ is the fluid density, σ is the surface tension, and R_m is the mean bubble radius for which holds: $\frac{2}{R_m} = \frac{1}{R_1} + \frac{1}{R_2}$. In our results, Weber numbers are relatively high because of the rapid bubble expansions, with maximal radius increases of several m s^{-1} . If the Weber number is lower than 0.5, bubble coalescence will always occur, without flattening of the adjacent surfaces prior to contact [21].

In a separate paper, we investigated the coalescence mechanism of microbubbles, based on high-speed optical observations of insonified UCA [146] (*cf.* Chapter 3). We investigated the mechanism of film drainage by comparing the observed coalescence times with calculated film drainage times for mobile interfaces and immobile interfaces (7.9). The drainage time τ_d of an interposed film with immobile interfaces until a critical thickness h_c is given by:

$$\tau_d = \frac{3 \eta R_f^2 R_m}{8 \sigma h_c^2}, \quad (7.9)$$

where R_f is the film radius, and R_m is the mean bubble radius. The drainage time of a film with mobile interfaces is three times as low.

The calculated drainage times for immobile interfaces prove too long to be compatible with the observations. Stated differently, if the film between bubbles thinned by eq. (7.9) alone during the observed time span, it would only reach a minimum thickness that is much larger than that needed to induce film rupture. Hence, a mechanism for film rupture might be at work that overrules the drainage. We investigated if shape instabilities of the bubble can cause local corrugations that bridge the film and rupture it, before thinning of the whole film [145]. Although small perturbations on the bubble surface may grow tremendously, a phenomenon known as parametric instability, sufficiently large perturbations to bridge the liquid film cannot be formed within the times observed.

Bounce is the process where bubbles approach and flatten, but do not coalesce [146]. This behavior has been attributed to the drainage given in eq. (7.9) taking more time than the expansion phase.

[7, 1]

MICROBUBBLE PHENOMENA: OVERVIEW

Fragmentation

Fragmentation is the fission of a bubble into smaller bubbles [141]. Although acoustical observations have been associated with microbubble destruction [165], fragmentation of UCA microbubbles was first visualized with high-speed cameras in 2001 [27, 140]. In the same year, Brennen [14] computed the number of fragments for a cavitation bubble distorted by spherical harmonics. He demonstrated that, for any positive

$$\Gamma = \frac{\rho R^2 \ddot{R}}{\sigma}, \quad (7.10)$$

where \ddot{R} denotes the second time derivative of R , there must be a mode n for which the spherical harmonic distortion has a maximum. This mode depends on Γ as

$$n = \frac{1}{3} \sqrt{7 + 3\Gamma} - \frac{2}{3}. \quad (7.11)$$

The number of fragments N is estimated $N \approx n^3$.

Chomas *et al.* [28] showed that fragmentation occurs around peak contraction, when the bubble collapse is driven by inertial forces, since the inward acceleration continues to increase as the bubble approaches its minimum radius and suddenly changes sign as the bubble begins a rebound. They suggest that if the energy that is transferred during collapse is not sufficiently dissipated during one ultrasonic cycle, the bubble will become unstable and fragment.

Longuet-Higgins [109] related the intrinsic energy of a bubble fragment population with a size distribution $P(R)$ to the initial intrinsic energy of the mother-bubble with equilibrium radius R_0 :

$$E^* = \int_0^\infty \left(\frac{R}{R_0} \right)^2 P(R) dR, \quad (7.12)$$

where E^* is the intrinsic energy ratio, and R is the radius of a fragment. For bubble fragments of equal sizes,

$$E^* = \frac{R_0}{R} = \sqrt[3]{N}. \quad (7.13)$$

Longuet-Higgins [109] also presented an elegant method to compute the size distribution of bubbles generated by “shattering a single air cavity”.

Sonic cracking

Sonic cracking is the ultrasound-induced formation of a shell defect causing gas to escape from UCA microbubbles. It has been observed with rigid-shelled UCA microbubbles [34, 178, 141]. The physical mechanism behind sonic cracking is yet not known. Tiny flaws in the shells may account for the fact that certain bubbles crack while others stay intact [141].

Jetting

When a bubble rapidly contracts (collapses) near a boundary, this collapse will be asymmetrical. A high-speed liquid jet may form which projects through the bubble towards the boundary [3], pulling a slight volume of the bubble content along. This remarkable phenomenon is called jetting.

The jetting phenomenon for cavitation bubbles was described by Philipp & Lauterborn [138] and depicted by Ory (*cf.* Figure 7.1): The asymmetric collapse causes the velocity of the upper bubble wall to exceed the velocity of the lower wall in order to conserve the impulse of the bubble/fluid system. Consequently, the fluid volume above the bubble is accelerated and focused during collapse, leading to the formation of a liquid jet directed towards the boundary. This jet hits the lower bubble wall, causing a funnel-shaped protrusion and finally impacts on the boundary.

Jets have regularly been observed with cavitation bubbles [99, 138]. An illustrative enlargement of a high-speed photograph of a cavitation jet in the millimeter range was published by Lauterborn & Ohl [100]. Ohl & Ory [135] calculated the shapes of asymmetrically collapsing bubbles. Their results are consistent with photographs of a collapsing cavitation bubble developing a jet. Kodama & Takayama [94] studied the impact of jets on gelatin surfaces. They found that the radius of the jet R_j is approximately related to the radius of the bubble on the verge of collapsing R_c as: [94, 134]

$$\frac{R_j}{R_c} \approx 0.1. \quad (7.14)$$

The length of the jet l_j , defined as the full travel path of the propelled liquid, is approximately related to R_c as [134]:

$$\frac{l_j}{R_c} \approx 3. \quad (7.15)$$

[7, 1] MICROBUBBLE PHENOMENA: OVERVIEW

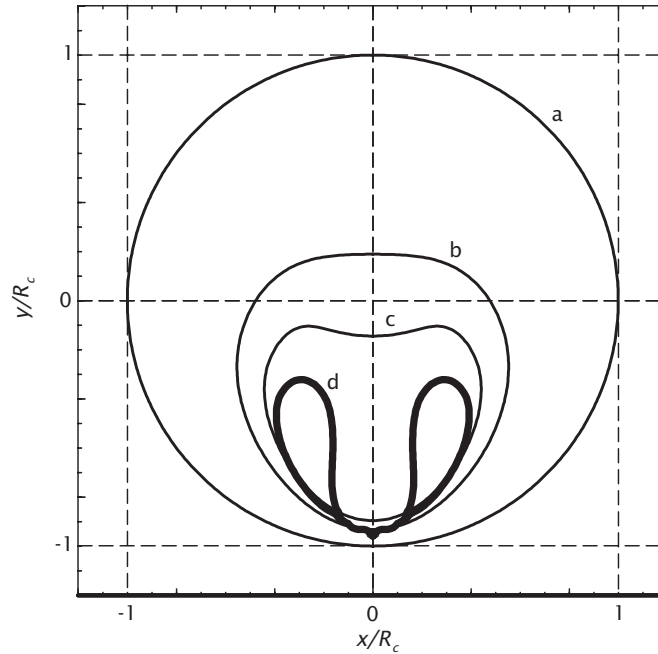


Figure 7.1: Schematic evolution of jet development in a collapsing bubble near a boundary (below): bubble on the verge of collapse (a), asymmetric collapse (b), jet development (c), funnel-shaped protrusion (d).

From these two ratios the amount of liquid within the jet, V_j , is estimated [134]:

$$V_j \approx 0.1 R_c^3 . \quad (7.16)$$

The impact of a jet on a surface generates a high-pressure region. The pressure in this region happens similarly to the *water-hammer pressure* effect [31]. For a perfectly plastic impact, the water-hammer pressure of a cavitation jet was estimated by de Haller [62] and Ohl & Ory [135]:

$$p_{wh} \approx \frac{1}{2} \rho c v_j , \quad (7.17)$$

where p_{wh} is the water-hammer pressure, v_j is the jet velocity, ρ is the fluid density, and c is the speed of sound.

The damage caused by a jet can be estimated by comparing the water-hammer pressure to the maximum stress the impact surface can withstand

before rupture. The maximum stress τ_{\max} is given by:

$$\tau_{\max} = E \varepsilon_r , \quad (7.18)$$

where E is the elastic (Young's) modulus of the material, and ε_r is the relative deformation of the surface before rupture.

Clinical applications

UCA microbubble oscillating behavior is the basis of most diagnostic imaging techniques [4, 57]. Since oscillating microbubbles provide a means to discriminate blood from tissue, they are applicable in perfusion and flow imaging, and tumor detection [16, 191, 190].

Medical applications of the manipulation of the movement of UCA microbubbles by means of acoustic energy will be primarily in directing UCA toward cells [35].

If small UCA microbubbles, having passed through the narrowest vessels, coalesce, they may be controlled to obtain resonant sizes. Especially for subharmonic imaging [160], where twice the resonant bubble size is needed, and for tracking the diffusion of free gas bubbles with subharmonics, a promising technique in noninvasive blood pressure measurements [144], controlled microbubble coalescence may be applicable. If coalescence of a lipid-shelled microbubble and a cell membrane can be induced, this will imply a promising technique in targeted drug delivery.

Bouncing behavior of UCA microbubbles has got no potential medical application yet.

UCA microbubble fragmentation has been associated with violent effects, such as cell membrane permeabilization and lysis. The reason for this may lie in the fact that fragmenting bubbles produce shock-waves. Because of the strong acoustic signal generated, fragmentation finds applications in high-MI imaging. The applicability of microbubble fragmentation for local drug delivery is fully dependent of the presence of a shell after fragmentation. If the shell is absent after fragmentation, the fragments will behave as released gas bubbles. Thus, the potential therapeutic applications will then be identical to those for sonic cracking.

Sonic cracking may find applications in drug delivery, if the released bubble content has therapeutic properties [52]. Frinking *et al.* [53] suggested a technique they called release burst imaging: Upon transmission of a high-MI ultrasound burst, there will be a strong scattering response

[7, 2]

MICROBUBBLE PHENOMENA: OVERVIEW

from the released gas bubbles. The free gas will rapidly dissolve, and with it the strong scattering response will fade away. Wei *et al.* [191] proposed that the acoustical measurement of the reappearance of UCA microbubbles may provide a means for determining tissue perfusion in any organ accessible to ultrasound.

The diffusion rate of a gas bubble with a certain size is known for every hydrostatic pressure. By making use of the changing acoustic properties of the dissolving gas bubbles, hydrostatic pressures may be determined in a minimally invasive clinical setting [10, 144].

It has been speculated that jets may be formed when UCA microbubbles in the bloodstream are insonified with high enough acoustic pressures. These jets would be directed towards a boundary like a cell or a capillary wall with adjacent cells. As such, jets might function as microsyringes [126, 134], if they could penetrate cells. The maximum extension measured in human cells is less than 50% ($\epsilon_r < 0.5$) [103]. Therefore, we may assume that for any human cell or cell part, $\epsilon_r \ll 1$. Elastic moduli of human cells were measured $E \approx 7.3$ kPa for endothelial cells [119], and $E \approx 12$ kPa for fibroblasts [156]: less than half the elastic modulus of murine skeletal muscle cells ($E \approx 24$ kPa) [118]. Rabbit cardiac cells are among the stiffest, with $E \approx 100$ kPa [118]. It is safe to assume that even for the stiffest human cell $E \ll 200$ kPa. Combining both assumptions in eq. (7.18) gives $\tau_{\max} \ll 200$ kPa. If the water-hammer pressure of a jet exceeds this stress, the jet will be able to penetrate any human cell.

The porosities observed on cell-membranes by Tachibana *et al.* [175] may well be attributed to jets. Probably, particles that were present in the photosensitive drug acted as cavitation nuclei, whereas the cell-membranes acted as the boundaries towards which the jets were directed.

2 Experimental setup

Overview

For the high-speed observations, we made use of the Brandaris-128 system [22] and an Imacon 468 fast framing camera. An overview of this experimental setup is shown in Figure 7.2. A computer controlled the triggering of a waveform generator, a Xenon flash source, and the cameras.

The electrical signal was generated by an AWG 520 arbitrary waveform generator (Tektronix, Inc., Beaverton, OR), or by an LW 420A arbitrary

EXPERIMENTAL SETUP

[7, 2]

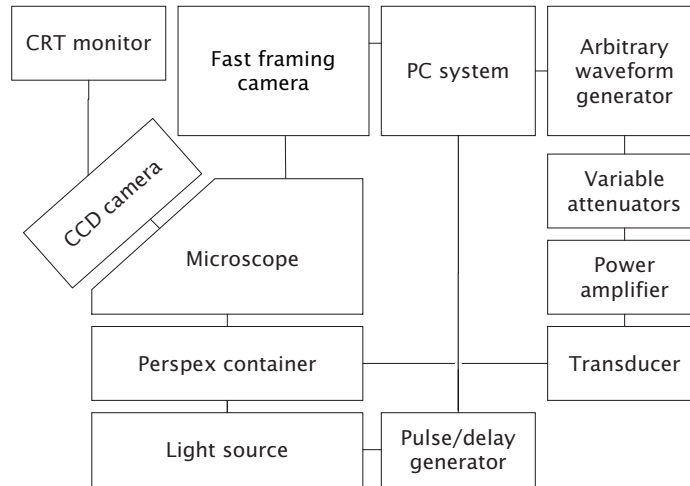


Figure 7.2: Basic setup of the high-speed photography system.

waveform generator (LeCroy Corp., Chestnut Ridge, NY). The signal was adjusted by two variable 355C/D attenuators (Hewlett Packard Company, Palo Alto, CA) in series, and an A-500 60 dB linear power amplifier (ENI technology, Inc., Rochester, NY). It was converted to ultrasound by a v389-SU 500 kHz, or by a v397-SU 2.25 MHz single-element transducer (Panametrics Inc., Waltham, MA), both spherically focused at 7.5 cm. The transducers were mounted in a Perspex container at an angle of 45° relative to the top of the container. This container was filled with saturated water. A \varnothing 200 μ m cellulose Cuprophan[®] capillary tube (Membrana GmbH, Wuppertal, Germany) was fixed in the focal area of the transducer, through which contrast agent was flowing. Because the capillary tube was water-soaked and much smaller in diameter than the acoustic wavelength, it was not expected to interfere with the ultrasound transmitted. Without contrast agent inserted, we did not observe reflections from the tube.

Optics

Underneath the capillary tube an optic fiber was mounted. This fiber was connected to an MVS-7010 Fiber Optic Strobe (PerkinElmer Optoelectronics, Salem, MA), and to a KLS-201 continuous fiber light source (Olympus KMI (KeyMed Ltd), Southend-on-Sea, UK). The pulsed light source was trig-

[7, 2] MICROBUBBLE PHENOMENA: OVERVIEW

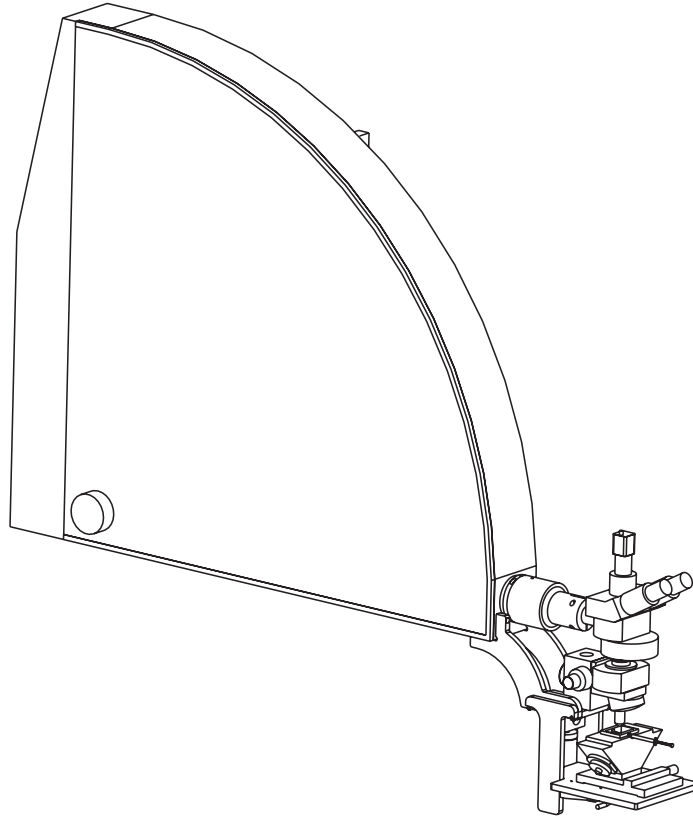


Figure 7.3: Line drawing of the Brandaris-128 system.

gered by a PM 5716 pulse/delay generator (Koninklijke Philips Electronics N.V., Eindhoven, The Netherlands). The container was positioned beneath a customized BXM microscope system (Olympus Optical Co., Ltd., Tokyo, Japan) with a U-CA magnification changer (Olympus Optical Co., Ltd.), switched to 2 \times magnification and a LUMPlanFI 60 \times water immersion objective lens (Olympus Optical Co., Ltd.). For the measurements with the Imacon 468 camera, we made use of a BH-2 model (Olympus Optical Co., Ltd.) with an SPlan 100 oil immersion objective lens (Olympus Optical Co., Ltd.). For image control purposes, an LCL-902K or a WAT-902HS CCD camera (Watec Co., Ltd., Yamagata, Japan) was fitted to the micro-

EXPERIMENTAL SETUP

[7, 2]

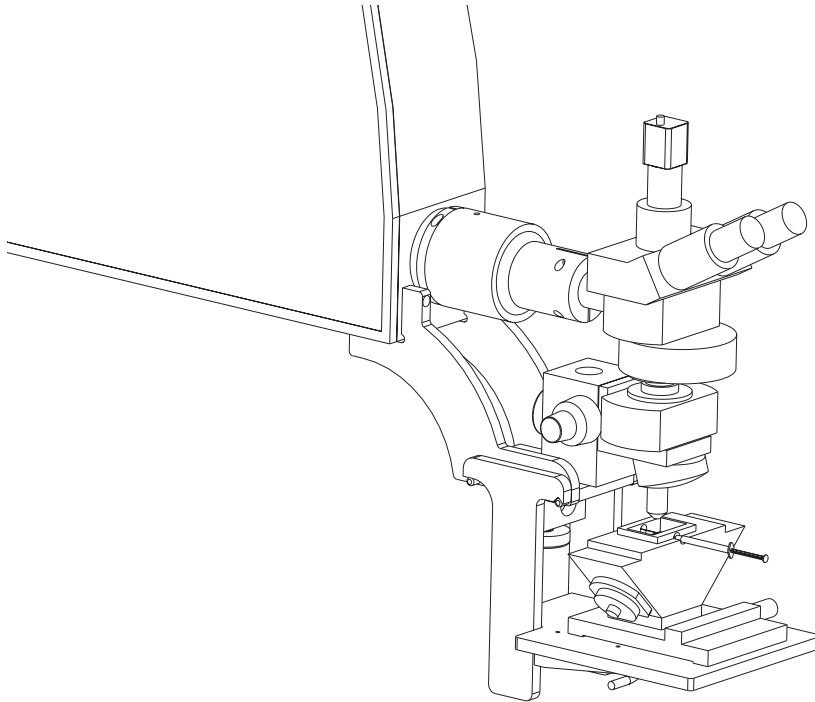


Figure 7.4: Line drawing of the optical observation part of the Brandaris-128 system.

scope. Focusing was done manually at the middle of the cellulose tube. Because the tube was wide compared to the contrast microbubbles measured, its upper half was considered a flat surface between contrast microbubbles and object lens, not causing aberrations but lowering the dynamic range of the images.

Camera

The optical observations were recorded with a Brandaris-128 fast framing camera system [22]. The Brandaris-128 captured sequences of 128 image frames at an average speed of 13 million frames per second. Typical frame sizes correspond to $89 \times 68 \mu\text{m}^2$. In all observations, image frames were captured before, during, and after ultrasound insonification. A line

[7, 2]

MICROBUBBLE PHENOMENA: OVERVIEW

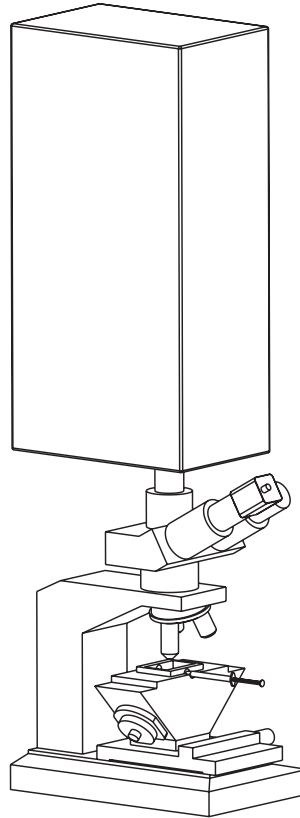


Figure 7.5: Line drawing of the optical observation of the Imacon 468 system.

drawing of the optical observation part of the setup is shown in Figure 7.3 and 7.4.

Furthermore, we made use of an Imacon 468 fast framing camera (DRS Hadland, Ltd., Tring, UK), capturing eight two-dimensional frames at 3 MHz. In all observations, the first frame was taken a few microseconds before ultrasound waves reached the contrast agent. The other seven frames were taken during ultrasound insonification, with 330 ns interframe time for 500 kHz ultrasound, spanning a full ultrasound cycle. Frame exposure times ranged from 10 ns to 70 ns. A line drawing of the optical observation part of this setup is shown in Figure 7.5.

Contrast agents

We investigated the ultrasound contrast agent Quantison™ (Upperton Limited). It consists of human serum albumin-encapsulated air bubbles with a mean diameter of $3.2 \mu\text{m}$. Shell thicknesses are between 0.2 and $0.3 \mu\text{m}$ [54]. The content of a Quantison™ vial was resuspended in 5 ml of Isoton® II (Beckman Coulter, Inc., Fullerton, CA), and shaken gently for 20 seconds before further dilution. The agent was inserted through the capillary tube using a syringe pressed by hand.

We also investigated an experimental UCA (supplied by Bracco Research SA, Geneva, Switzerland). It consists of phospholipid-encapsulated gas bubbles ranging in diameter from 1 to $6 \mu\text{m}$ with a median of $2 \mu\text{m}$. The acoustic behavior of a very similar contrast agent was modeled and described in [58]. Undiluted UCA (5ml of a 0.9% sodium chloride dilution, added to a 25 mg UCA vial) was inserted through the capillary tube using either a syringe pressed by hand or a hose operated by a gravity fed or pumped infusion.

Ultrasound

For the experiments with the Brandaris-128 camera system, the UCA bubbles were insonified by 8 cycles of 1.7 MHz ultrasound at a peak rarefactional acoustic pressure of 2 MPa, corresponding to a mechanical index of $MI = 1.5$. For the experiments with the Imacon 468 camera, the UCA bubbles were insonified by 10 cycles of 500 kHz ultrasound at peak rarefactional acoustic pressures between 0.66 and 0.85 MPa, corresponding to mechanical indices in the range $0.9 < MI < 1.2$. The mechanical index is defined as $MI = p_{ac}^- / \sqrt{f}$, where p_{ac}^- is the peak rarefactional acoustic pressure normalized by 1 MPa and f is the center frequency of the ultrasound normalized by 1 MHz.

Acoustic pressures applied were measured with a calibrated MH28-10 hydrophone (FORCE Technology, Brøndby, Denmark) in a separate water tank. An example of the acoustic signal measured at the transducer focus has been published in [142]. The *in-situ* reverberant component due to the presence of the microscopic lens was observed to be less than -14 dB. Thus, it is assumed the *in-situ* acoustic signal is comparable to the signal measured.

[7, 3]

MICROBUBBLE PHENOMENA: OVERVIEW

Procedure

We recorded 277 image sequences with the Brandaris-128 system. We performed 527 experiments at high acoustic amplitudes with the Imacon 468 camera. Bubble sizes and distances were measured manually or by using a segmentation method described by Postema *et al.* [142].

3 Results and discussion

The following types of ultrasound-induced UCA microbubble behavior have been distinctly observed and categorized: oscillation, translation, coalescence, fragmentation, sonic cracking, and jetting.

Oscillation

Figure 7.6(i) shows an optical image sequence of two identical $\varnothing 6 \mu\text{m}$ moderately oscillating experimental UCA microbubbles freely flowing through a capillary tube. The frames have been taken during one cycle of ultrasound insonification, with a center frequency of 0.5 MHz and a mechanical index $MI = 0.09$. Inter-frame times for frames b to h are $0.33 \mu\text{s}$. Each frame corresponds to a $88 \times 58 \mu\text{m}^2$ area. Frame a has been taken prior to ultrasound arrival. Maximal sizes are reached in frame d with bubble diameters of $7.6 \mu\text{m}$, whereas minimal sizes are displayed in frame f with bubble diameters of $4.4 \mu\text{m}$. Thus, the expansion and contraction of the bubbles are symmetric. We do not expect a violent collapse in this regimen, since the maximum bubble radius is less than twice its equilibrium radius. The oscillating amplitude is represented in the left frame of Figure 7.6(iii). The solid line represents the radius-period curve of a free gas bubble [77]. Apparently, the UCA bubbles have comparable excursions to a free gas bubble.

Figure 7.6(ii) and the right frame of Figure 7.6(iii) show a similar situation for a $\varnothing 1.5 \mu\text{m}$ strongly oscillating microbubble insonified at $MI = 0.67$. Again, the UCA bubble excursion is comparable to a free gas bubble. At the acoustic amplitude applied there may be some energy loss in the shell, causing increased thermal damping. Maximum size is reached in frame e with a bubble diameter of $10.0 \mu\text{m}$, whereas minimum size is displayed in frame g with a bubble diameter of $0.57 \mu\text{m}$. The bubble oscillates highly asymmetrically. We expect the microbubble to grow into an *inertial cavity*

RESULTS AND DISCUSSION

[7, 3]

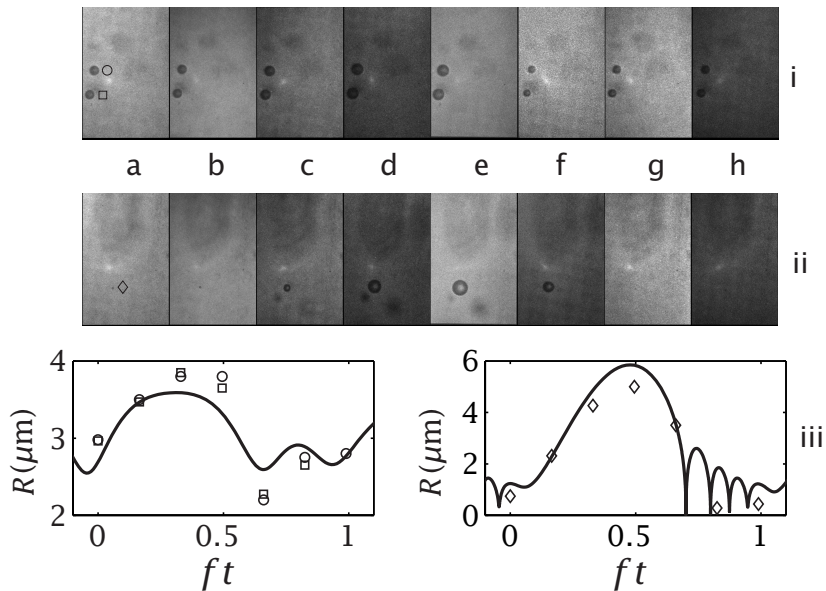


Figure 7.6: Oscillating experimental UCA microbubbles. Both respective image sequences span one ultrasonic cycle. Frames a have been captured prior to ultrasound arrival. Inter-frame times for frames b to h are $0.33 \mu s$. Each frame corresponds to a $88 \times 58 \mu m^2$ area. (i) Two $\varnothing 6 \mu m$ bubbles moderately oscillating ($MI = 0.09$). (ii) A $\varnothing 1.5 \mu m$ bubble strongly oscillating ($MI = 0.67$). (iii) Radius-period plots of both events. The solid line represents an oscillating free gas bubble.

in this regimen, since the maximum bubble radius is much greater than its equilibrium radius.

Translation

Figure 7.7 shows a high-speed optical image sequence of QuantisonTM insonified by 8 cycles of 1.7 MHz ultrasound with a mechanical index $MI = 1.5$. The ultrasound travels from the lower side of the frames to the upper side. Frame times are indicated in ns. Each frame corresponds to a $30 \times 16 \mu m^2$ area. In Figure 7.7(b,c,d) gas escapes from a $\varnothing 4 \mu m$ bubble. This free gas bubble expands and contracts, and translates towards the upper side of the frames. The displacement of the free gas bubble center has

[7, 3] MICROBUBBLE PHENOMENA: OVERVIEW

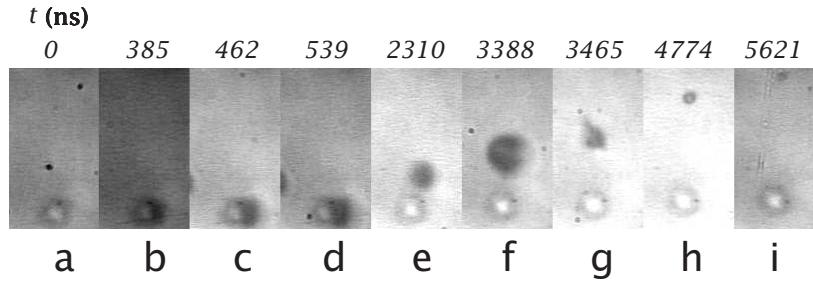


Figure 7.7: (a-d) Sonic cracking of a $\varnothing 4 \mu\text{m}$ Quantison™ bubble ($M_I = 1.5$). (e-i) The released gas is subjected to a primary radiation force. Each image frame corresponds to a $30 \times 16 \mu\text{m}^2$ area. Frames shown were selected from a sequence of 128 frames. The travel distance of the bubble center between (e) and (h) is $14 \mu\text{m}$ over 4 ultrasonic cycles.

been measured $14 \mu\text{m}$ over 4 periods (frames e-h). The resting diameter of the released bubble after insonification was $1.3 \mu\text{m}$. The theoretical mean bubble displacement over time has been computed by integrating eq. (7.1) over 4 periods, taking $c = 1480 \text{ m s}^{-1}$, $\rho = 998 \text{ kg m}^{-3}$, $R_0 = 0.65 \mu\text{m}$, $f = 1.7 \text{ MHz}$, $f_r = 5.3 \text{ MHz}$, $\delta_t = 1.0$, $p_{ac}(t) = [2 \text{ MPa}] \sin 2\pi f t$, and $\eta = 0.001 \text{ Pa s}$. The damping was computed using the parameters stated in Medwin [124] and De Jong [73]. The theoretical displacement is $18 \mu\text{m}$. The measured displacement is lower than the theoretical value. At the acoustic pressure applied, the expansion phase is longer than the contraction phase, which may account for this difference.

Figure 7.8 shows 5 image frames of two $\varnothing 4 \mu\text{m}$ experimental UCA microbubbles, each captured after insonification by 10 cycles of 0.5 MHz ul-

frame	d_0 (μm)	v_a (cm s^{-1})	Δd_{th} (μm)	Δd_m (μm)
a	21.2	15	3.0	3.2
b	18.0	20	4.0	3.9
c	14.1	33	6.6	6.4
d	7.7	111	> 7.7	7.7
e	0			

Table 7.1: Traveled distances and mean velocities of approaching bubbles.

trasound (duration $T_p = 20 \mu\text{s}$). Each image frame corresponds to a $30 \times 20 \mu\text{m}^2$ area. During every ultrasound burst the bubbles draw nearer to each other. For each center-to-center distance d_0 measured the mean approach velocity v_a has been computed from eq. (7.6), taking $\kappa = 5 \times 10^{-6} \text{ m}^2 \text{ N}^{-1}$ (Estimated from [73] and [37]). By combining d_0 with v_a , the theoretical distances $\Delta d_{\text{th}} = v_a T_p$ have been computed. These were compared to the distance Δd_m measured from Figure 7.8. The results are summarized in Table 7.1. The measured values Δd are consistent with theory.

Coalescence

Figure 7.9(i) shows an example of microbubble coalescence. The first frame has been captured prior to ultrasound arrival. In Figure 7.9(i)b), the main bubble with an initial diameter of $4 \mu\text{m}$ has split up, into several fragments with diameters below or around optical resolution, and these fragments have started to coalesce upon expansion. As the resulting two bubbles have expanded to mean diameters of approximately $2.7 \mu\text{m}$, shown in Figure 7.9(i)c), the flattening of the adjacent bubble surfaces is clearly visible. After the bubbles have expanded further to mean diameters of $4.6 \mu\text{m}$, as demonstrated in Figure 7.9(i)d), the interposed film has drained to a critical thickness to rupture (Figure 7.9(i)e), which has resulted in the formation of a single bubble (Figure 7.9(i)f).

The flattening of the adjacent bubble surfaces in Figure 7.9(i)b) is sup-

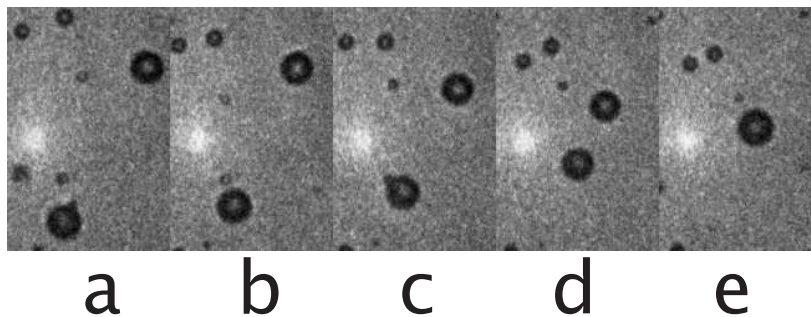


Figure 7.8: The approach of two $\varnothing 4 \mu\text{m}$ experimental UCA bubbles induced by a secondary radiation force. Each image frame corresponds to a $30 \times 20 \mu\text{m}^2$ area. Frames are each captured after insonification by 10 cycles of 0.5 MHz ultrasound ($MI = 0.67$).

[7, 3] MICROBUBBLE PHENOMENA: OVERVIEW

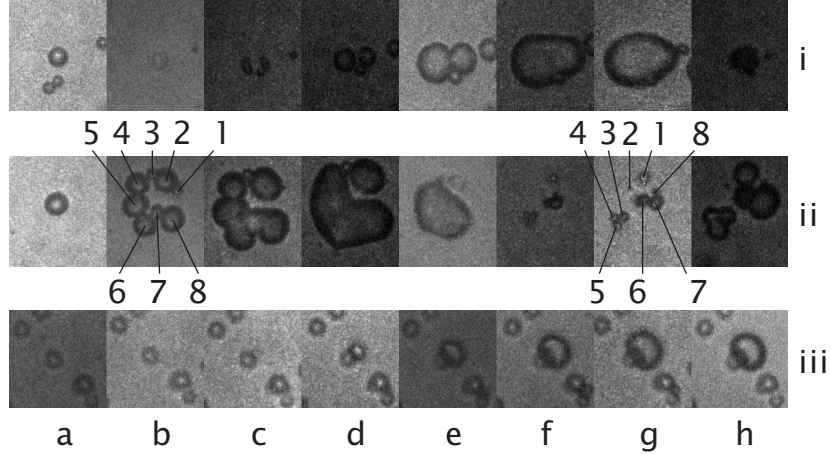


Figure 7.9: Experimental UCA microbubbles showing (i) coalescence, (ii) second mode spherical harmonic fragmentation, (iii) sonic cracking. Frames a have been captured prior to ultrasound arrival. Inter-frame times for frames b to h are $0.33 \mu\text{s}$. Each image frame corresponds to a $23 \times 23 \mu\text{m}^2$ area.

ported by a conservative estimate of the Weber number. Based on our analysis of the optical system [142], we may assume that the optical resolution $\mathcal{R} \ll 0.5 \mu\text{m}$, and fragment diameters in Figure 7.9(i)b) $< 0.5 \mu\text{m}$. Even if the bubbles would expand linearly to the sizes observed in Figure 7.9(i)c), the approach velocity would still have to be

$$u \approx \frac{2 \Delta R_m}{\Delta t} > \frac{2.7 \mu\text{m} - 0.5 \mu\text{m}}{0.33 \mu\text{s}} = 6.7 \text{m s}^{-1}. \quad (7.19)$$

By taking $\rho = 998 \text{kg m}^{-3}$ and $\sigma = 0.072 \text{N m}^{-1}$, we obtain a Weber number $We > 0.8$. As stated before, flattening of the adjacent bubble surfaces is expected to occur if $We > 0.5$.

From eq. (7.9), it is expected that the drainage time of the film shown in Figure 7.9(i)c) until a critical thickness $h_c = 0.15 \mu\text{m}$ is $\tau_d = 0.3 \mu\text{s}$, taking $\eta = 0.001 \text{Pa s}$ and $R_f \approx \frac{2}{3} R_m$ [146]. However, Figure 7.9(i)d) shows not only film drainage, but also continuing bubble expansion. For these bubble diameters of $4.6 \mu\text{m}$, the interposed film would take $1.3 \mu\text{s}$ to drain. Still, $0.66 \mu\text{s}$ later the bubbles have coalesced, although the bubbles have continued to expand. This supports the theory that the expanded bubble surfaces may be considered mobile.

Fragmentation

Figure 7.9(ii) shows the repeated fragmentation, coalescence, and re-fragmentation of an experimental UCA microbubble with an initial diameter $\mathcal{D} = 6 \mu\text{m}$. Each frame corresponds to a $23 \times 23 \mu\text{m}^2$ area. Figure 7.9(ii)a was captured prior to ultrasound arrival. In Figure 7.9(ii)b the bubble has broken up into 8 discernable fragments, suggesting a mode $n = \sqrt[3]{8} = 2$ spherical harmonic instability. The fragments coalesce and form an ellipsoidal bubble in Figure 7.9(ii)e. Because the ellipsoidal shape can be discriminated, we may conclude that the second spherical harmonic mode is dominant. After collapse, the fragments in Figure 7.9(ii)f are too small to be counted, but in Figure 7.9(ii)g, captured while the fragments have begun to expand, 8 fragments can be discerned, which confirms the second mode instability.

Sonic cracking

Figure 7.9(iii) shows the sonic cracking of a $\varnothing 3 \mu\text{m}$ Quantison™ microbubble. Each frame corresponds to a $23 \times 23 \mu\text{m}^2$ area. In Figure 7.9(iii)d gas starts to escape from the bubble in the middle of the frame. It expands to approximately $\varnothing 8 \mu\text{m}$ in Figure 7.9(iii)g, and then begins to contract in Figure 7.9(iii)h.

Clearly, the gas bubble has been released from its rigid shell. However, in the image sequence, the pixel size ($0.15 \times 0.15 \mu\text{m}^2$) corresponds in approximation to the shell thickness. Thus, even if the optical resolution were on the order of the shortest wavelength of the light, the presence of tiny flaws in the rigid shell would not have been detectable.

Jetting

We recorded two optical sequences showing jet development in UCA microbubbles [143], one of which is shown in Figure 7.10. Figure 7.10(a) shows a microbubble with a radius $R_c = 8.43 \mu\text{m}$. Figure 7.10(b) has been captured $0.33 \mu\text{s}$ later. Liquid is propelled through the lower left and escapes from the upper right of the bubble. The jet has traveled over a length $l_j = 26.2 \mu\text{m}$ in $0.33 \mu\text{s}$, giving an average jet velocity $v_j = 79.4 \text{ m s}^{-1}$. The ratio $\frac{l_j}{R_c}$ is in agreement with the ratio put forward by Ohl & Ikink [134]. The volume of the jet is approximately $V_j \approx 0.1R_c^3 = 60 \text{ femtoliter}$.

[7, 4]

MICROBUBBLE PHENOMENA: OVERVIEW

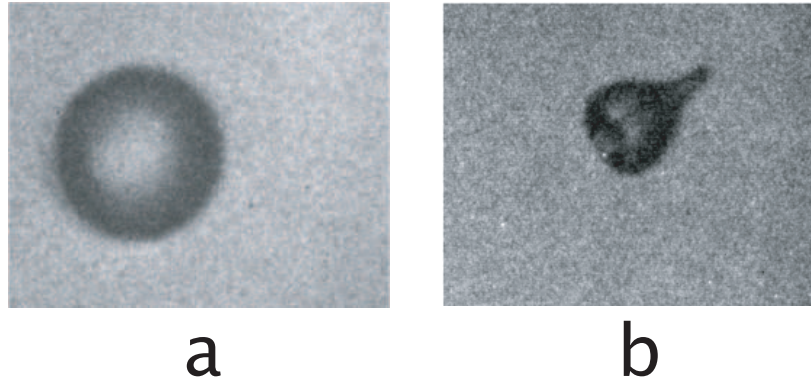


Figure 7.10: Ultrasound-induced jet development in an experimental UCA microbubble ($M_I = 1.2$). Each image frame corresponds to a $38 \times 30 \mu\text{m}^2$ area. Inter-frame time is $0.33 \mu\text{s}$ and exposure time is 10 ns .

Taking $\rho = 998 \text{ kg m}^{-3}$ and $c = 1480 \text{ m s}^{-2}$, the water-hammer pressure is around 60 MPa . Since $p_{\text{wh}} \gg 200 \text{ kPa} \gg \tau_{\text{max}}$, such a jet may penetrate any cell.

Influence of the capillary tube

Ishida *et al.* [70] demonstrated with simulations and high-speed optical observations, that if the distance between the walls of their solid test vessel was greater than 5 times the maximum free-field expansion radius of a cavitation bubble, the bubble would remain spherical while expanding. In our setup, the diameter of the water-soaked capillary tube is approximately 20 times the largest microbubble radius measured. Thus, the phenomena described other than jetting cannot be attributed to the boundaries imposed by the capillary tube, since our imaging plane is at the center of the tube.

4 Conclusions

An overview of dynamic behavior of ultrasound insonified encapsulated microbubbles has been presented. The following types of behavior have been observed and categorized: oscillation, translation, coalescence, fragmentation, sonic cracking, and jetting.

CONCLUSIONS

[7, 4]

Oscillation is the expanding and contracting bubble response to an oscillating acoustic signal. At low acoustic amplitudes bubbles pulsate moderately, at high amplitudes their longer expansion phase is followed by a violent collapse. Microbubble translation has been associated with primary and secondary radiation forces. Our optical observations of translating bubbles are consistent with theory. Coalescence, the fusion of two or more bubbles, is mainly caused by the drainage of the liquid film separating expanding bubbles, whereas bounce — unsuccessful coalescence — is caused by the drainage taking longer than the expansion of the bubbles. Fragmentation is the fission of a bubble into smaller bubbles. The number of fragments has been related to the dominant spherical harmonic oscillation mode of a bubble. In our observations, the second spherical harmonic mode appears to be the dominant mode. Remarkable are our observations of jetting through encapsulated microbubbles. For an observed jet, we computed a volume of approximately 60 femtoliter, generating a pressure at the tip of the jet around 60 MPa. This is high enough to penetrate any human cell. Hence, liquid jets may act as microsyringes, delivering a drug to a region of interest.

Table 7.2 gives an overview of potential clinical applications related to the encapsulated microbubble phenomena discussed. The phenomena have potential clinical applications in imaging, pressure measurements, tumor detection, permeabilization, lysis, targeting, and drug delivery.

	oscillation	translation	coalescence	fragmentation	sonic cracking	jetting
imaging	*		*	*	*	
pressure measurements			*	?	*	
tumor detection	*					
permeabilization and lysis				*		*
targeting		*	*			
drug delivery			*	?	*	*

Table 7.2: Potential clinical applications for encapsulated microbubble phenomena observed.

[7, 4]

MICROBUBBLE PHENOMENA: OVERVIEW

Acknowledgments

We thank Kees Slager for the data on cell elasticity, Emmanuel Ory (Laboratory of Applied Thermodynamics, Helsinki University of Technology) for computing Figure 7.1, Leo Bekkering and Elmer Koene for technical assistance, and Cees Pakvis for drawing Figures 7.3, 7.4, and 7.5.

8

General Considerations, Summary, and Future Prospects

1 General considerations and summary

As a result of investigations based on acoustic imaging methods, the use of ultrasound contrast agents are becoming widespread in clinical diagnostics. Since the acoustic interrogation of an agent takes place on an ensemble of bubbles, however, the contribution of an individual contrast agent microbubble to the acoustic response cannot be predicted. Therefore, the development of more sophisticated detection techniques, and the research on therapeutic applications of ultrasound contrast agents have to be based on other investigation methods, such as high-speed optical imaging.

In this thesis, we made use of fast-framing camera systems to observe dynamic behavior of individual microbubbles subjected to ultrasound. Multiple frames were captured during a single ultrasonic cycle. Previous studies made use of (one-dimensional) streak images, or frames that covered multiple ultrasonic cycles.

[8, 1]

GENERAL CONSIDERATIONS

Most of the observed phenomena described in this thesis occur within one ultrasonic cycle. The pictures on which these descriptions were based are asymmetric. Hence, the applicability of streak imaging and slower-than-sound framing in predicting microbubble behavior is very limited.

To account for the presence of a shell encapsulating the gas microbubble, the physical properties shell stiffness and shell friction have been accounted for in models describing microbubble oscillation. These properties have been measured for ensembles of ultrasound contrast agent microbubbles. From our results, however, it is suggested that the shell properties may differ between individual bubbles, because optically identical bubbles reveal different oscillating behavior.

The presence of a shell appears to be less of interest for ultrasound contrast agent microbubble phenomena observed at high acoustic pressures: The physical mechanisms of microbubble coalescence, fragmentation, translation, and jetting are comparable to those of free gas bubbles in the millimeter range. Because of the fast-framing, we are the first to notice repeated coalescence and fragmentation. Irregular shapes of insonified bubbles were previously interpreted and published in literature as modes of shape instability of a single bubble. However, these shapes may also be accounted for by coalescence of bubbles or bubble fragments.

We investigated the influence of the lipid shell on the coalescence by computing the film drainage for immobile bubble surfaces resulting in a laminar flow, and for mobile bubbles surfaces resulting in a plug flow. The coalescence of lipid-encapsulated microbubbles appeared to be unimpeded by shells.

Previously, release of gas from encapsulated microbubbles had been assumed from acoustical measurements. We demonstrated such release from encapsulated microbubbles with a rigid albumin shell during insonification. After this so-called ‘sonic cracking’, the free gas dissolves in the surrounding fluid. Although the mechanism of sonic cracking is not yet fully understood, the release of gas from encapsulations may find an application in noninvasive pressure measurements.

Determining overpressures is feasible *in vivo* from the decay of the fundamental acoustic response from diffusing released air bubbles. Pressure differences of 50 mmHg can be distinguished. In medical diagnostics a resolution lower than 50 mmHg is desirable. To improve the sensitivity of the measurement approach mentioned above, gases other than air might be used. Furthermore, subharmonics may be utilized as a marker for half resonant bubble size, since the subharmonic response is more sensitive to

bubble size change than the fundamental.

The phenomena observed have potential clinical applications in imaging, pressure measurements, tumor detection, permeabilization, lysis, targeting, and drug delivery.

2 Future prospects

Now that we know which phenomena may occur, it is time to quantify them under different conditions. Fragmentation, jetting, and sonic cracking can only be effective mechanisms in drug delivery, if their occurrence can be predicted.

When developing new ultrasound imaging techniques based on the microbubble behavior observed at high acoustic amplitudes, individual bubble contributions to the bulk acoustic response of an agent should be known or at least be estimated.

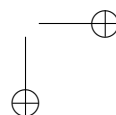
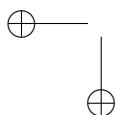
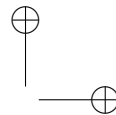
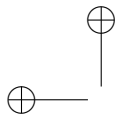
After *in vitro* quantification, drug-coated microbubbles and microbubbles containing *e.g.* anaesthetic gases revealing the same destruction behavior may be developed and studied. For bubbles containing drugs in the gas phase, sonic cracking should be the mechanism to focus on. For drug-coated bubbles, jetting would be the ideal release mechanism, since it effectively deals with the question how to penetrate the cell membranes. However, *in vitro* observations of jetting contrast microbubbles have been very rare. Thus, ideal conditions for jetting near cells have to be found.

We have demonstrated, that noninvasive pressure measurements are theoretically feasible, if noble gas can be released from encapsulated microbubbles, and its dissolution traced by means of the subharmonic acoustic response. In order to develop this novel clinical method, the first step is to make rigid-shelled encapsulated bubbles containing a noble gas, of which the released gas after sonic cracking has a narrow size distribution.

Furthermore, it should be studied whether bubbles can be forced to cluster and coalesce when subjected to ultrasound, so that emboli are created inside tumors.

International symposia on ultrasound contrast agents are shifting their attention from imaging to targeting and drug delivery. As the applications of medical bubbles become more diverse, the demand for medical bubbles with diverse behavior will grow.

In the near future, medical bubbles will play an important role, not only in ultrasonic imaging, but also in therapy.



Samenvatting

Met geluid kun je kijken. Dat wil zeggen: als je geluid produceert, reflecteert en vervormt het, afhankelijk van het voorwerp dat in de weg staat, en aan de hand van het teruggekaatste geluid zijn eigenschappen van dit voorwerp af te leiden. Ook eigenschappen die met het blote oog niet zichtbaar zijn.

Hoe hoger het geluid is dat gebruikt wordt, des te gedetailleerder is de informatie van het reflecterende voorwerp. Geluid boven de menselijke gehoorgrens wordt *ultrageluid* genoemd.

In de dierenwereld maken vleermuizen en dolfijnen gebruik van ultrageluidstechnieken voor afstands- en snelheidsbepaling. Sonar en Parking Distance Control zijn alledaagse technieken die van deze dieren afgekeken zijn.

In de echografie wordt geluid uitgezonden het lichaam in. Het vervormde, teruggekaatste geluid wordt afgebeeld in een *echogram*. Op deze manier kan een afbeelding gemaakt worden van delen van het lichaam, zonder dat het opengesneden hoeft te worden.

Bloed is — in tegenstelling tot ander weefsel — geen goede reflector. Daardoor is het met conventionele echografietechnieken moeilijk om de doorbloeding van organen te bepalen.

Een oplossing van dit probleem is het inspuiten van microscopisch kleine gasbelletjes (microbellen) in de bloedbaan. Gasbellen zetten uit wanneer de omgevingsdruk wordt verlaagd en krimpen in wanneer de omgevingsdruk wordt verhoogd. Geluid bestaat uit drukgolven, die de omgevingsdruk laten fluctueren. Het aantal fluctuaties per tijdseenheid (de frequentie) bepaalt de toonhoogte van het geluid. Bij hoorbaar geluid fluctueert de omgevingsdruk een paar keer tot een paar duizend keer per seconde. Bij medisch ultrageluid fluctueert de omgevingsdruk honderdduizenden tot vele miljoenen keren per seconde. Microbellen in zo'n geluidsveld gaan alternerend uitzetten en inkrimpen, met frequenties van dezelfde orde als het geluidsveld. Dit gedrag heet *oscilleren*, oftewel *slingeren*. Iedere oscillerende bel zendt radieel een drukveld uit en gedraagt

SAMENVATTING

zich daardoor zelf als een geluidsbron. Dus wanneer microbellen ingespoten worden in de bloedbaan, zijn ze door hun *karakteristieke respons* op ultrageluid op te sporen. Hun aanwezigheid is een indicatie voor de doorbloeding van individuele vaten en hele organen.

Dergelijke medische bellen worden gewoonlijk aangeduid met ultrageluid-contrastmiddelen. Ultrageluid-contrastmiddelen zijn voor klinisch-diagnostische doeleinden zo populair, dat er diverse soorten commercieel verkrijgbaar zijn. De meeste bestaan uit belletjes van een paar micrometer (miljoenste meter) in diameter. Om te voorkomen dat de belletjes te snel oplossen bevatten de contrastbellen een gas dat veel langzamer dan lucht oplost en zitten er schilletjes om de bellen.

Omdat een enkele injectie met contrastmiddel bestaat uit miljarden microbellen, kunnen we met ultrageluidstechnieken alleen het groepsgegedrag van microbellen meten. Voor de ontwikkeling van meer geavanceerde detectietechnieken en voor het onderzoek naar therapeutische toepassingen van microbellen is het van belang dat ook het gedrag van individuele microbellen vastgelegd en voorspeld kan worden. Daartoe kunnen optische technieken zoals hogesnelheidsfotografie gebruikt worden.

In deze studie werd gebruikgemaakt van hogesnelheidscamera's om het dynamisch gedrag van individuele microbellen onder invloed van ultrageluid waar te nemen. Binnen een enkele periode van een ultrageluidsgolf, maximaal 2 miljoenste seconde, werden zeven foto's gemaakt met sluitertijden tussen 10 en 70 miljardste seconde. In voorgaande studies werden één-dimensionale foto's gepubliceerd en foto's met sluitertijden langer dan de periode van de geluidsgolf. De verschijnselen die in deze studie beschreven worden, vinden meestal plaats binnen een enkele periode. Bovendien zijn de verschijnselen niet radieel symmetrisch. Daardoor zijn één-dimensionale fotografie en fotografie met “lange” sluitertijden beperkt qua voorspellend vermogen van belgedrag.

Aangezien contrastbellen een schilletje hebben, moet hiermee rekening gehouden worden bij de fysische beschrijving van het oscilleren. In bestaande modellen worden hiertoe de fysische grootheden schilstijfheid en schilfrictie gebruikt. Deze grootheden worden bepaald door metingen aan hoeveelheden contrastmiddel. Uit deze studie echter lijkt te volgen dat schileigenschappen van contrastbellen onderling kunnen verschillen, aangezien optisch identieke bellen verschillend slingergedrag vertonen.

De aanwezigheid van een schil blijkt minder van belang te zijn voor de verschijnselen die waargenomen worden bij contrastbellen in een ultrageluidsveld met een hoge akoestische amplitude: De fysische mechanis-

SAMENVATTING

men van microbelfusie, -fragmentatie, -translatie en -jetten zijn vergelijkbaar met de mechanismen voor vrije gasbellen (zonder schil) die duizend keer zo groot zijn. Door de hoge snelheid van de camera's is dit de eerste studie waarin zich herhalende microbelfusie en -fragmentatie zijn waargenomen. Onregelmatige vormen van bellen in een geluidsveld werden voorheen geïnterpreteerd en gepubliceerd als modes van vorminstabiliteit van een enkele bel. Deze vormen kunnen echter toegeschreven worden aan de fusie van bellen of belfragmenten.

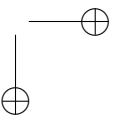
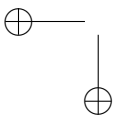
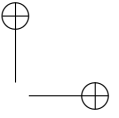
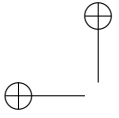
Drainagetijden van de dunne vloeistoffilm die bellen van elkaar scheidt, werden berekend met de Reynolds-vergelijking. De berekende tijden voor bellen met een schilletje zijn te lang om overeen te komen met optische waarnemingen van fusie van microbellen met een vetschilletje. Deze observaties kunnen wel verklaard worden wanneer de schillen zich als mobiele oppervlakken gedragen. Hierdoor worden de theoretische drainagetijden een factor drie verkort. Deze theorie is geverifieerd met optische waarnemingen van fusie van vrije gasbellen.

Op grond van akoestische metingen werd er voorheen aangenomen dat gas uit contrastbellen kan ontsnappen. In deze studie is aangetoond dat we onder invloed van ultrageluid gas kunnen laten ontsnappen uit contrastbellen met een rigide albumineschil. Na dit zogeheten *sonisch kraken* lost het vrije gas op in de vloeistof. Hoewel het mechanisme achter sonisch kraken nog niet uitgewerkt is, kan het laten ontsnappen van gas uit schillen in de nabije toekomst een toepassing vinden in niet-invasieve drukmeting.

Het bepalen van overdruk is in principe *in vivo* mogelijk aan de hand van het verval van de grondtoon van een oplossende vrije gasbel. Drukverschillen van 50 millimeter kwikdruk kunnen worden onderscheiden. In de medische diagnostiek is een kleinere resolutie wenselijk. Om de gevoeligheid van bovengenoemde meetmethode te verbeteren, zouden andere gassen dan lucht kunnen worden gebruikt. Aangezien ondertonen gevoeliger zijn voor een verandering in de belgrootte dan grondtonen, kan bovendien gebruik gemaakt worden van ondertonen om de halve resonantie-grootte van een bel te markeren.

De waargenomen verschijnselen zijn mogelijk klinisch toepasbaar in ultrasonische afbeelding, drukmeting, tumordetectie, doorbloedingsbepaling, lysis, targeting en gerichte medicijnbezorging.

Dit project wordt ondersteund door de stichting STW (RKG.5104).



Bibliography

- [1] Agard DA. Optical sectioning microscopy: Cellular architecture in three dimensions. *Annu Rev Biophys Bioeng* **1984** 13:191-219.
- [2] Aksoy BS. *Hydrophobic Forces in Thin Films of Water in the Presence and Absence of Surfactants*. Blacksburg: Virginia Polytechnic Institute and State University **1997**.
- [3] Barnett S. Nonthermal issues: cavitation — its nature, detection and measurement. *Ultrasound Med Biol* **1998** 24:S11-S21.
- [4] Becher H, Burns PN. *Handbook of Contrast Echocardiography: LV Function and Myocardial Perfusion*. Berlin: Springer-Verlag **2000**.
- [5] Bergeron V. Forces and structure in thin liquid soap films. *J Phys: Condens Matter* **1999** 11:R215-R238.
- [6] Berne RM, Levy MN, eds. *Physiology*. 3rd edition. St. Louis: Mosby — Year Book, Inc **1993**.
- [7] Bernoulli D. *Hydrodynamica, sive de viribus et motibus fluidorum commentarii*. Strasbourg: JH Dulsecker **1738**.
- [8] Bouakaz A, Frigstad S, Ten Cate FJ, de Jong N. Improved contrast to tissue ratio at higher harmonics. *Ultrasonics* **2002** 40:575-578.
- [9] Bouakaz A, Frigstad S, Ten Cate FJ, de Jong N. Super harmonic imaging: a new imaging technique for improved contrast detection. *Ultrasound Med Biol* **2002** 28(1):59-68.
- [10] Bouakaz A, Frinking PJA, de Jong N. Noninvasive pressure measurement using microbubble contrast agent and wavelet transforms. *Proc IEEE Ultrason Symp* **2000** 1907-1910.

BIBLIOGRAPHY

- [11] Bouakaz A, Frinking PJA, de Jong N, Bom N. Noninvasive measurement of the hydrostatic pressure in a fluid-filled cavity based on the disappearance time of micrometer-sized free gas bubbles. *Ultrasound Med Biol* **1999** 25(9):1407-1415.
- [12] Boys CV. On electric spark photographs; or, photography of flying bullets, etc., by the light of the electric spark. *Nature* **1893** 47:415-421.
- [13] Bragg W. *The World of Sound*. London: G Bell and Sons Ltd **1920**.
- [14] Brennen CE. Fission of collapsing cavitation bubbles. *Proc CAV 2001 4th Int Symp Cavitation* **2001**.
- [15] Brennen CE. Fission of collapsing cavitation bubbles. *J Fluid Mech* **2002** 472:153-166.
- [16] Burns PN, Hilpert P, Goldberg BB. Intravenous contrast agent for ultrasound Doppler: In vivo measurement of small tumor vessel dose-response. *Proc Annu Int Conf IEEE Eng Med Biol Soc* **1990** 12(1):322-324.
- [17] Burns PN, Karshafian R, Bevan P, de Jong N, Bouakaz A, Chin CT, Versluis M, Tickner G. Looking at and listening to breaking bubbles: a correlative optical acoustic study of some experimental polymer/air agents. *Abstr 9th Eur Symp Ultrasound Contrast Imaging* **2004** 11-16.
- [18] Chaudhari RV, Hofmann H. Coalescence of gas bubbles in liquids. *Rev Chem Eng* **1994** 10(2):131-190.
- [19] Chen JD, Slattery JC. Effects of London-van der Waals forces on the thinning of a dimpled liquid film as a small drop or bubble approaches a horizontal solid plane. *AIChE J* **1982** 28(6):955-963.
- [20] Chen WS, Matula TJ, Crum LA. The disappearance of ultrasound contrast bubbles: observations of bubble dissolution and cavitation nucleation. *Ultrasound Med Biol* **2002** 28(6):793-803.
- [21] Chesters AK, Hofman G. Bubble coalescence in pure liquids. *Appl Sci Res* **1982** 38:353-361.

BIBLIOGRAPHY

- [22] Chin CT, Lancée C, Borsboom J, Mastik F, Frijlink M, de Jong N, Versluis M, Lohse D. Brandaris 128: a 25 million frames per second digital camera with 128 highly sensitive frames. *Rev Sci Instru* **2003** 74(12):5026-5034.
- [23] Chin CT, Lancée C, Borsboom J, Mastik F, Versluis M, Lohse D, de Jong N. Optical imaging of ultrasound contrast bubble motions at 25 million frames per second. *Abstr 8th Eur Symp Ultrasound Contrast Imaging* **2003** 20-25.
- [24] Chiou KR, Liu CP, Chiang HT, Lin SL. Clinical applications of contrast echocardiography. *Acta Cardiol Sin* **2000** 16:63-78.
- [25] Chomas J, Dayton P, Allen J, Morgan K, Ferrara K. High speed optical experimental analysis of microbubble destruction, supported by theoretical development. *Abstr 4th Eur Symp Ultrasound Contrast Imaging* **1999** 52-55.
- [26] Chomas J, Dayton P, Morgan K, Allen J, Ferrara K. Optimization of microbubble destruction. *Proc IEEE Ultrason Symp* **1999** 1689-1692.
- [27] Chomas JE, Dayton P, Allen J, Morgan K, Ferrara KW. Mechanisms of contrast agent destruction. *IEEE Trans Ultrason, Ferroelect, Freq Contr* **2001** 48(1):232-248.
- [28] Chomas JE, Dayton P, May D, Ferrara K. Threshold of fragmentation for ultrasonic contrast. *J Biomed Opt* **2001** 6(2):141-150.
- [29] Church CC. The effects of an elastic solid surface layer on the radial pulsations of gas bubbles. *J Acoust Soc Am* **1995** 97(3):1510-1521.
- [30] Collins AC. *The Story of America in Pictures*. Garden City: Doubleday & Company, Inc **1953**.
- [31] Cook SS. Erosion by water-hammer. *Proc Roy Soc London A* **1928** 119:481-488.
- [32] Dayton P, Goode A, Morgan K, Klivanov S, Brandenburger G, Ferrara K. Action of microbubbles when insonified: experimental evidence. *Proc IEEE Ultrason Symp* **1996** 1131-1134.
- [33] Dayton P, Klivanov A, Brandenburger G, Ferrara K. Acoustic radiation force in vivo: a mechanism to assist targeting of microbubbles. *Ultrasound Med Biol* **1999** 25(8):1195-1201.

BIBLIOGRAPHY

- [34] Dayton P, Morgan K, Allietta M, Klibanov A, Brandenburger G, Ferrara K. Simultaneous optical and acoustical observations of contrast agents. *Proc IEEE Ultrason Symp* **1997** 1583-1591.
- [35] Dayton PA, Allen JS, Kruse DE, Ferrara KW. Experimental validation of a theoretical framework to predict radiation force displacement of contrast agents. *Proc IEEE Ultrason Symp* **2001** 1687-1690.
- [36] Dayton PA, Chomas JE, Lum AFH, Allen JS, Lindner JR, Simon SI, Ferrara KW. Optical and acoustical dynamics of microbubble contrast agents inside neutrophils. *Biophys J* **2001** 80:1547-1556.
- [37] Dayton PA, Morgan KE, Klibanov AL, Brandenburger G, Nightingale KR, Ferrara KW. A preliminary evaluation of the effects of primary and secondary radiation forces on acoustic contrast agents. *IEEE Trans Ultrason, Ferroelect, Freq Contr* **1997** 44(6):1264-1277.
- [38] Dayton PA, Morgan KE, Klibanov AL, Brandenburger GH, Ferrara KW. Optical and acoustical observations of the effects of ultrasound on contrast agents. *IEEE Trans Ultrason, Ferroelect, Freq Contr* **1999** 46(1):220-232.
- [39] Dey N, Boucher A, Thonnat M. Modélisation et étude de la formation de l'image d'un objet 3D translucide. *Presented at: 2ème colloque francophone Méthodes et Techniques Optiques pour l'Industrie* **2001**.
- [40] Dhainaut M. Literature study on observations and experiments on coalescence and breakup of bubbles and drops. Technical Report STF24 A02531, Trondheim: NTNU, Dept of Chemical Engineering **2002**.
- [41] Di Marco P, Grassi W, Memoli G. Experimental study on rising velocity of nitrogen bubbles in FC-72. *Int J Therm Sci* **2003** 42:435-446.
- [42] Dimitrov DS, Ivanov IB. Hydrodynamics of thin liquid films. On the rate of thinning of microscopic films with deformable interfaces. *J Colloid Interf Sci* **1978** 64(1):97-106.
- [43] Duineveld PC. *Bouncing and coalescence of two bubbles in water*. Enschede: PC Duineveld **1994**.
- [44] Endelman LL. A brief history of high speed photography 1851-1930. *Presented at: SPIE 32nd Annu Int Tech Symp* **1988** .

BIBLIOGRAPHY

- [45] Epstein PS, Plesset MS. On the stability of gas bubbles in liquid-gas solutions. *J Chem Phys* **1950** 18(11):1505-1509.
- [46] Fairbank Jr WM, Scully MO. A new noninvasive technique for cardiac pressure measurement: resonant scattering of ultrasound from bubbles. *IEEE Trans Biomed Eng* **1977** BME-24(2):107-110.
- [47] Flagello DG, Milster T, Rosenbluth AE. Theory of high-NA imaging in homogeneous thin films. *J Opt Soc Am A* **1996** 13(1):53-64.
- [48] Flynn HG. Cavitation dynamics. II. Free pulsations and models for cavitation bubbles. *J Acoust Soc Am* **1975** 58(6):1160-1170.
- [49] Flynn HG, Church CC. Transient pulsations of small gas bubbles in water. *J Acoust Soc Am* **1988** 84(3):985-998.
- [50] Fox FE, Herzfield KF. Gas bubbles with organic skins as cavitation nuclei. *J Acoust Soc Am* **1954** 26(6):984-989.
- [51] Frinking PJA. *Ultrasound Contrast Agents: acoustic characterization and diagnostic imaging*. Rotterdam: PJA Frinking **1999**.
- [52] Frinking PJA, Bouakaz A, de Jong N, Ten Cate FJ, Keating S. Effect of ultrasound on the release of micro-encapsulated drugs. *Ultrasonics* **1998** 36:709-712.
- [53] Frinking PJA, Céspedes EI, Kirkhorn J, Torp HG, de Jong N. A new ultrasound contrast imaging approach based on the combination of multiple imaging pulses and a separate release burst. *IEEE Trans Ultrason, Ferroelect, Freq Contr* **2001** 48(3):643-651.
- [54] Frinking PJA, de Jong N. Acoustic modeling of shell-encapsulated gas bubbles. *Ultrasound Med Biol* **1998** 24(4):523-533.
- [55] Fuller PWW, Rendell JT. The development of high speed photography. In Ray S, ed., *High speed photography and photonics*. Washington: SPIE **2002** 7-28.
- [56] Gibson SF, Lanni F. Experimental test of an analytical model of aberration in an oil-immersion objective lens used in three-dimensional light microscopy. *J Opt Soc Am A* **1991** 8:1601-1613.

BIBLIOGRAPHY

- [57] Goldberg BB, Raichlen JS, Forsberg F, eds. *Ultrasound Contrast Agents. Basic principles and clinical applications*. 2nd edition. London: Martin Dunitz Ltd **2001**.
- [58] Gorce JM, Arditi M, Schneider M. Influence of bubble size distribution on the echogenicity of ultrasound contrast agents: A study of SonoVue™. *Invest Radiol* **2000** 35(11):661-671.
- [59] Gramiak R, Shah PM. Echocardiography of the aortic root. *Invest Radiol* **1968** 3:356-366.
- [60] Gramiak R, Shah PM, Kramer DH. Ultrasound cardiography: contrast studies in anatomy and function. *Radiology* **1969** 92:939-948.
- [61] Groen FCA, Young IT, Ligthart G. A comparison of different focus functions for use in autofocus algorithms. *Cytometry* **1985** 6:81-91.
- [62] de Haller P. Untersuchungen über die durch Kavitation hergerufenen Korrosionen. *Schweiz Bauzeit* **1933** 101(21):243-246.
- [63] Harvey JT, Culvenor J, Payne W, Cowley S, Lawrance M, Stuart D, Williams R. An analysis of the forces required to drag sheep over various surfaces. *Appl Ergon* **2002** 33:523-531.
- [64] Hilgenfeldt S, Brenner MP, Grossmann S, Lohse D. Analysis of Rayleigh-Plesset dynamics for sonoluminescing bubbles. *J Fluid Mech* **1998** 365:171-204.
- [65] Hilgenfeldt S, Lohse D, Zomack M. Sound scattering and localized heat deposition of pulse-driven microbubbles. *J Acoust Soc Am* **2000** 107(6):3530-3539.
- [66] Hiraoka Y, Sedat JW, Agard DA. The use of a charge-coupled device for quantitative optical microscopy of biological structures. *Science* **1987** 238:36-41.
- [67] Hoff L. Acoustic properties of ultrasonic contrast agents. *Ultrasonics* **1996** 34:591-593.
- [68] Hornby AS. *Oxford Advanced Learner's Dictionary of Current English*. Oxford: Oxford University Press **1989**.
- [69] Isenberg C. *The science of soap films and soap bubbles*. Dover edition. Don Mills: General Publishing Company, Ltd **1992**.

BIBLIOGRAPHY

- [70] Ishida H, Nuntadusit C, Kimoto H, Nakagawa T, Yamamoto T. Cavitation behavior near solid boundaries. *Proc CAV 2001 4th Int Symp Cavitation* **2001**.
- [71] Ivanov IB, Dimitrov DS, Radoyev BP. Generalized equations of thin films hydrodynamics and their application to the calculations of the thinning rate of films with non-deformed surfaces. *Kolloid Zh* **1979** 41(1):36-42.
- [72] Jain AK. *Fundamentals of Digital Image Processing*. Englewood-Cliffs: Prentice-Hall **1989**.
- [73] de Jong N. *Acoustic properties of ultrasound contrast agents*. Rotterdam: N de Jong **1993**.
- [74] de Jong N, Bouakaz A, ten Cate F. Ultrasound contrast imaging: principles and applications. *Klinische Fysica* **2000**/3:24-31.
- [75] de Jong N, Bouakaz A, Frinking PJA, Ten Cate FJ. Contrast-specific imaging methods. In Goldberg B, Raichlen J, Forsberg F, eds., *Ultrasound Contrast Agents. Basic principles and clinical applications*, 2nd edition. London: Martin Dunitz Ltd **2001** 25-36.
- [76] de Jong N, Bouakaz A, Ten Cate FJ. Contrast harmonic imaging. *Ultrasonics* **2002** 40:567-573.
- [77] de Jong N, Cornet R, Lancée CT. Higher harmonics of vibrating gas-filled microspheres. Part one: simulations. *Ultrasonics* **1994** 32(6):447-453.
- [78] de Jong N, Frinking P, ten Cate F, van der Wouw P. Characteristics of contrast agents and 2D imaging. *Proc IEEE Ultrason Symp* **1996** 2:1449-1458.
- [79] de Jong N, Frinking PJA, Bouakaz A, Goorden M, Schuurmans T, Jingping X, Mastik F. Optical imaging of contrast agent microbubbles in an ultrasound field with a 100-MHz camera. *Ultrasound Med Biol* **2000** 26(3):487-492.
- [80] de Jong N, Frinking PJA, Bouakaz A, Ten Cate FJ. Detection procedures of ultrasound contrast agents. *Ultrasonics* **2000** 38:87-92.

BIBLIOGRAPHY

- [81] de Jong N, Hoff L. Ultrasound scattering properties of Albunex microspheres. *Ultrasonics* **1993** 31(3):175-181.
- [82] de Jong N, Hoff L, Skotland T, Bom N. Absorption and scatter of encapsulated gas filled microspheres: theoretical considerations and some measurements. *Ultrasonics* **1992** 30(2):95-103.
- [83] de Jong N, Ten Cate FJ. New ultrasound contrast agents and technological innovations. *Ultrasonics* **1996** 34:587-590.
- [84] de Jong N, Ten Cate FJ, Lancée CT, Roelandt JRTC, Bom N. Principles and recent developments in ultrasound contrast agents. *Ultrasonics* **1991** 29:324-330.
- [85] Kabalnov A, Bradley J, Flaim S, Klein D, Pelura T, Peters B, Otto S, Reynolds J, Schutt E, Weers J. Dissolution of multicomponent microbubbles in the bloodstream: 2. Experiment. *Ultrasound Med Biol* **1998** 24(5):751-760.
- [86] Kabalnov A, Klein D, Pelura T, Schutt E, Weers J. Dissolution of multicomponent microbubbles in the bloodstream: 1. Theory. *Ultrasound Med Biol* **1998** 24(5):739-749.
- [87] Kam Z, Hanser B, Gustafsson MGL, Agard DA, Sedat JW. Computational adaptive optics for live three-dimensional biological imaging. *Proc Natl Acad Sci USA* **2001** 98:3790-3795.
- [88] Keogh JM. Circular transportation facilitation device: Australian patent number AU 2001100012 A4 **2001**.
- [89] King DB, Saltzman ES. Measurement of the diffusion coefficient of sulfur hexafluoride in water. *J Geophys Res* **1995** 100(C4):7083-7088.
- [90] Klaseboer E, Chevaillier JP, Gourdon C, Masbernat O. Film drainage between colliding drops at constant approach velocity: experiments and modeling. *J Colloid Interf Sci* **2000** 229:274-285.
- [91] Klein E. Some background history of ultrasonics. *J Acoust Soc Am* **1948** 20(5):601-604.
- [92] Klibanov AL. Targeted delivery of gas-filled microspheres, contrast agents for ultrasound imaging. *Adv Drug Delivery Rev* **1999** 37:139-157.

BIBLIOGRAPHY

- [93] Klibanov AL, Ferrara KW, Hughes MS, Wible Jr JH, Wojdyla JK, Dayton PA, Morgan KE, Brandenburger GH. Direct video-microscopic observation of the dynamic effects of medical ultrasound on ultrasound contrast microspheres. *Invest Radiol* **1998** 33(12):863-870.
- [94] Kodama T, Takayama K. Dynamic behavior of bubbles during extracorporeal shock-wave lithotripsy. *Ultrasound Med Biol* **1998** 24(5):723-738.
- [95] Kralchevsky PA, Danov KD, Ivanov IB. Thin liquid film physics. In Prud'homme R, Khan S, eds., *Foams, Theory, Measurements and Applications*. New York: Marcel Dekker **1996** 1-98.
- [96] Kudo N, Miyaoka T, Okada K, Yamamoto K, Niwa K. Study on mechanism of cell damage caused by microbubbles exposed to ultrasound. *Proc IEEE Ultrason Symp* **2002** 1351-1354.
- [97] Kuribayashi K, Kudo N, Natori M, Yamamoto K. A high-magnification and high-speed system for the observation of microbubbles under ultrasound exposure. *Proc IEEE Ultrason Symp* **1999** 1755-1758.
- [98] Landau LD, Lifshitz EM. *Fluid Mechanics*. 2nd edition. Oxford: Pergamon Press **1987**.
- [99] Lauterborn W. Optische Kavitation. *Physikalische Blätter* **1976** 32(12):553-563.
- [100] Lauterborn W, Ohl CD. Cavitation bubble dynamics. *Ultrason Sonochem* **1997** 4:65-75.
- [101] Lee HC. Review of image-blur models in a photographic system using the principles of optics. *Opt Eng* **1990** 29(5):405-421.
- [102] Leighton TG. *The Acoustic Bubble*. London: Academic Press Ltd **1994**.
- [103] Lendon CL, Davies MJ, Born GVR, Richardson PD. Atherosclerotic plaque caps are locally weakened when macrophages density is increased. *Atherosclerosis* **1991** 87:87-90.
- [104] Lide DR. *CRC Handbook of Chemistry and Physics*. 82nd edition. Boca Raton, FL: CRC Press LLC **2001**.

BIBLIOGRAPHY

- [105] Lin CY, Slattery JC. Thinning of a liquid film as a small drop or bubble approaches a fluid-fluid interface. *AIChE J* **1982** 28(5):786-792.
- [106] Lin CY, Slattery JC. Thinning of a liquid film as a small drop or bubble approaches a solid plane. *AIChE J* **1982** 28(1):147-156.
- [107] Lohse D, Prosperetti A. Controlling bubbles. *J Phys: Condens Matter* **2003** 15:S415-S420.
- [108] Lohse D, Schmitz B, Versluis M. Snapping shrimp make flashing bubbles. *Nature* **2001** 413:477-478.
- [109] Longuet-Higgins MS. The crushing of air cavities in a liquid. *Proc Roy Soc London A* **1992** 439:611-626.
- [110] Mach E, Mach L. Weitere ballistisch-photographische Versuche. *Sitzungsberichte d kais Akad d Wiss mathem-naturw Classe* **1889** 98(2a):1310-1326.
- [111] Mach E, Salcher P. Photographische Fixirung der durch Projectile in der Luft eingeleiteten Vorgänge. *Sitzungsberichte d kais Akad d Wiss mathem-naturw Classe* **1887** 95(2):764-780.
- [112] Mach E, Salcher P. Über die in Pola und Meppen angestellten ballistisch-photographischen Versuche. *Sitzungsberichte d kais Akad d Wiss mathem-naturw Classe* **1889** 97(2):41-50.
- [113] Magnaudet J, Eames I. The motion of high-Reynolds-number bubbles in inhomogeneous flows. *Annu Rev Fluid Mech* **2000** 32:659-708.
- [114] Marmottant P, Hilgenfeldt S. Controlled vesicle deformation and lysis by single oscillating bubbles. *Nature* **2003** 423:153-156.
- [115] Marrucci G. A theory of coalescence. *Chem Eng Sci* **1969** 24:975-985.
- [116] Maruvada S, Hynynen K. Optical monitoring of ultrasound interaction with blood vessels in transparent fish after injection with contrast agents. *Proc IEEE Ultrason Symp* **2002** 1936-1939.
- [117] Matérn B. Precision of area estimation: a numerical study. *J Microsc* **1989** 153(3):269-284.

BIBLIOGRAPHY

- [118] Mathur AB, Collinsworth AM, Reichert WM, Kraus WE, Truskey GA. Endothelial, cardiac muscle and skeletal muscle exhibit different viscous and elastic properties as determined by atomic force microscopy. *J Biomech* **2001** 34:1545-1553.
- [119] Mathur AB, Truskey GA, Reichert WM. Atomic force and total internal reflection fluorescence microscopy for the study of force transmission in endothelial cells. *Biophys J* **2000** 78:1725-1735.
- [120] May D, Allen J, Ferrara K. Dynamics and fragmentation of thick-shelled microbubbles. *IEEE Trans Ultrason, Ferroelect, Freq Contr* **2002** 49(10):1400-1410.
- [121] May D, Allen J, Gut J, Ferrara K. Acoustic fragmentation of therapeutic contrast agents designed for localized drug delivery. *Proc IEEE Ultrason Symp* **2001** 1385-1388.
- [122] Mayer S, Grayburn PA. Myocardial contrast agents: recent advances and future directions. *Prog Cardiovasc Dis* **2001** 44(1):33-44.
- [123] McManus IC. Scrotal asymmetry in man and in ancient sculpture. *Nature* **1976** 259:426.
- [124] Medwin H. Counting bubbles acoustically: a review. *Ultrasonics* **1977** 15:7-13.
- [125] Miller DL, Nyborg WL. Theoretical investigation of the response of gas-filled micropores and cavitation nuclei to ultrasound. *J Acoust Soc Am* **1983** 73(5):1537-1544.
- [126] Miller MW. Gene transfection and drug delivery. *Ultrasound Med Biol* **2000** 26(S1):S59-S62.
- [127] Minnaert M. On musical air bubbles and the sound of running water. *Philos Mag* **1933** (S. 16):235-248.
- [128] Morgan KE, Allen JS, Chomas JE, Dayton PA, Ferrara KW. Experimental and theoretical analysis of individual contrast agent behavior. *Proc IEEE Ultrason Symp* **1999** 1685-1688.
- [129] Morgan KE, Allen JS, Dayton PA, Chomas JE, Klibanov AL, Ferrara KW. Experimental and theoretical evaluation of microbubble behavior: Effect of transmitted phase and bubble size. *IEEE Trans Ultrason, Ferroelect, Freq Contr* **2000** 47(6):1494-1509.

BIBLIOGRAPHY

- [130] Narsimhan G, Ruckenstein E. Structure, drainage, and coalescence of foams and concentrated emulsions. In Prud’homme R, Khan S, eds., *Foams, Theory, Measurements and Applications*. New York: Marcel Dekker **1996** 99–187.
- [131] Newton I. *Philosophiae Naturalis Principia Mathematica*. 3rd, enlarged & revised edition. London: Guil & Joh Innys **1726**.
- [132] Newton I. *The Principia: mathematical principles of natural philosophy*. Berkeley: University of California Press **1999**.
- [133] Noltingk BE, Neppiras EA. Cavitation produced by ultrasonics. *Proc Phys Soc London B* **1950** 63:674–685.
- [134] Ohl CD, Ikink R. Shock-wave-induced jetting of micron-size bubbles. *Phys Rev Lett* **2003** 90:214 502.
- [135] Ohl CD, Ory E. Aspherical bubble collapse — comparison with simulations. In Lauterborn W, Kurz T, eds., *Nonlinear Acoustics at the Turn of the Millennium: ISNA 15*. New York: American Institute of Physics **2000** 393–396.
- [136] Pain HJ. *The physics of vibrations and waves*. 3rd edition. Chichester: John Wiley & Sons Ltd **1992**.
- [137] Palanchon P, Bouakaz A, Klein J, de Jong N. Subharmonic and ultraharmonic emissions for emboli detection and characterization. *Ultrasound Med Biol* **2003** 29(3):417–425.
- [138] Philipp A, Lauterborn W. Cavitation erosion by single laser-produced bubbles. *J Fluid Mech* **1998** 361:75–116.
- [139] Plesset MS, Mitchell TP. On the stability of the spherical shape of a vapor cavity in a liquid. *Quart Appl Math* **1956** 13(4):419–430.
- [140] Postema M, Bouakaz A, Chin CT, de Jong N. Real-time optical imaging of individual microbubbles in an ultrasonic field. *Proc IEEE Ultrason Symp* **2001** 1679–1682.
- [141] Postema M, Bouakaz A, Chin CT, de Jong N. Optically observed microbubble coalescence and collapse. *Proc IEEE Ultrason Symp* **2002** 1900–1903.

BIBLIOGRAPHY

- [142] Postema M, Bouakaz A, Chin CT, de Jong N. Simulations and measurements of optical images of insonified ultrasound contrast microbubbles. *IEEE Trans Ultrason, Ferroelect, Freq Contr* **2003** 50(5):523-536.
- [143] Postema M, Bouakaz A, de Jong N. *IEEE Trans Ultrason, Ferroelect, Freq Contr* **2002** 49(3):cover.
- [144] Postema M, Bouakaz A, de Jong N. Noninvasive microbubble-based pressure measurements: a simulation study. *Ultrasonics* **2004** 42(1-9):759-762.
- [145] Postema M, Marmottant P, Lancée C, Hilgenfeldt S, de Jong N. Ultrasound-induced microbubble coalescence by parametric instability. *Proc 10th Dutch Annu Conf BioMed Eng* **2003** 177.
- [146] Postema M, Marmottant P, Lancée CT, Hilgenfeldt S, de Jong N. Ultrasound-induced microbubble coalescence. *Ultrasound Med Biol* **2004** submitted.
- [147] Preza C, Miller MI, Thomas Jr LW, McNally JG. Regularized linear method for reconstruction of three-dimensional microscopic objects from optical sections. *J Opt Soc Am A* **1992** 9(2):219-228.
- [148] Prosperetti A. Application of the subharmonic threshold to the measurement of the damping of oscillating gas bubbles. *J Acoust Soc Am* **1977** 61(1):11-16.
- [149] Lord Rayleigh. Investigations in optics, with special reference to the spectroscope. *Philos Mag* **1879** 8(49):261-274.
- [150] Lord Rayleigh. On the pressure development in a liquid during the collapse of a spherical cavity. *Philos Mag* **1917** 32(S8):94-98.
- [151] Reddy AJ, Szeri AJ. Coupled dynamics of translation and collapse of acoustically driven microbubbles. *J Acoust Soc Am* **2002** 112(4):1346-1352.
- [152] Rensen J, Bosman D, Magnaudet J, Ohl CD, Prosperetti A, Tögel R, Versluis M, Lohse D. Spiraling bubbles: how acoustic and hydrodynamic forces compete. *Phys Rev Lett* **2001** 86(21):4819-4822.

BIBLIOGRAPHY

- [153] Reynolds O. On the theory of lubrication and its application to Mr. Beauchamp Tower's experiments, including an experimental determination of the viscosity of olive oil. *Philos Trans Roy Soc A* **1886** 177:157-234.
- [154] Richter IA, ed. *The Notebooks of Leonardo da Vinci*. Oxford World's Classics paperback edition. New York: Oxford University Press Inc **1998**.
- [155] Rönneberg G. Eignung von Fokusverfahren für Beobachtung und Vermessung von Mikrostrukturen. Technical report, Darmstadt: Institut für EMK **1996**.
- [156] Rotsch C, Jacobson K, Radmacher M. Dimensional and mechanical dynamics of active and stable edges in motile fibroblasts investigated by using atomic force microscopy. *Proc Natl Acad Sci USA* **1999** 96:921-926.
- [157] Schlieff R, Poland H. Ultrasonic manometry process in a fluid by means of microbubbles: US patent number 5,195,520 **1993**.
- [158] Schneider M, Arditi M, Barrau MB, Brochot J, Broillet A, Ventrone R, Yan F. BR1: A new ultrasonographic contrast agent based on sulfur hexafluoride-filled microbubbles. *Invest Radiol* **1995** 30(8):451-457.
- [159] Schrope BA, Newhouse VL. Second harmonic ultrasonic blood perfusion measurement. *Ultrasound Med Biol* **1993** 19(7):567-579.
- [160] Shankar PM, Krishna PD, Newhouse VL. Subharmonic backscattering from ultrasound contrast agents. *J Acoust Soc Am* **1999** 106(4):2104-2110.
- [161] Sharma A, Ruckenstein E. Critical thickness and lifetimes of foams and emulsions: role of surface wave-induced thinning. *J Colloid Interf Sci* **1987** 119(1):14-29.
- [162] Sheludko A. Thin liquid films. *Advan Colloid Interf Sci* **1967** 1:391-464.
- [163] Shi WT, Forsberg F, Raichlen JS. Pressure measurements using contrast microbubbles. In Goldberg B, Raichlen J, Forsberg F, eds., *Ultrasound Contrast Agents. Basic principles and clinical applications*, 2nd edition. London: Martin Dunitz Ltd **2001** 105-111.

BIBLIOGRAPHY

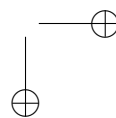
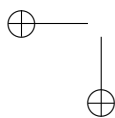
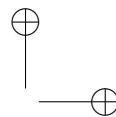
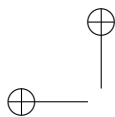
- [164] Shi WT, Forsberg F, Raichlen JS, Needleman L, Goldberg BB. Pressure dependence of subharmonic signals from contrast microbubbles. *Ultrasound Med Biol* **1999** 25(2):275-283.
- [165] Shi WT, Forsberg F, Tornes A, Østensen J, Goldberg BB. Destruction of contrast microbubbles and the association with inertial cavitation. *Ultrasound Med Biol* **2000** 26(6):1009-1019.
- [166] Shohet RV, Chen S, Zhou YT, Wang Z, Meidell RS, Unger RH, Grayburn PA. Echocardiographic destruction of albumin microbubbles directs gene delivery to the myocardium. *Circulation* **2000** 101:2554-2556.
- [167] Silberrad O. Propeller erosion. *Engineering* **1912** 33-35.
- [168] Skaife T. A feat in photography. *Times* **1858** (29 May):12.
- [169] Skyba DM, Price RJ, Linka AZ, Skalak TC, Kaul S. Direct in vivo visualization of intravascular destruction of microbubbles by ultrasound and its local effects on tissue. *Circulation* **1998** 98:290-293.
- [170] Sprung CL, ed. *Pulmonalarterienkatheter: Methodik und klinische Anwendung*. 2nd edition. Berlin: Springer-Verlag **1999**.
- [171] Squires GL. *Practical physics*. 3rd edition. Cambridge: Cambridge University Press **1989**.
- [172] Stokseth PA. Properties of a defocused optical system. *J Opt Soc Am* **1969** 59(10):1314-1321.
- [173] Strasberg M. Gas bubbles as sources of sound in liquids. *J Acoust Soc Am* **1956** 28(1):20-26.
- [174] Stride E, Saffari N. On the destruction of microbubble ultrasound contrast agents. *Ultrasound Med Biol* **2003** 29(4):563-573.
- [175] Tachibana K, Uchida T, Ogawa K, Yamashita N, Tamura K. Induction of cell-membrane porosity by ultrasound. *Lancet* **1999** 353:1409.
- [176] Takeuchi Y. Industrial use thermoplastic microballoon to mimic the contrast agents and its in-vitro behavior including released gas dynamics. *Proc IEEE Ultrason Symp* **1997** 2:1579-1582.

BIBLIOGRAPHY

- [177] Takeuchi Y. Pulsed stroboscopic visualizer to synchronously monitor the microballoon under insonification. *Proc IEEE Ultrason Symp* **1998** 1645-1649.
- [178] Takeuchi Y. *IEEE Trans Ultrason, Ferroelect, Freq Contr* **1999** 46(4):cover.
- [179] Taniyama Y, Tachibana K, Hiraoka K, Namba T, Yamasaki K, Hashiya N, Aoki M, Ogihara T, Yasufumi K, Morishita R. Local delivery of plasmid DNA into rat carotid artery using ultrasound. *Circulation* **2002** 105:1233-1239.
- [180] Thornycroft JI, Barnaby SW. Torpedo-boat destroyers. *Min Proc Inst Civ Eng* **1895** 122:51-69.
- [181] Tickner EG. Precision microbubbles for right side intracardiac pressure and flow measurements. In Meltzer R, Roelandt J, eds., *Contrast echocardiography*. Den Haag: Martinus Nijhoff Publishers **1982** 313-324.
- [182] Tortoli P, Michelassi V, Corsi M, Righi D, Takeuchi Y. On the interaction between ultrasound and contrast agents during Doppler investigations. *Ultrasound Med Biol* **2001** 27(9):1265-1273.
- [183] Uhlendorf V, Hoffmann C. Nonlinear acoustical response of coated microbubbles in diagnostic ultrasound. *Proc IEEE Ultrason Symp* **1994** 1559-1562.
- [184] Unger EC, Matsunaga TO, McCreery T, Schumann P, Sweitzer R, Quigley R. Therapeutic applications of microbubbles. *Eur J Radiol* **2002** 42:160-168.
- [185] Unger EC, Wu Q, McCreery TP, Matsunaga TO. Thrombus-specific contrast agents for imaging and thrombolysis. In Goldberg B, Raichlen J, Forsberg F, eds., *Ultrasound Contrast Agents. Basic principles and clinical applications*, 2nd edition. London: Martin Dunitz Ltd **2001** 337-345.
- [186] Versluis M, Schmitz B, von der Heydt A, Lohse D. How snapping shrimp snap: through cavitating bubbles. *Science* **2000** 289:2114-2117.

BIBLIOGRAPHY

- [187] Vokurka K. Comparison of Rayleigh's, Herring's, and Gilmore's models of gas bubbles. *Acustica* **1986** 59:214-219.
- [188] de Vries J, Luther S, Lohse D. Induced bubble shape oscillations and their impact on the rise velocity. *Eur Phys J B* **2002** 29:503-509.
- [189] van Wamel A, Bouakaz A, ten Cate F, de Jong N. Effects of diagnostic ultrasound parameters on molecular uptake and cell viability. *Proc IEEE Ultrason Symp* **2002** 1387-1390.
- [190] Wei K. Blood flow and perfusion measurements: background and clinical utility. In Goldberg B, Raichlen J, Forsberg F, eds., *Ultrasound Contrast Agents. Basic principles and clinical applications*, 2nd edition. London: Martin Dunitz Ltd **2001** 89-104.
- [191] Wei K, Jayaweera AR, Firoozan S, Linka A, Skyba DM, Kaul S. Quantification of myocardial blood flow with ultrasound-induced destruction of microbubbles administered as a constant venous infusion. *Circulation* **1998** 97:473-483.
- [192] Wild JJ. The use of ultrasonic pulses for the measurement of biologic tissues and the detection of tissue density changes. *Surgery* **1950** 27(2):183-188.
- [193] Wild JJ, Neal D. Use of high-frequency ultrasonic waves for detecting changes of texture in living tissues. *Lancet* **1951** 655-657.
- [194] Wilhelm E, Battino R, Wilcock RJ. Low-pressure solubility of gases in liquid water. *Chem Rev* **1977** 77(2):219-262.
- [195] Worthington AM, Cole RS. Impact with a liquid surface studied by the aid of instantaneous photography. Paper I. *Philos Trans Roy Soc A* **1897** 189:137-149.
- [196] Worthington AM, Cole RS. Impact with a liquid surface studied by the aid of instantaneous photography. Paper II. *Philos Trans Roy Soc A* **1900** 194:175-200.
- [197] Young DF, Munson BR, Okiishi TH. *A Brief Introduction to Fluid Mechanics*. 2nd edition. New York: John Wiley & Sons **2000**.
- [198] Young IT. Quantitative microscopy. *IEEE Eng Med Biol* **1996** 15(1):59-66.



List of Figures

1.1	Thomas Skaife’s claim in <i>The Times, London</i> , of May 29, 1858. Reprinted with permission.	22
1.2	“ <i>Abe Edgington, owned by Leland Stanford; driven by C. Marvin, trotting at a 2:24 gait over the Palo Alto track, 15th June 1878.</i> ” Reprinted with permission from Muybridge HE. <i>The Horse in Motion 1878</i> . In: <i>Adolf Nichtenhauser history of motion picture collection ca. 1950</i> . Collection number MS C 380 located in: Modern Manuscripts Collection, History of Medicine Division, National Library of Medicine, National Institutes of Health, Department of Health and Human Services, Bethesda, MD.	23
1.3	Medical bubble acting as a microsyringe. © 2002 IEEE. Reprinted with permission from Postema M, Bouakaz A, de Jong N. <i>IEEE Trans Ultrason, Ferroelect, Freq Contr</i> 2002 49(3):cover.	25
2.1	One-dimensional, differently sized objects \mathcal{F} , convolved with the PSF, resulting in optical images G . Segmented objects ξ were obtained after applying the threshold $\theta = 0.5$	32
2.2	Measured object diameter (ζ) versus true object diameter (τ) after segmentation using the threshold $\theta = 0.5$	34
2.3	Measured object diameter (ζ) as a function of applied threshold (θ) for three different object diameters.	35
2.4	Basic setup for taking UCA microbubble pictures.	36
2.5	Front-side view of container.	37
2.6	Optical observation part of the experimental setup.	38
2.7	Acoustic signal measured at the transducer focus.	39
2.8	Semi-automated segmentation. Selection of region of interest (a) and (b), binary segmented image (c), segmented object (d).	40
2.9	CCD images of 11 triacontakaidigons (i) on a calibration grid, (ii) segmented with a $\theta = 1/2(\phi + \psi)$ threshold.	41
2.10	Intensity cross-sections of a $5\ \mu\text{m}$ glass calibration particle, $4\ \mu\text{m}$ proximal to focus (a), $2\ \mu\text{m}$ proximal to focus (b), in focus (c), and $2\ \mu\text{m}$ distal to focus (d).	43
2.11	Quantison TM contrast microbubbles above the focal plane of the optical system (a)–(d), shifted through visual focus (e), below the focal plane (f)–(i). Each frame corresponds to a $43 \times 32\ \mu\text{m}^2$ area.	44
2.12	Randomly taken pictures of freely flowing, ultrasound insonified, experimental UCA. Bubbles with a bright center are considered to be out of focus (a), (f). Sharp and unsharp, fuzzy bubbles are comparable in size (b)–(e)	45

LIST OF FIGURES

2.13 Maximal deviation in bubble measurement due to random error caused by the optical system and the segmentation process, as a function of mean bubble diameter measurement. 46

2.14 Bubble expansion at four different acoustic pressures. $MI = 0.089$ (a), $MI = 0.15$ (b), $MI = 0.25$ (c), $MI = 0.39$ (d). 47

2.15 Optical image sequence of three microbubbles with apparently the same initial diameters, insonified at $MI = 0.93$. Each frame corresponds to a $55 \times 45 \mu\text{m}^2$ area. Frame (a) was taken before ultrasound arrival. The microbubbles expanded to different maximal diameters (b)-(d). 47

2.16 Relative excursion at $MI = 0.93$. 39 bubbles were selected from 10 image sequences. Identical markers indicate bubbles from the same image sequence. 48

2.17 Bubble expansion (b)-(e) and collapse (f) within one acoustic cycle at $MI = 1.2$ 48

2.18 Bubbles coalescing during insonification at $MI = 0.93$ 49

2.19 Mean relative excursion as a function of acoustic pressure applied, for bubble diameters ranging from $1.8 \mu\text{m}$ to $2.2 \mu\text{m}$, compared to model A and model B. 50

3.1 Optical images of stages of ultrasound-induced microbubble coalescence: flattening of contact surfaces (a), liquid film drainage (b), forming of a merged bubble (c), turning into an ellipsoidal bubble (d). Each frame in event (i) corresponds to a $21 \times 21 \mu\text{m}^2$ area. Each frame in events (ii)-(iv) corresponds to a $30 \times 30 \mu\text{m}^2$ area. Interframe times are $0.33 \mu\text{s}$ 56

3.2 Schematic representation of stages of expanding bubble coalescence: bubble collision (a), flattening of contact surfaces (b), liquid film drainage (c) until a critical thickness (d), film rupture (e), and formation of an ellipsoidal bubble (f). 57

3.3 Schematic overview of variables used. 58

3.4 Optical images of microbubble coalescence and spherical rebound (i), bounce (ii), multiple coalescence (iii), and repeated coalescence (iv). Each frame corresponds to a $30 \times 30 \mu\text{m}^2$ area. The frames in column a have been captured prior to ultrasound arrival. Interframe times are $0.33 \mu\text{s}$ 62

4.1 Schematic representation of colliding bubbles or droplets: approach (a-b), flattening of the interposed film (c), drainage to a critical thickness (d), film rupture (e), and formation of a single bubble (f). 68

4.2 Gas release from PB127 microbubbles, captured at 10 MHz. Each frame corresponds to a $23 \times 23 \mu\text{m}^2$ area. Spontaneous coalescence of free gas microbubbles takes place in frames 81-83. 71

5.1 Fundamental and subharmonic scattering cross-sections of a diffusing $\varnothing 14 \mu\text{m}$ Ar bubble, insonified at 1 and 2 MHz, respectively, as a function of time, when applying hydrostatic overpressures of 0 and 50 mmHg. 81

6.1 Line drawings of the housing of the Brandaris-128 (left) and the CR 2000 camera (right). 85

6.2 Gas release from a Quantison™ contrast microbubble at 0.5 MHz and $MI = 1.1$. Each frame corresponds to a $19 \times 19 \mu\text{m}^2$ area. Interframe times are $0.1 \mu\text{s}$ 88

6.3 Gas release from a Quantison™ contrast microbubble at 0.5 MHz and $MI = 0.9$. Each frame corresponds to a $13 \times 13 \mu\text{m}^2$ area. Interframe times are $0.33 \mu\text{s}$ 89

LIST OF FIGURES

6.4 Dissolution of released gas. Each frame corresponds to a $13 \times 13 \mu\text{m}^2$ area. Time between recordings is 100 ms. The free gas bubble is visible to the upper left of the PB127 bubble in the left frame. 89

6.5 Dissolution of released gas, captured at 2 kHz. Upper frames show raw CCD images, lower frames show segmented images. Each frame corresponds to a $10 \times 10 \mu\text{m}^2$ area. The released gas fragments (arrow) are less than $1 \mu\text{m}$ 90

6.6 Gas release from a PB127 contrast microbubble at 1.7 MHz and $M_I = 0.9$. Each frame corresponds to a $46 \times 30 \mu\text{m}^2$ area. Interframe times are $0.1 \mu\text{s}$. After release (first three rows), the free gas bubbles interact, until one free gas bubble remains (last row). 91

6.7 Three PB127 bubbles and one released gas bubble (left). After 100 ms the released gas bubble has disappeared (right). Each frame corresponds to a $23 \times 23 \mu\text{m}^2$ area. Time between recordings is 100 ms. 92

6.8 Size distribution of released gas from PB127. 93

6.9 Average number of cracked contrast agent bubbles for $M_I > 0.8$ 94

6.10 Dissolution of nitrogen microbubbles with diameters between 0.5 and $4.5 \mu\text{m}$ into saturated water at ambient pressure. 95

7.1 Schematic evolution of jet development in a collapsing bubble near a boundary (below): bubble on the verge of collapse (a), asymmetric collapse (b), jet development (c), funnel-shaped protrusion (d). 106

7.2 Basic setup of the high-speed photography system. 109

7.3 Line drawing of the Brandaris-128 system. 110

7.4 Line drawing of the optical observation part of the Brandaris-128 system. 111

7.5 Line drawing of the optical observation of the Imacon 468 system. 112

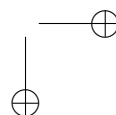
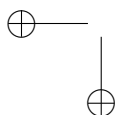
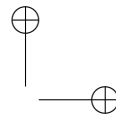
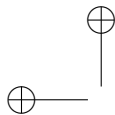
7.6 Oscillating experimental UCA microbubbles. Both respective image sequences span one ultrasonic cycle. Frames a have been captured prior to ultrasound arrival. Inter-frame times for frames b to h are $0.33 \mu\text{s}$. Each frame corresponds to a $88 \times 58 \mu\text{m}^2$ area. (i) Two $\phi 6 \mu\text{m}$ bubbles moderately oscillating ($M_I = 0.09$). (ii) A $\phi 1.5 \mu\text{m}$ bubble strongly oscillating ($M_I = 0.67$). (iii) Radius-period plots of both events. The solid line represents an oscillating free gas bubble. 115

7.7 (a-d) Sonic cracking of a $\phi 4 \mu\text{m}$ QuantisonTM bubble ($M_I = 1.5$). (e-i) The released gas is subjected to a primary radiation force. Each image frame corresponds to a $30 \times 16 \mu\text{m}^2$ area. Frames shown were selected from a sequence of 128 frames. The travel distance of the bubble center between (e) and (h) is $14 \mu\text{m}$ over 4 ultrasonic cycles. 116

7.8 The approach of two $\phi 4 \mu\text{m}$ experimental UCA bubbles induced by a secondary radiation force. Each image frame corresponds to a $30 \times 20 \mu\text{m}^2$ area. Frames are each captured after insonification by 10 cycles of 0.5 MHz ultrasound ($M_I = 0.67$). 117

7.9 Experimental UCA microbubbles showing (i) coalescence, (ii) second mode spherical harmonic fragmentation, (iii) sonic cracking. Frames a have been captured prior to ultrasound arrival. Inter-frame times for frames b to h are $0.33 \mu\text{s}$. Each image frame corresponds to a $23 \times 23 \mu\text{m}^2$ area. 118

7.10 Ultrasound-induced jet development in an experimental UCA microbubble ($M_I = 1.2$). Each image frame corresponds to a $38 \times 30 \mu\text{m}^2$ area. Inter-frame time is $0.33 \mu\text{s}$ and exposure time is 10 ns 120



List of Publications

Peer-reviewed articles

- Postema M, Bouakaz A, Versluis M, de Jong N. Ultrasound-induced gas release from contrast agent microbubbles. **2004** submitted.
- Postema M, Marmottant P, Lancée CT, Hilgenfeldt S, de Jong N. Ultrasound-induced microbubble coalescence. *Ultrasound Med Biol* **2004** submitted.
- Postema M, van Wamel A, Lancée CT, de Jong N. Ultrasound-induced encapsulated microbubble phenomena. *Ultrasound Med Biol* **2004** 30(6):827–840.
- Postema M, Bouakaz A, de Jong N. Noninvasive microbubble-based pressure measurements: a simulation study. *Ultrasonics* **2004** 42(1-9): 759–762.
- Postema M, Bouakaz A, Chin CT, de Jong N. Simulations and measurements of optical images of insonified ultrasound contrast microbubbles. *IEEE Trans Ultrason, Ferroelect, Freq Contr* **2003** 50(5):523–536.

Conference proceedings

- Postema M, Bouakaz A, Versluis M, de Jong N. Towards controlled gas release from hard-shelled microbubbles. *Proc IEEE Ultrasonics Symp* **2004** to be submitted.
- Postema M, Marmottant P, Lancée CT, Versluis M, Hilgenfeldt S, de Jong N. Ultrasound-induced coalescence of free gas microbubbles. *Proc IEEE Ultrason Symp* **2004** to be submitted.

LIST OF PUBLICATIONS

- Postema M, Marmottant P, Lancée C, Hilgenfeldt S, de Jong N. Ultrasound-induced microbubble coalescence by parametric instability. *Proc 10th Dutch Annu Conf BioMed Eng* **2003** 177.
- Postema M, Bouakaz A, Chin CT, de Jong N. Optically observed microbubble coalescence and collapse. *Proc IEEE Ultrason Symp* **2002** 1900-1903.
- Postema M, Bouakaz A, Chin CT, de Jong N. Real-time optical imaging of individual microbubbles in an ultrasonic field. *Proc IEEE Ultrason Symp* **2001** 1679-1682.

Conference abstracts

- Postema M, Bouakaz A, de Jong N. Controlled gas release from rigid-shelled microbubbles. *Abstr IEEE Ultrasonics Symp* **2004** accepted.
- Postema M, Lancée CT, de Jong N, Marmottant P, Hilgenfeldt S. Ultrasound-induced coalescence of contrast agent microbubbles. *Abstr IEEE Ultrasonics Symp* **2004** accepted.
- Postema M. Beter met bier. *Abstr NWO Bessensap* **2004** 10.
- Postema M, Bouakaz A, Chin CT, de Jong N. Optical observations of ultrasound contrast agent destruction. *Acta Acust united Acust* **2003** 89:728.
- Postema M, Bouakaz A, de Jong N. Noninvasive microbubble-based pressure measurements: a simulation study. *Abstr Ultrasonics Int Symp* **2003** 2.44C.
- Postema M, Bouakaz A, de Jong N. Ultrasonic contrast agent destruction mechanisms revealed by optical observations. *Abstr 8th Eur Symp Ultrasound Contrast Imaging*; Ten Cate F, de Jong N, Cosgrove DO, Eds. **2003** 58-60.
- Postema M, Bouakaz A, Chin CT, de Jong N. Optically observed microbubble coalescence and collapse. *Abstr IEEE Ultrason Symp* **2002** 300-301.
- Postema M, Bouakaz A, Chin CT, de Jong N. Real-time optical imaging of individual microbubbles in an ultrasonic field. *Abstr IEEE Ultrason Symp* **2001** 144.

LIST OF PUBLICATIONS

Other

Postema M. Dynamisch microbelgedrag onder invloed van ultrageluid.
MagICINe **2003** (3):9-11.

Postema M, Bouakaz A, de Jong N. *IEEE Trans Ultrason, Ferroelect, Freq
Contr* **2002** 49(3):cover.

OVER DE AUTEUR



Foto: Jeroen Goudswaard

ISBN 90-365-2037-1

© 2004 Michiel Postema, Bergschenhoek.

All rights reserved. No part of this publication may be reproduced, stored in a retrieval system or transmitted in any form or by any means, electronic, mechanical, photocopying, recording or otherwise, without the prior written permission of the author.

Typesetting system: \LaTeX

Printed in The Netherlands by Universal Press, Veenendaal

Cover design: Michiel Postema